INVESTIGATING NUCLEAR STRUCTURE WITH REACCELERATED RARE-ISOTOPE BEAMS USING GAMMA-RAY SPECTROSCOPY

By

John Edward Ash

A DISSERTATION

Submitted to
Michigan State University
in partial fulfillment of the requirements
for the degree of

Physics - Doctor of Philosophy

2021

ABSTRACT

INVESTIGATING NUCLEAR STRUCTURE WITH REACCELERATED RARE-ISOTOPE BEAMS USING GAMMA-RAY SPECTROSCOPY

By

John Edward Ash

Discovering unexplored high-spin states in neutron-rich nuclei can open up a new direction to study band structure and the associated shell structure in isospin-asymmetric many-body systems. However, experimental reach has so far been limited to neutron-deficient or stable nuclei which are preferentially produced in fusion reactions used in such studies. By using neutron-rich rare-isotope beams, this limitation can be effectively removed, exposing previously inaccessible nuclei to this proven approach.

This dissertation reports an experiment designed to kick off a spectroscopy program to study nuclear structure by means of low-energy nuclear reactions with reaccelerated rare-isotope beams available from the ReA3 facility at National Superconducting Cyclotron Laboratory. A ^{40}Ar stable beam and a ^{45}K rare-isotope beam impinged on a self-supporting lithium target to produce products ranging from argon to titanium via both direct and compound nucleus reactions. These mechanisms provide complementary tools to study the single-particle and collective natures of the states being probed. Using particle and gamma-ray coincidence relations between a silicon charged-particle detector and the Segmented Germanium Array, reaction channels were distinguished and new properties were revealed, including for the nuclei ^{46}Ca and ^{47}K.

For ^{46}Ca, three new higher-lying states around 6 MeV and five new gamma-ray transitions were identified, suggesting three independent band structures formed from different particle-hole configurations. The rotational-like band built on the 0_2^+ state is established up to the tentatively assigned 6_2^+ state. New results are compared to large-scale shell model calculations, confirming the validity of the effective interaction describing particle-hole excitations across the Z=20 and N=28 shell gaps in the vicinity of doubly-magic ^{48}Ca. Shape coexistence observed in lighter-mass calcium isotopes is suggested to persist in ^{46}Ca, albeit as part of a transition from neutron to proton cross-shell excitations. For ^{47}K, differential cross sections were extracted for the two-neutron transfer channel related to the present intruder configuration. Comparisons to Coupled Reaction Channels calculations indicate strong single-particle character for the states and a direct one-step process for the reaction itself.

This work successfully developed the experimental techniques to use reaccelerated beams for spectroscopy of hitherto unexplored nuclei and demonstrated the ability of this approach to expand the experimental reach of nuclear structure studies.

ACKNOWLEDGMENTS

This document represents the tireless effort of many people beyond just myself, including my colleagues, mentors, teachers, friends, and family. The number of people who have supported me and made this work possible is far greater than the ones listed here, so please forgive any omissions.

I would not have reached this goal without my research advisor, Dr. Hironori Iwasaki. We worked together at every stage of this journey, from proposing the experiment to writing the paper and this thesis. He trained me well as a scientist and provided valuable insight and support while I was making important choices for my future career. I would also like to thank the members of my guidance committee, Dr. Alexandra Gade, Dr. Pengpeng Zhang, Dr. Sean Liddick, and Dr. Filomena Nunes. In particular, what I learned from Dr. Nunes about nuclear reaction theory proved essential to this work. Dr. Liddick's work with the Nuclear Science and Security Consortium (NSSC) was instrumental both in my funding and in broadening my perspective on the field.

Thank you to all past and present members of the NSCL Lifetime group, as well as Dr. Dirk Weisshaar and the rest of the NSCL Gamma group. Working alongside you all was a great privilege and an invaluable learning experience. For the use of the JANUS experimental setup and GRUTinizer analysis package, a special debt of gratitude is owed to Dr. Eric Lunberberg (and Dr. Peter Bender, Dr. Mark Spieker, et al.). Among our many outside collaborators, Dr. Ching-Yen Wu and Dr. Jack Henderson aided in performing my thesis experiment, and Dr. Nick Scielzo and Dr. Aaron Gallant provided me the rewarding opportunity to work at Lawrence Livermore National Lab on a summer project.

I would also like to thank my undergraduate research advisor Dr. Mustafa Rajabali, who

introduced me to the world of nuclear physics. It was under his tutelage that I participated in my first experiment and went to my first physics conference. I am grateful for his patience while explaining the basic principles of nuclear physics research to me, especially when it required two or three attempts to finally sink in.

Lastly, I would like to express my gratitude and love for my family, especially my parents and my sister, for their unwavering support during all the unexpected challenges that the last five years have brought.

TABLE OF CONTENTS

LIST OF TABLES

LIST OF FIGURES

Chapter 1

Introduction

1.1 Properties of Nuclei

The atomic nucleus is composed of positively-charged protons and electrically-neutral neutrons held together by the strong nuclear force. The atomic number Z of a nucleus is the number of protons it contains, and determines what element the nucleus is. When added to the number of neutrons N, the sum is referred to as the mass number, $A = Z + N$, which is the number of nucleons that make up the nucleus. If X is taken as the elemental symbol corresponding to a given atomic number Z, then nuclei are often denoted by the abbreviation ^{A}X, for instance ^{46}Ca with $Z = 20$ and $N = 26$. Nuclei with the same number of of protons, neutrons, or nucleons are refereed to as isotopes, isotones, and isobars, respectively.

Nuclei pose a complex quantum many-body problem in an extremely dense environment. In an atom, electrons are bound into orbits around the nucleus due solely to the Coulomb interaction, and the system has a typical radius of 10^{-10} m. On the other hand, the nucleus itself experiences Coulomb repulsion between constituent protons, yet is bound into a volume with a radius on the order of 10^{-15} m. This confinement is surprising given that the nucleus contains 99.9% of the mass of the atom. Another force must be binding nucleons together that is much stronger than the force of Coulomb repulsion, roughly 100 times stronger over distances of 1 fm $= 10^{-15}$ m. In fact this inter-nucleon force is an effective interaction from

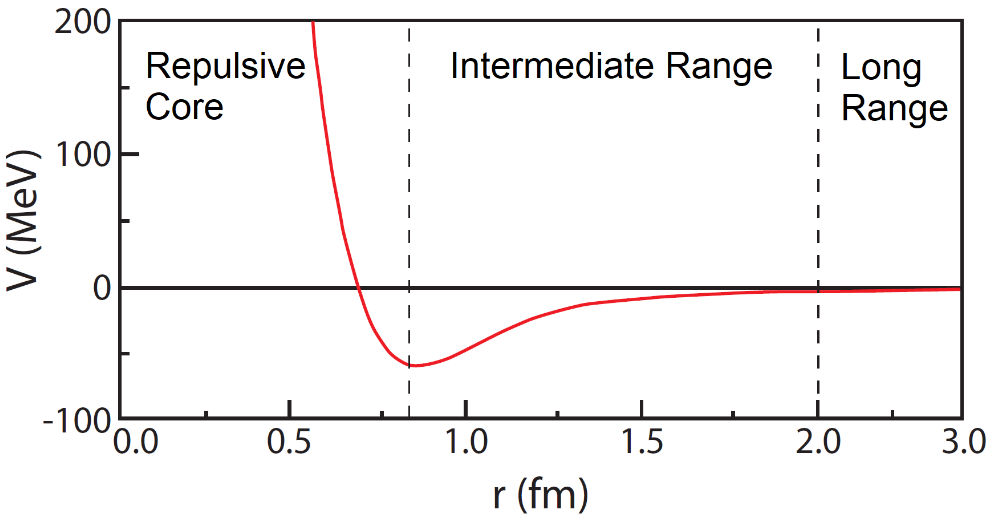

Figure 1.1: The radial component of the nucleon-nucleon interaction. Outside of the repulsive core, the interaction strength quickly goes to zero. Typical distances between bound nucleons are in the long range region. The figure is adapted from Ref. [1].

a force originating within the nucleons themselves, called the strong nuclear force.

Protons and neutrons are composite particles called hadrons made of fundamental particles known as quarks. The strong nuclear force confines quarks into hadrons in sets of three: two up quarks and one down quark for protons, and one up quark and two down quarks for neutrons. For the known net charges of e and 0 for protons and neutrons to occur, up and down quarks must have individual charges of $+2/3e$ and $-1/3e$, respectively. The strong nuclear force described by quantum chromodynamics binds quarks together into protons and neutrons and creates a residual interaction, akin to intermolecular forces in chemistry. The residual nuclear force beteen nucleons combine to form the effective interaction that binds nucleons into the nucleus.

There is no simple analytical form for the nuclear force, but general properties can be deduced. One representation is to only consider two-body nucleon-nucleon (NN) interactions. These interactions have been shown to be mostly charge independent. The shape of the central part of the NN potential, not including the spin-dependent tensor force, is shown in

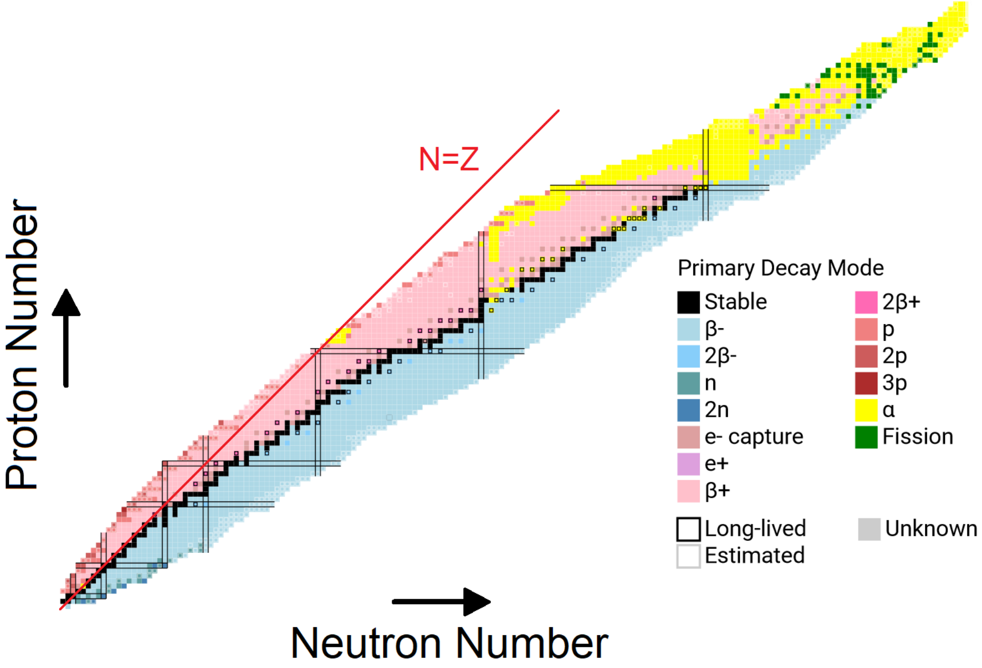

Figure 1.2: The Nuclear Chart. The colors correspond to the decay mode of each nucleus, plotted according to Z and N. The horizontal and vertical bars show the proton and neutron magic numbers 2, 8, 20, 28, 82, and 126. The figure is adapted from Ref. [2].

Figure 1.1. At ranges below 1 fm, the force is strongly repulsive. This repulsion arises from the Pauli exclusion force between alike nucleons, or between alike quarks in the case of the proton-neutron interaction. Beyond 1 fm the force is attractive, but rapidly diminishes in strength. The Coulomb force is roughly equal in strength at 2.5 fm.

A trend emerges from the competition between Coulomb and nuclear forces, as seen in Figure 1.2. The nuclear chart spans the roughly 3,000 nuclei known to exist by plotting their atomic number Z and neutron number N. A total of 252 nuclei have never been observed to decay and are referred to as stable. Through the center of the range of nuclei lies the so-called valley of stability, which follows an observable trend that begins with ^{1}H following $N = Z$ until bending away significantly for heavier nuclei toward greater numbers of neutrons ($N > Z$), finally ending at ^{208}Pb. This is due to the total strength of the Coulomb force that repels the constituent protons in the nuclei increasing compared to the strength of binding

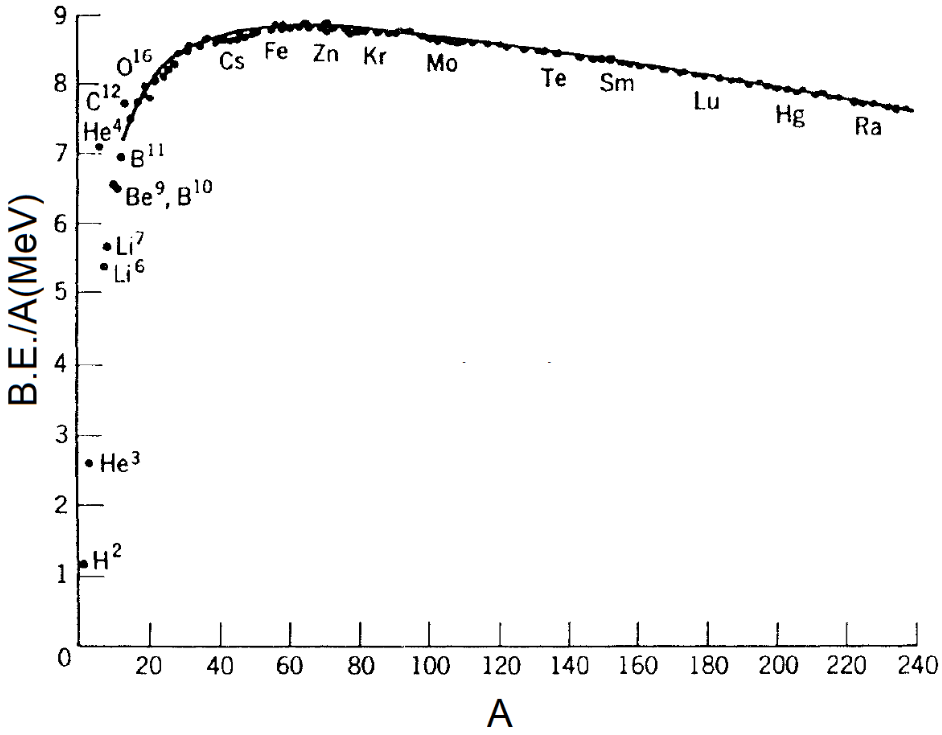

Figure 1.3: A plot of the total binding energy per nucleon against mass number A. The turning point due to saturation is clearly visible around $A = 60$. The solid curve is the result of a semi-empirical mass formula that includes corrections for surface effects, Coulomb repulsion, the Pauli principle, and pairing effects. The figure is adapted from Ref. [3].

nuclear force as mass increases. Protons become relatively less bound compared to neutrons, producing the observed trend.

The outpacing of nuclear forces by Coulomb repulsion can only happen if nuclei reach a point of saturation, where the nucleus has a roughly constant density of nucleons over its volume. This implies that the volume of the nucleus increases proportionally to the mass number A, meaning that distant nucleons no longer interact due to the short range of nuclear interactions (Figure 1.1). On the other hand, the Coulomb force is long range, so all protons in the nucleus experience roughly the same force. This saturation is seen in Figure 1.3 around A=60, where the binding energy per nucleon reaches a maximum. Binding energy is defined as the amount of energy necessary to separate all of the constituent nucleons and is a measure of the total energy of interactions between nucleons. For nuclei lighter than the turning point, binding energy increases roughly quadratically with A, because each nucleon interacts with every other nucleon, yielding a total of $A(A-1)$ interactions. However, once the nucleus reaches a certain size, only the nearest neighbors experience a strong interaction.

Nucleons are spin-1/2 fermions, each of which have intrinsic spin s and orbital angular momentum l. These two momenta couple to form the total angular momentum j, which then is added vectorily to produce the total spin of the nucleus J. Each nucleon has an individual energy, the sum of which is a nuclear energy state. The lowest energy state for a nucleus is referred to as its ground state. A state's excitation energy E_x is defined as its energy relative to the ground state of the nucleus. Discovering the energy and spins of nuclear excited states is key in experimental investigation into nuclear structure.

1.1.1 Shell Structure of Atomic Nuclei

Shown in Figure 1.4 is some of the voluminous evidence of the presence of shell structure in atomic nuclei. Nuclei with an even number of protons and neutrons are plotted according to the excitation energy E_x of their first excited state. At specific numbers of protons or neutrons, referred to as magic numbers, the first excited state is seen to be much higher lying than in neighboring nuclei. The observed magic numbers are 2, 8, 20, 28, 50, 82, and 126. Other examples of evidence are the sharp drop-offs in proton and neutron separation energies after their respective magic numbers. This behavior is directly analogous to the sharp changes in electron binding energies that occur after a closed electron shell, and thus could imply the existence of nuclear shells composed of single particle levels.

The nuclear shell model begins with the assumption of independent particle motion under a central potential. This assumption, that nucleons in a densely-packed nucleus do not

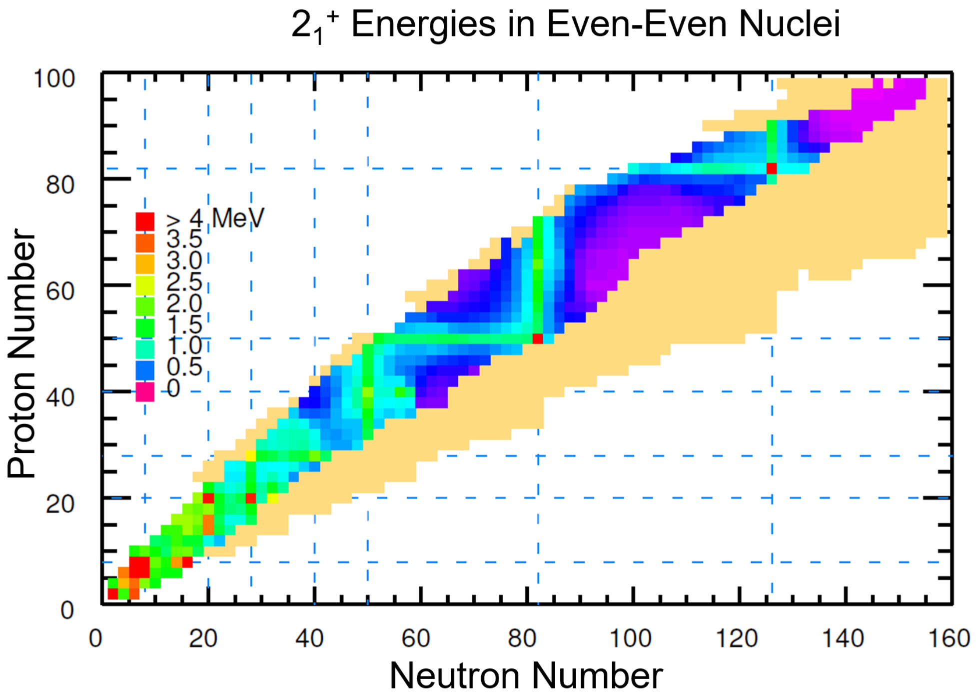

Figure 1.4: A plot of the nuclear chart showing the known 2_1^+ excited state energies of all even-even nuclei. Specific numbers of protons or neutrons are marked with dashed lines, including 8, 20, 28, 40, 50, 82, and 126. These magic numbers coincide with large first excited state energies. The figure is adapted from Ref. [4].

interfere with one another, does not appear valid at first, or at least appears more complicated than the analogous case of electron orbitals in an otherwise empty atom. However, nucleons are subject to the Pauli principle for fermions and thus cannot share the same quantum states. This is what allows the idea of nuclear shells filling sequentially to work in the first place; otherwise, all nucleons could occupy the lowest single-particle level. Nucleons occupying a low single-particle level would then be unable to exchange energy in a collision, because there would be no available energy states within the reach of the relatively weak residual nuclear force. Finally, the Pauli exclusion principle also explains the tendency of stable nuclei to have roughly equal amounts of protons and neutrons. Since the two types of nucleons are distinguishable, they occupy separate sets of single-particle levels, meaning the most energetically favorable configuration for a given number of nucleons is $N = Z$, ignoring Coulomb repulsion.

In order for the nuclear shell model to explain the existing magic numbers, some properties of the central potential must be defined. From quantum mechanics, having a central potential that only depends on the distance from the center (r) allows for the Schrödinger equation to be separated into radial and angular components along with the corresponding wave function solutions $\psi(r, \theta, \phi) = \frac{1}{r}R(r)\psi(\theta, \phi)$. The angular part of the eigenstates are given by the standard spherical harmonics, with quantum numbers $\ell = 0, 1, 2...$ and $m = -\ell, ..., \ell$. This leaves the radial equation:

$$\frac{\hbar^2}{2M}\frac{d^2R_{n\ell}(r)}{dr^2} + \left[E_{n\ell} - V(r) - \frac{\hbar^2}{2M}\frac{\ell(\ell+1)}{r^2}\right]R_{nl\ell}(r) = 0 \tag{1.1}$$

where the $n = 1, 2, ...$ quantum number specifies the number of nodes of the wave function. To start off, the harmonic oscillator potential is a good potential due to the ease of solving for its eigenvalues:

$$V(r) = \frac{1}{2}M\omega^2r^2 \tag{1.2}$$

$$E_{n\ell} = \left(2n + \ell - \frac{1}{2}\right)\hbar\omega. \tag{1.3}$$

These energy levels are plotted in the left column in Figure 1.5. Each level contains degenerate multiplets of $N = 2(n-1) + \ell$ states. For each nl state there are $2(2\ell + 1)$ degenerate m states. By Pauli's exclusion principle, one nucleon can occupy each of these states, and so by counting up these states you arrive at the gaps in energy shown on the left. These shells only partially correspond to the empirical magic numbers, so modifications to

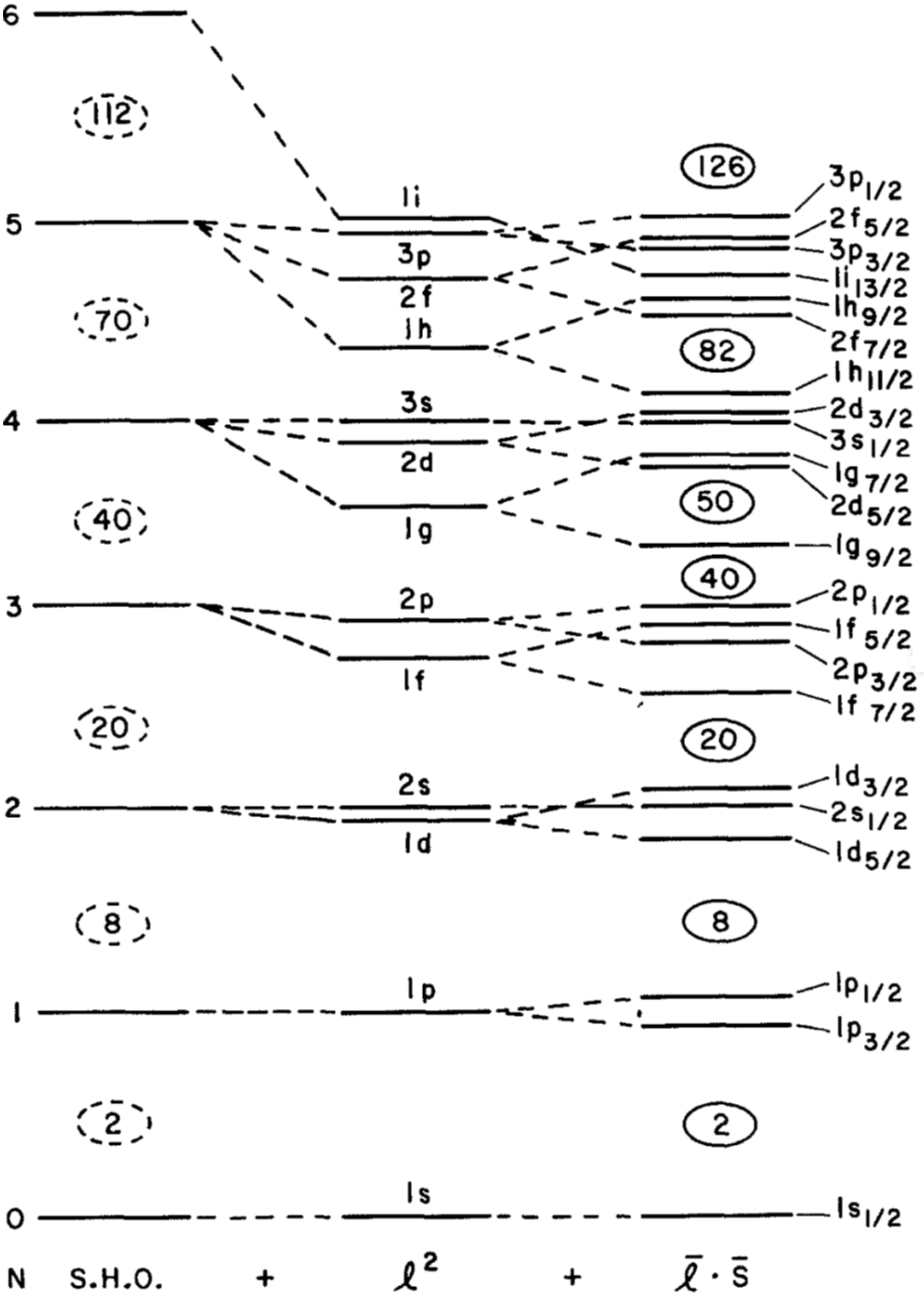

Figure 1.5: A figure showing the development of the magic numbers from single particle energies in a common potential, starting with a simple harmonic oscillator (S.H.O.), adding a term related to orbital angular momentum ℓ^2, and lastly adding a spin-orbit $\vec{\ell} \cdot \vec{s}$ term. The figure is from Ref. [3].

the potential must be made. These modifications that were originally suggested in 1949 [5] were the foundation on which nearly all of nuclear physics has been based since.

The first addition to make the potential more realistic is to add an ℓ^2 term to the potential. Having a potential that is less quadratic and more like a square well is preferable because nucleons in the interior of the nucleus would be screened somewhat by the potential at the boundaries, since they are surrounded by other nucleons more or less symmetrically. Since the orbits with higher angular momentum have larger average radii due to the centrifugal force, the effect of an ℓ^2 term is to flatten the bottom of the harmonic oscillator potential. Introducing this term breaks the $2(n-1)+\ell$ degeneracy as higher ℓ levels are brought down in energy, producing the energy levels shown in the middle of Figure 1.5.

Finally, a spin-orbit term related to $\vec{\ell}\cdot\vec{s}$ is introduced. Each nucleon has an intrinsic spin of 1/2, which can be coupled to its orbital angular momentum in either a parallel or antiparallel direction. This spin-orbit term would be expected to be surface-peaked for similar reasoning to the ℓ^2 term, and if the potential is negative and large enough, then the new $j = \ell \pm 1/2$ states will split in such a way that reproduces the observed magic numbers (see Figure 1.5).

The shell model is a single-particle model, and so its application is potentially restricted to nuclei with very few valence nucleons above an inert doubly-magic core. Closed shells couple to a total $J = 0$, meaning the wavefunction is spherically symmetric. This means their interaction with valence nucleons is limited to influencing their single-particle energies. Expanding the usage of the shell model to more complex cases requires a quickly increasing number of interactions to be accounted for. This model has been developed extensively and has led to a formalism that not only accurately describes many nuclei but also provides the microscopic basis for many macroscopic models of collective properties of nuclei [3].

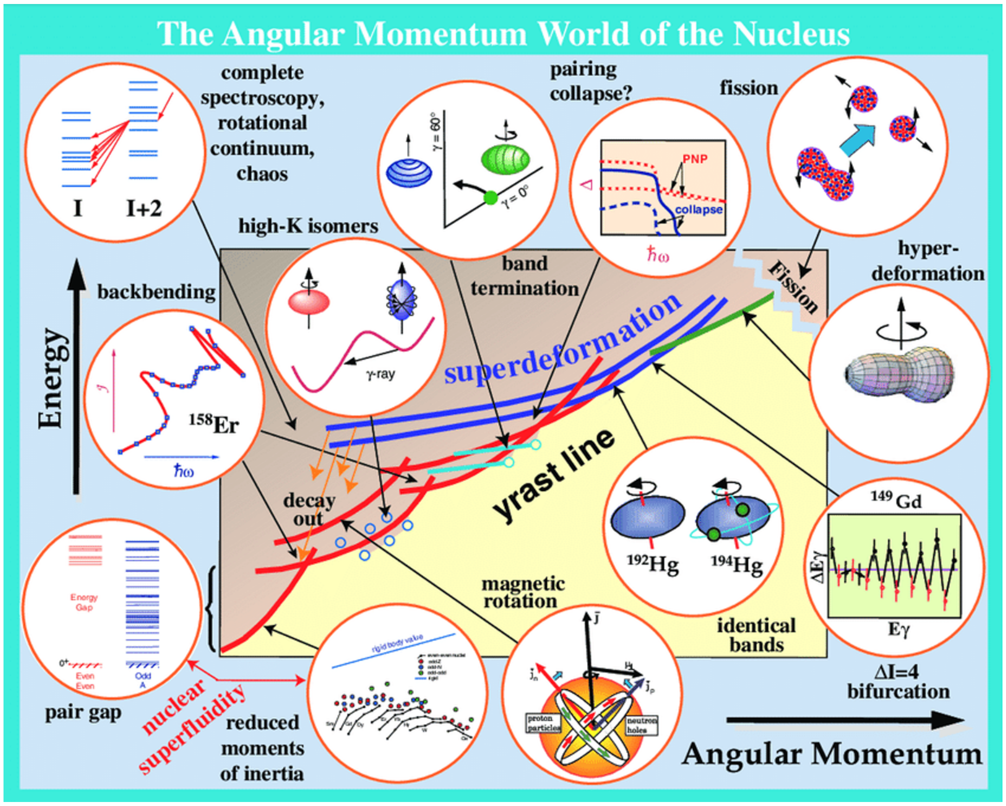

Figure 1.6: A plot showing advances in nuclear structure that were accomplished by exploring the angular momentum frontier. The figure is adapted from Ref. [6].

1.1.2 Collective Phenomena in Nuclei

As the number of valence nucleons increases when one moves away from the magic, closed shell nuclei, the number of degrees of freedom become impractical for shell model approaches. This coincides with the accumulation of proton-neutron interactions as the increasing number of valence nucleons undergo configuration mixing. From this mixing arises highly coherent motion of the nucleons that are better described with macroscopic collective models.

Figure 1.6 summarizes some of the achievements of the past several decades in using high angular momentum states to study collectivity in nuclei. Exploring the angular momentum frontier was an extremely fruitful approach, so only a few results will be briefly summarized here.

Spherical nuclei like those modelled with a spherically symmetric mean-field do not have an axis of symmetry about which to rotate. Only deformed nuclei away from closed shells can develop rotational modes, which for axially-symmetric nuclei have excited state energies of [3]

$$E_{rot} = \frac{\hbar^2}{2I} J(J+1), \tag{1.4}$$

where I is the moment of inertia and only even J are allowed by selection rule. Excited state bands following this trend have been found in hundreds of deformed nuclei, especially by the characteristic $E_{4_1^+}/E_{2_1^+} = 3.33$ ratio of the lowest lying states. However, the inertial parameter, $\hbar^2/2I$, is generally different for different bands, even for bands within the same nucleus. This underscores the phenomena of shape coexistence, where different band structures are connected to distinct and competing nuclear shapes. To quantify the deformation of a spherical nucleus of radius $R_0 = r_0 A^{1/3}$, a parameterization is introduced

$$R(\theta, \phi) = R_0 \left[1 + \sum_{\lambda=1}^{\infty} \sum_{\mu=-\lambda}^{\lambda} \alpha_{\lambda\mu} Y_{\lambda\mu}(\theta, \phi) \right], \tag{1.5}$$

where $Y_{\lambda\mu}(\theta, \phi)$ are the spherical harmonics and $\alpha_{\lambda\mu}$ are coefficients representing the distortion. For $\lambda = 1$, α can be set to zero since this only represents the motion of the nuclear center of mass. The $\lambda = 2$ terms describe quadrupole deformation, while higher order terms describe octupole ($\lambda = 3$) shapes, hexadecapole ($\lambda = 4$) shapes, etc. For quadrupole deformation, one can align the principal axes of the deformed nucleus with the coordinate system and show that $\alpha_{22} = \alpha_{2-2}$ and $\alpha_{21} = \alpha_{2-1} = 0$, leaving two independent coefficients to describe the system, α_{20} and α_{22}. These can be related to two alternative parameters: β, the axially symmetric quadrupole deformation, and γ, the degree of axial asymmetry, through the relations $\alpha_{20} = \beta \cos\gamma$ and $\alpha_{22} = -1/\sqrt{2}\beta \sin\gamma$. The radii along the principal axes can then be written as

$$\begin{aligned} R_z &= R_0\left(1+\sqrt{\frac{5}{4\pi}}\beta\cos\gamma\right), \\ R_x &= R_0\left[1+\sqrt{\frac{5}{4\pi}}\beta\cos\left(\gamma-\frac{2\pi}{3}\right)\right], \\ R_y &= R_0\left[1+\sqrt{\frac{5}{4\pi}}\beta\cos\left(\gamma-\frac{4\pi}{3}\right)\right]. \end{aligned} \tag{1.6}$$

These expressions show that $\beta = 0$ for a spherical nucleus, $\beta > 0, \gamma = 0°$ for an axially symmetric prolate nucleus, and $\beta > 0, \gamma = 60°$ for an axially symmetric oblate nucleus. In the latter two cases, it can be shown through an integral that the moment of inertia is related to the quadrupole deformation to first order as

$$I = \frac{2}{5}AMR_0^2\left(1+0.31\beta\right). \tag{1.7}$$

Thus the level energies in a rotational band can be related to the quadrupole deformation of the band through the moment of inertia. It should be noted that the intrinsic quadrupole moment can also be related to β and is directly measured through techniques like multi-step Coulomb excitation.

Equation 1.4 implies that the spacing of states in the rotational band, and thus the gamma-energies from in-band transitions, would follow

$$E_\gamma(J \rightarrow J-2) = \frac{\hbar^2}{2I}\left(4J-2\right), \tag{1.8}$$

meaning that they would be linear in J. This can be seen in Figure 1.7, where the marked sequence of gamma rays correspond to a rotational band in ^{152}Dy [8]. Using Equations 1.7

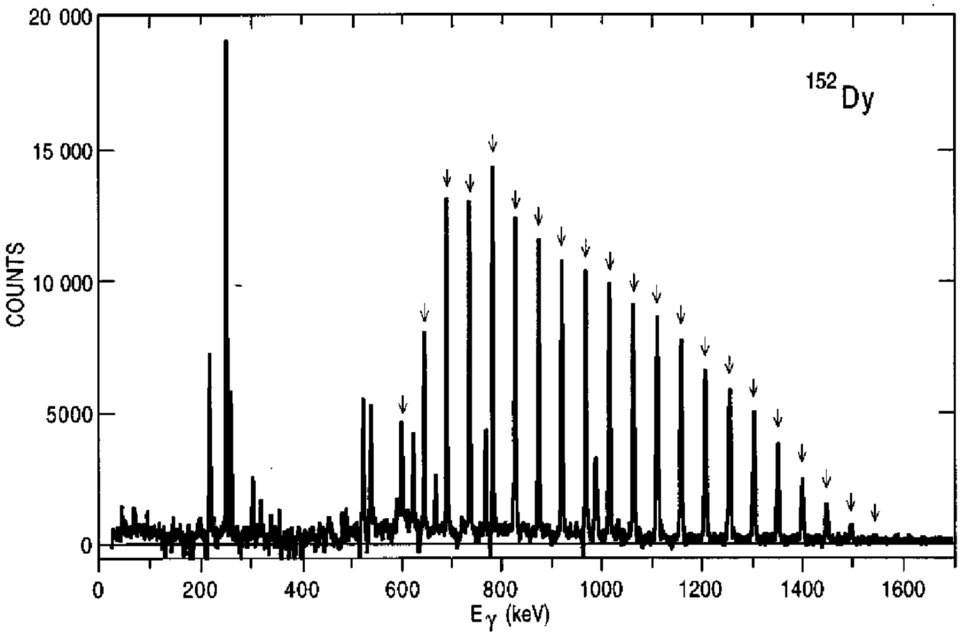

Figure 1.7: A spectrum showing a superdeformed rotational band in ^{152}Dy, with the relevant gamma-ray transitions marked. The constant spacing between the gamma-ray energies is characteristic of a purely collective rotational band. Other gamma-rays correspond to transitions from lower levels with normal deformation, populated after decays out of the superdeformed band. The figure is from Ref. [7].

and 1.8 the spacing between the sequence of gamma rays ($\Delta E_\gamma = 47$ keV) corresponds to $4\hbar^2/I$, which implies a quadrupole deformation β of about 0.6. The ^{152}Dy measurement of Ref. [8] was the first experimental evidence for superdeformation. While the ground and low lying excited states have a normal deformation of about 0.15, shape coexistence emerges for high-spin in the form of this rigid rotational band with high deformation. Superdeformation has been found in many different mass regions, and occurs when the potential energy surface as a function of β has a second minimum beyond the normal minimum for a spherical or lightly deformed shape. There is evidence of a third minimum known as hyperdeformation [9, 10, 11], corresponding to an axis ratio of 3:1, which is only observable at the absolute frontier of angular momentum. Beyond this extreme deformation, the nucleus becomes unstable to fission due to centrifugal forces.

Rotational band structures and the coexisting nuclear shapes they represent can mix, even to the point of crossing over. This manifests in a plot of the moment of inertia vs rotational frequency (i.e. $2I/\hbar^2 \equiv (4J-2)/E_\gamma$ vs. $\hbar\omega \equiv E_\gamma/2$) having an unmistakable "backbending" shape, where the gamma-ray energies suddenly decrease at a certain angular momentum before turning around and increasing again, this time with a higher moment of inertia. The microscopic explanation for this behavior involves so-called intruder orbitals, like $1h_{11/2}$ in Figure 1.5. These orbitals have the highest j in their respective shells due to being lowered in energy by the spin-orbit coupling. The rotational modes of the bands interact through a Coriolis force on the nucleons within the intruder orbital [3]. This force aligns the angular momentum of the nucleons with collective angular momentum from the rotation, and is stronger for higher j. The force will break a pair of nucleons within the intruder orbital and align each of their individual $\vec{j}$ with the angular momentum of the core. This causes the sudden decrease in gamma-ray energies at the location of the backbending in plots comparing energy and angular momentum, and represents a transition from states that are purely collective to states that have two unpaired nucleons not following the collective motion. This phenomena exemplifies the powerful interplay between single-particle and collective degrees of freedom.

The study of collective phenomena using high angular momentum has been expansive. However, experimental limitations have prevented studies from exploring nuclei with an excess of neutrons until recently. There remain many important open questions about the evolution of collective phenomena away from stability, and the answers lie in the extremes of both spin and isospin.

1.2 Nuclear Structure of the Calcium Isotopes

The chain of calcium isotopes provides an ideal testing ground for nuclear structure models, in terms of both the single-particle and collective properties of atomic nuclei. Recent experimental and theoretical efforts have aimed at exploring the rapid evolution of the shell structure of these nuclei out to the neutron dripline [12, 13, 14, 15, 16, 17, 18, 19, 20, 21]. The recent discovery of ^{60}Ca at N=40 implies that the Ca dripline should extend to at least ^{70}Ca [14]. Meanwhile, gamma-ray spectroscopy has identified new magic numbers of $N = 32$ and $N = 34$ for ^{52}Ca [15, 16] and ^{54}Ca [17] respectively, with confirmation from mass measurements [18, 19]. For ^{52}Ca, an unexpectedly large charge radius found in Ref. [20] has posed challenges for theoretical interpretation, while recent density functional theory has successfully reproduced the observed trends of charge radii from ^{36}Ca all the way to ^{52}Ca [21]. This theory also addressed the importance of continuum effects in understanding the structural evolution in the isotopic chain.

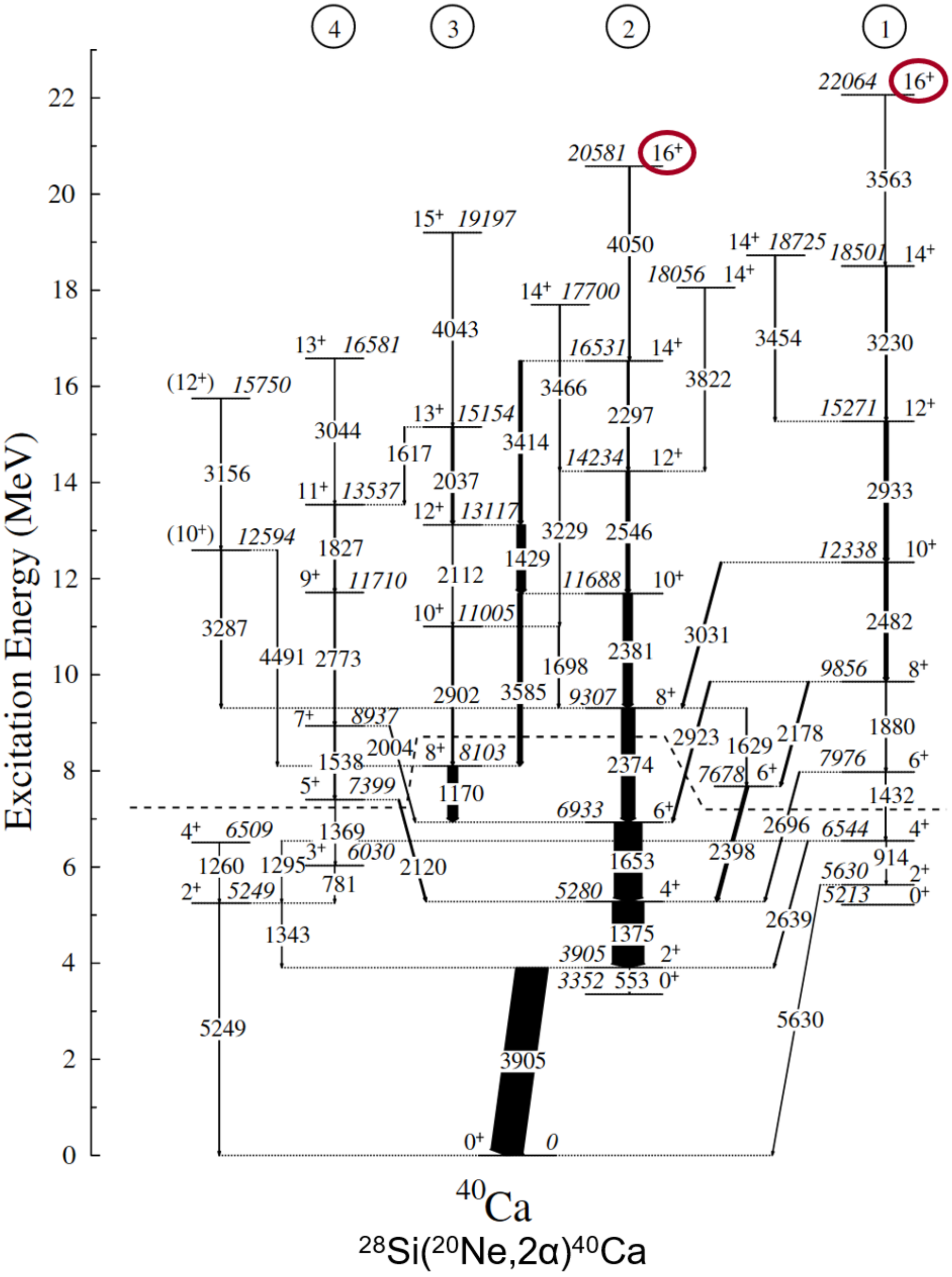

Figure 1.8: A level scheme showing band structures built on 0^+ excited states (labelled 1 and 2) in ^{40}Ca, populated in a fusion-evaporation reaction. Band 1 is superdeformed ($\beta \approx 0.6$) and associated with the $\pi 1f_{7/2}^4 \nu 1f_{7/2}^4$ configuration. The figure is adapted from Ref. [22].

While the isospin frontier has been the focus of many recent efforts in nuclear structure studies, the study of medium- to high-spin states remains an important challenge for neutron-rich nuclei [23, 24, 25, 26]. For calcium isotopes, studies of high-spin structures have reached ^{40,42}Ca [22, 27], with pronounced shape coexistence identified for the low-lying 0^+ states and multiple band structures, extending to 16^+ in ^{40}Ca (Figure 1.8). For ^{44}Ca, a negative-parity rotational band from 3^- to 13^- was proposed [28] based on the $J(J+1)$ trend of its energy levels. Shape coexistence is expected to persist in heavier calcium isotopes (Figure 1.9) [29], where the energy relation between spherical and deformed states may evolve far from stability, as seen in other neutron-rich regions including along the $N = 20$ and $N = 50$ isotones [30, 31, 32]. Expanding our knowledge of these deformed bands in the Ca isotopes and characterizing their evolution toward doubly-magic ^{48}Ca and beyond would give insight into the interplay between isospin and angular momentum and allow one to test advanced theoretical models that have been developed to describe low-lying structure of neutron-rich Ca isotopes [12, 17, 21, 33, 34, 35].

Previous investigations into ^{46}Ca have not uncovered the underlying band structure of the nucleus. Through particle spectroscopy, several excited states have been identified, using for instance $^{44}\mathrm{Ca}(t,p)$ [36], $^{48}\mathrm{Ca}(p,t)$ [37], and $^{46}\mathrm{Ca}(p,p')$ [38]. However, gamma-ray spectroscopy has generally been limited to studies of low-lying and low-spin states [39]. A recent β^--decay measurement has identified 42 new excited states in ^{46}Ca [40], but no band structures were observed due to the selective population of low-spin states by the β^- decay of ^{46}K with $J^{\pi}_{gs.} = (2^-)$. As shown in previous work for ^{40,44}Ca [22, 28], fusion-evaporation reactions can be used effectively to study band-structures due to selective population of high-spin states, particularly the yrast states; however, no stable beam and target combination is capable of reaching ^{46}Ca with sufficient intensity, calling for a new experimental approach.

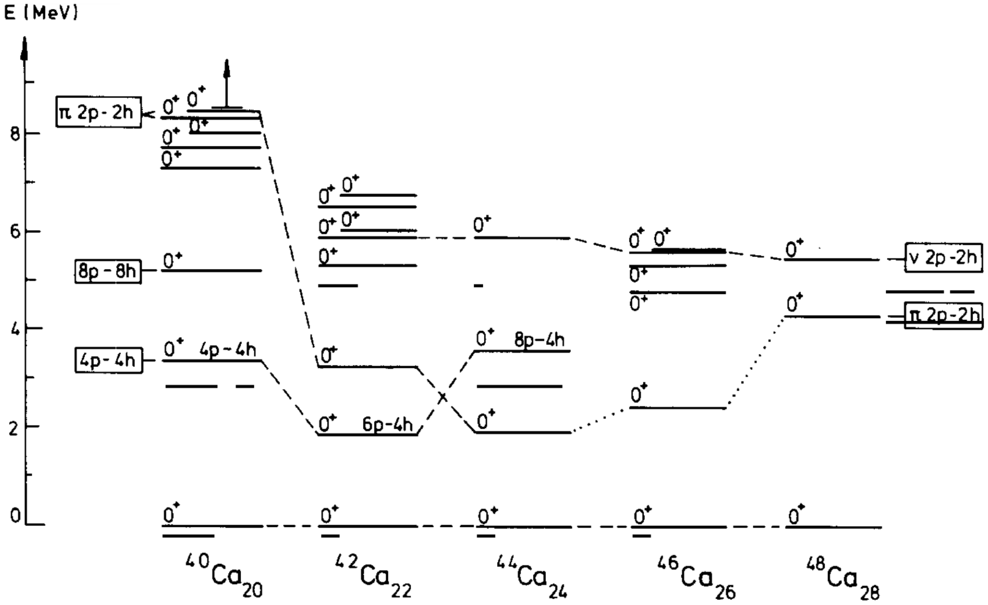

Figure 1.9: Systematics of the dominant particle-hole structure of excited 0^+ states in $^{40-48}$Ca. This shape coexistence impacts the band structures built on each of the 0^+ states. The figure is from Ref. [29].

For this work, the study of ^{46}Ca is enabled using a rare-isotope (RI) beam to induce several reactions that have not previously been measured.

1.3 Nuclear Reactions

Nuclear reactions can be divided into direct and compound reactions based on the energies and timescales involved. In direct reactions, the projectile and target nuclei are only within the range of the nuclear force for a short period of time, which leads to a minimal number of their component nucleons to interact with one another. Compound reactions create a long-lived compound nucleus, in which all nucleons interact until reaching equilibrium. The former is thought of as a one-step process, while the number of steps in compound reactions is too many to handle without using statistical methods.

1.3.1 Direct Reactions

Direct reactions are widely used to precisely study microscopic nuclear interactions. The one-step process in which only a few nucleons interact grants advantages in examining the single-particle or cluster character of the nuclei involved in the entrance and exit channels. By choosing nuclear reactions that only excite a few simple degrees of freedom, valuable structural information can be effectively probed.

Theoretical treatments for direct reactions are robust and can be compared to experimental measurements like cross sections to extract information about the reaction dynamics and the interacting nuclei, including spectroscopic factors. Spectroscopic factors quantify the amount of correlation in the single-particle wave functions across the entrance and exit channels of the reaction. In this way, studies of direct reactions can demonstrate how purely single-particle in nature a particular nuclear state is. In particular, nuclear astrophysics relies on the predictive power of these theoretical calculations due to the difficulty of producing reactions that occur in stellar environments in the laboratory.

Transfer reactions have historically been the workhorse of spectroscopy with direct reactions. (p,d), (d,p), (d,n), (^{3}He,d), and (d,^{3}He) were used frequently, as well as two-nucleon stripping and pickup transfers like (t,p) and (p,t). Two-particle transfers could access additional states, but have much lower reaction rates and are more difficult to theoretically model. Even more complex are multi-nucleon, or cluster, transfers. These include alpha-triton cluster transfer, relevant for ^{7}Li reactions.

1.3.2 Compound Reactions

The theory of compound nucleus reactions was proposed by Bohr in 1937 [41]. He proposed a two-step process beginning with the capture of the projectile by the target nucleus, followed by subsequent particle and gamma decays. This compound nucleus formation involves many nucleon-nucleon interactions, to the point that the system reaches complete statistical equilibrium. This requires the compound nucleus to live much longer than the duration of the typical direct reaction ($10^{-19} - 10^{-16}$ s rather than 10^{-22} s). The highly excited compound nucleus, which is also formed with high spin due to the conservation of angular momentum, then emits neutrons, protons and alpha particles in a statistically determined series of decays, until reaching the ground state of a residual nucleus through gamma decay. Due to the equilibrium of energy, the decays of the compound nucleus should not depend on how the nucleus was formed; this is referred to as the independence hypothesis. Modern models of compound nucleus decay use the Hauser-Feshbach formalism [42], which only incorporates the mass, atomic number, excitation energy, and angular momentum of the compound nucleus. The first experimental evidence of the independence hypothesis is shown in Figure 1.10.

In real cases, direct and compound nucleus reaction mechanisms often compete in a single experiment. Long-lived resonances and multi-step processes complicate attempts to theoretically model the reaction. For example, incomplete fusion channels in lithium-induced reactions have been shown to potentially be limited in the angular momentum transferred to the residue [26]. Achieving a better understanding of lithium-induced reactions is an active area of research.

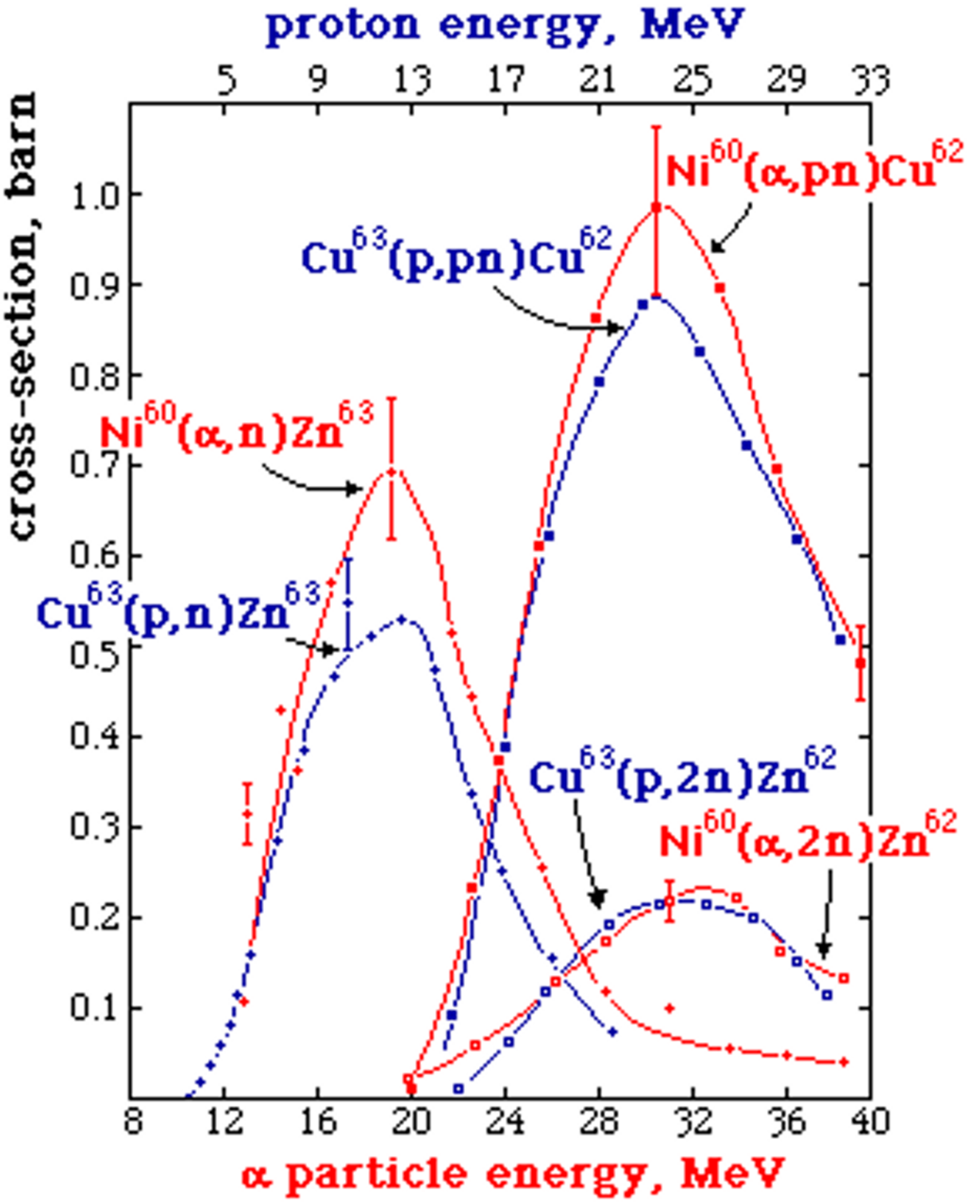

Figure 1.10: Excitation functions for proton and alpha induced reactions with ^{63}Cu and ^{60}Ni, showing correspondence between reaction channels that produce the same compound nucleus. This implies a level of independence in how a compound nucleus decays once it is formed. The figure is adapted from Ref. [43].

Chapter 2

Experimental Techniques

This dissertation focuses on an experiment that studied nuclear structure by employing nuclear spectroscopy with a reaccelerated rare-isotope (RI) beam. The measurement is based on particle-gamma coincidence. In this chapter, three of the techniques necessary to perform the experiment are detailed. First, the principles and operation of semi-conductor detectors are described, forming the foundation of our gamma-ray and charged particle detection. Then, in-flight gamma-ray spectroscopy is discussed, which provided the basis for discovering new nuclear excited states in this measurement. Finally, the application of nuclear reactions at Coulomb-barrier energies to explore neutron-rich nuclei is addressed.

2.1 Semiconductor Detectors

In semiconductor detectors, electron-hole pairs serve as information carriers and are produced along the path of a charged particle through the detector. Collecting these electron-hole pairs after they move in an applied electric field generates the detector signal (Figure 2.1). Charged-particle semiconductor detectors are typically made from silicon, whereas gamma-ray detectors tend to be made from germanium due to the larger atomic number Z.

In crystalline solids, energy bands form for electron energies. In the case of metals, the highest occupied energy band is not full, and valence electrons can travel throughout the material. For insulators, valence electrons do not contribute to the solid's conductivity,

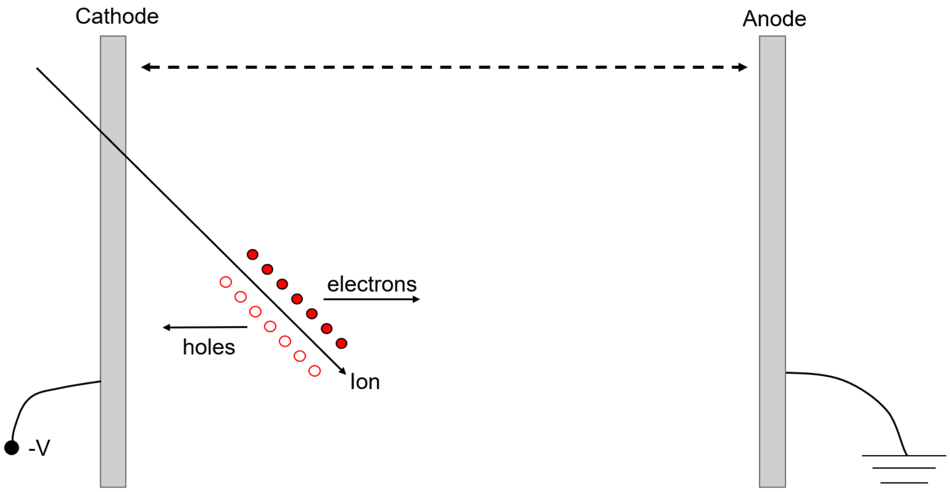

Figure 2.1: A diagram of a semiconductor detector, showing the electron-hole pairs being created and moved by the applied electric field between the electrodes.

and must be excited to the conduction band, where the electrons are free to migrate. The band gap between the valence and conduction bands leads to much lower conductivities than metals. Semiconductors are materials with band gaps that are considerably less than 5 eV. When promoting a valence electron to the conduction band, a corresponding hole is created in the valence band. Both the particle and virtual particle move when subjected to an external electric field, but in opposite directions.

Thermal generation of electron-hole pairs is an important limiting factor for semiconductor detectors. The probability per unit time of a thermally excited electron is

$$p(T) = CT^{3/2} \exp\left(-\frac{E_g}{2kT}\right) \tag{2.1}$$

where T is temperature in Kelvin, E_g is the band gap energy, k is the Boltzmann constant, and C is a constant dependent on the material. There is a strong dependence on the ratio between the band gap and temperature. This explains why silicon detectors, with a band gap of 1.14 eV, can be operated at room temperature, whereas germanium detectors ($E_g = 0.67$

eV) should be cooled to liquid nitrogen temperatures.

Intrinsic semiconductors are atomically pure and have distinct valence and conduction bands. Such is the case for the gamma-ray detectors used in this experiment, which consist of high-purity germanium (HPGe) crystals. However, producing silicon detectors of a requisite purity for the purpose of charged-particle detection would be very difficult, and any impurities present would dominate the properties of the material. Because of this limitation, semiconductor detectors are often doped with other atoms. When doped with a pentavalent element like phosphorus, additional donor electrons occupy levels just below the conduction band, in a region normally forbidden in intrinsic semiconductors. These electrons are compensated by ionized phosphorus atoms, which do no act as holes because they are locked in place in the lattice at the donor site. The increased number of electrons increases the probability of recombination with holes, and thus decreases the number of holes. However, the total number of carriers will be much higher than for the corresponding intrinsic material, improving the material's conductivity. The n-type semiconductor described here has its dual in a p-type semiconductor doped with a trivalent element like boron, producing an acceptor level and an excess of holes, which would serve as the majority charge carrier (see Figure 2.2).

When ionizing radiation loses energy within a semiconductor, that energy is converted directly or indirectly to electron-hole pairs along the path of the particle. The energy to create one pair is independent of the particle's properties and is slightly higher than the band gap energy, which is 3.62 eV for silicon (at 300 K) and 2.96 eV for germanium (at 77 K). This allows for a direct conversion between the average number of electron-hole pairs observed and the energy of the incident radiation. The deviation of the intrinsic energy resolution with respect to statistical fluctuations given by the number of charge carriers is

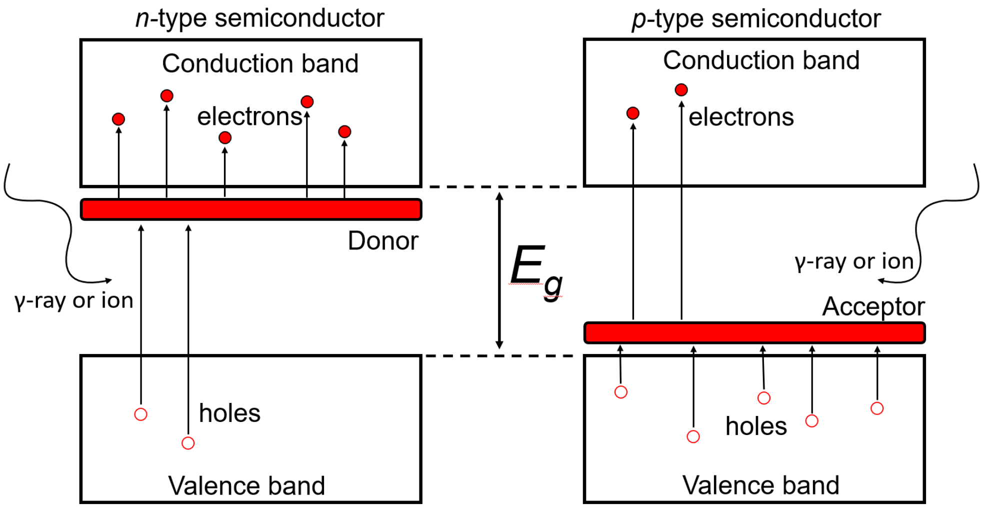

Figure 2.2: An energy diagram of n-type and p-type semiconductor responses to ionizing radiation. The effects of doping on the dominant charge carriers are depicted.

quantified by the detector's Fano factor (about 0.115 for silicon and 0.13 for germanium [44]).

The charges of electron-hole pairs are collected by electrical contacts and generate a pulse. The voltage applied to produce the necessary electric field is typically hundreds of volts, and small conductivity present in the detector will create a leakage current. Fluctuation in the leakage current causes noise in the resulting pulse, potentially obscuring the signal voltage. Therefore, a very low conductivity is preferred to minimize leakage current, as well as improve charge collection efficiency. A detector dead layer typically occurs near the electrodes where collection is inefficient, leading to insensitivity to radiation in the region.

In order to account for a detector dead layer, the effective dead layer thickness must be measured experimentally. Typically this is accomplished by varying the angle of incidence of a monoenergetic charged particle source [45]. As a function of angle of incidence θ, the energy loss due to dead layer is

$$\Delta E(\theta) = \frac{dE_0}{dx}\frac{t}{\cos\theta} \tag{2.2}$$

where dE_0/dx is stopping power and t is the effective dead layer thickness. Thus, by plotting the observed energies against $1/\cos\theta$, a linear trend should emerge with slope equal to dE_0/dx times t. Comparison with a range table for the chosen charged particle and detector material will give an effective dead layer thickness. There are higher order effects present, like the dependence of particle energy loss on the direction traveled relative to the detector's electric field, which could introduce nonlinearity in the trend described above.

2.2 In-Flight Gamma-Ray Spectroscopy

Gamma rays carry no charge and thus cannot directly interact with charged particles in atoms within an absorbing material through Coulomb interactions [45]. Unlike the detection of charged particles, detection of gamma rays must be carried out indirectly through interactions that transfer a photon's energy to electrons. These interactions, summarized below, occur suddenly and have significant effects on the photon's properties, in contrast with the many interactions of charged particles that continuously reduce the particle's kinetic energy. After the incident gamma ray has deposited some or all of its energy through these interactions, the subsequent free electrons lose energy through ionizing and exciting atoms in the material. Therefore, a gamma-ray spectrometer must serve both as a site for gamma-ray interactions and as a conventional detector to measure the subsequent electron energies.

2.2.1 Gamma-Ray Interactions with Matter

The three relevant ways in which gamma rays interact with matter are photoelectric absorption, Compton scattering, and pair production. Each involves photons transferring all or some of their energy to electrons, which are then slowed through the continuous inelastic

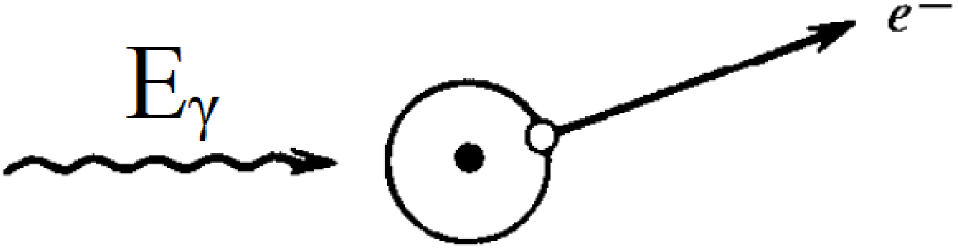

Figure 2.3: A diagram of the photoelectric effect. The incident photon is replaced with an emitted photoelectron originating from one of the electron shells in the absorber atom. The figure is adapted from Ref. [45].

collisions, characterized as a material's stopping mechanism [46]. The processes differ in several ways explained below, including the gamma-ray energy regime in which they are predominate over other gamma-ray interactions.

The photoelectric absorption process involves an incident photon interacting with an atom and an ejected photoelectron taking its place. For typical gamma-ray energies, this freed electron most likely originates from the lowest-lying atomic energy levels of the atom. The energy of this free electron is given by

$$E_{e^-} = E_\gamma - E_b \tag{2.3}$$

where E_γ is the photon energy and E_b is the binding energy of the electron. This binding energy can be several keV and increases with increasing atomic number (e.g. For Germanium atoms, the K shell binding is 11.1 keV.). There is also the small recoil of the atom owed to the conservation of momentum, but it can be ignored both with this process and later in this section. Consequently, a large majority of the incident gamma ray energy is carried away by the photoelectron. The binding energy is liberated through electron deexcitation followed by emission of X-rays or Auger electrons, which travel a short distance on the order of a millimeter before being reabsorbed. Therefore, assuming an interaction point several millimeters from the edge of the detector volume, it is very likely in the case of photoelectric absorption that all of the incident gamma-ray energy is captured by the detector. Therefore in a gamma-ray energy spectrum, this process yields a single peak referred to as a full-energy peak.

Because of the complete retention of the incident gamma-ray energy, photoelectric absorption is the most preferred mode of interaction in gamma-ray spectroscopy. Thus, maximizing its cross section is central to the design and specifications of gamma-ray detectors. The photoelectric process dominates for low energy gamma rays and is greatly enhanced for detector materials with high atomic number Z compared to other processes (see Figure 2.4). Generally, the cross section is roughly proportional to

$$\frac{Z^n}{E_\gamma^{3.5}} \tag{2.4}$$

where n falls roughly between 4 and 5 depending on gamma ray energy E_γ. This strong Z dependence is the reason that gamma-ray detectors are made from high-Z materials and that lead is used in gamma-ray shielding.

Compton scattering occurs when the incident gamma-ray photon is deflected after transferring energy to a recoil electron, as in Figure 2.5. The transferred energy varies along with the scattering angle θ relative to the incoming photon direction. If one neglects the binding energy of the electron and instead assumes a free electron, one can evaluate the outgoing gamma-ray energy as a function of incident energy and scattering angle using conservation of momentum and energy:

$$E'_\gamma = \frac{E_\gamma}{1 + \frac{E_\gamma}{m_0 c^2}(1 - \cos\theta)} \tag{2.5}$$

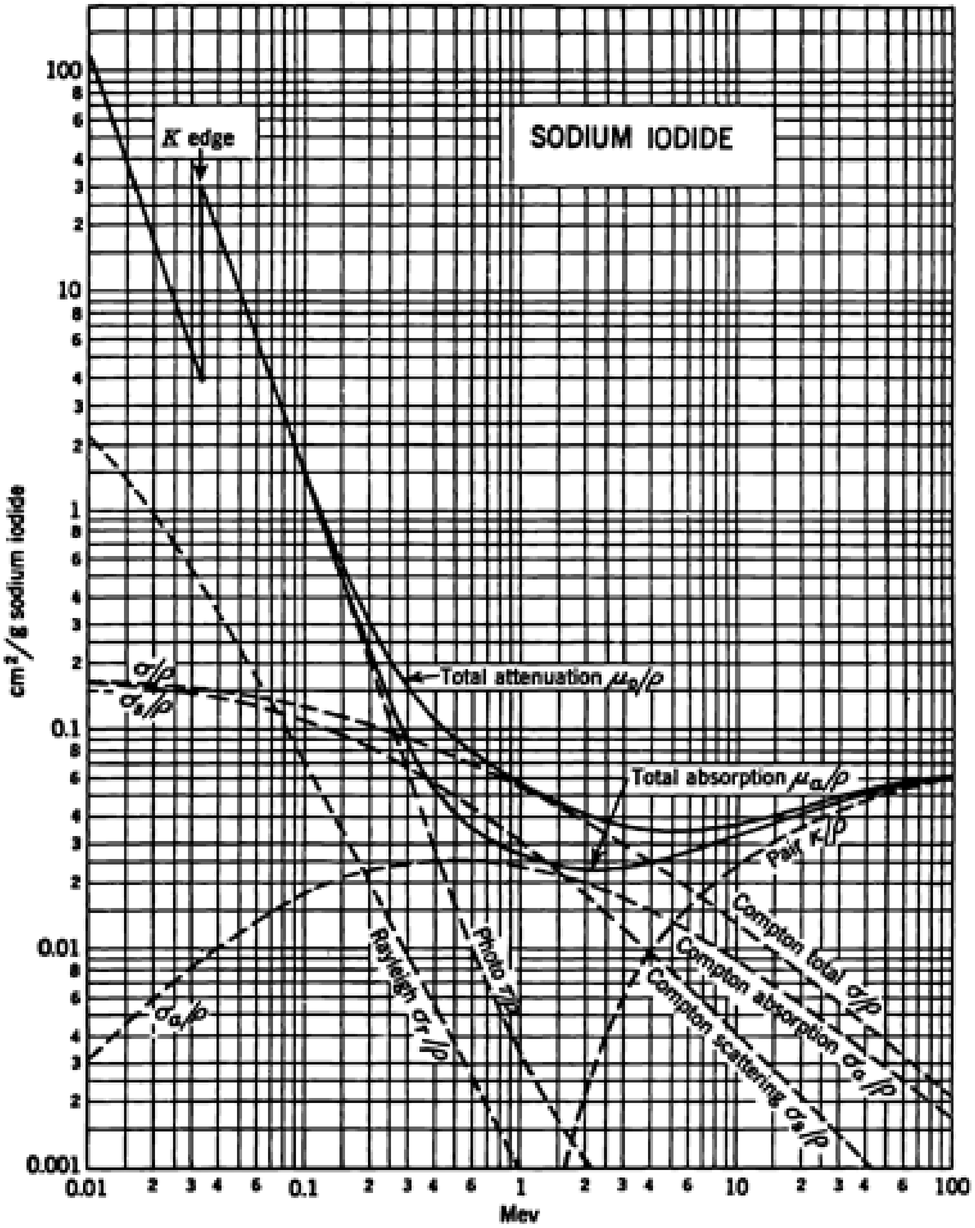

Figure 2.4: Energy-dependent attenuation coefficients for several gamma-ray interactions in sodium iodide. The figure is from Ref. [47].

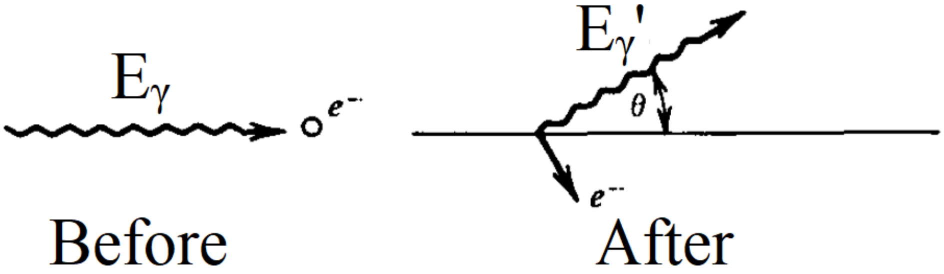

Figure 2.5: A diagram of Compton scattering. The incident gamma-ray energy is distributed between the scattered photon and the recoiling electron according to the scattering angle θ. The figure is adapted from Ref. [45].

where $m_0c^2 = 511$ keV is the electron's rest mass. The electron's kinetic energy is then

$$E_{e^-} = E_\gamma - E'_\gamma = E_\gamma \frac{(E_\gamma/m_0c^2)(1-\cos\theta)}{1+(E_\gamma/m_0c^2)(1-\cos\theta)} \tag{2.6}$$

There are two extreme cases to be discussed. If $\theta = 0$, the photon is not deflected and $E_{e^-} = 0$. On the other hand, if $\theta = \pi$

$$E'_\gamma|_{\theta=\pi} = \frac{E_\gamma}{1+2E_\gamma/m_0c^2} \tag{2.7}$$

$$E'_{e^-}|_{\theta=\pi} = E_\gamma \frac{2E_\gamma/m_0c^2}{1+2E_\gamma/m_0c^2} \tag{2.8}$$

Since any scattering angle between 0 and π is possible, E_{e^-} can range from 0 to the value in equation 2.8. If a gamma-ray detector is small compared to the mean-free path of the scattered gamma ray, it is likely that only the energy of the recoil electron will be deposited in the detector. This leads to a continuum of Compton-related measured energies up to the maximum, known as the Compton edge. The scattered photon could Compton scatter again, or be absorbed, leading to total energy in the detector below or equal to the full

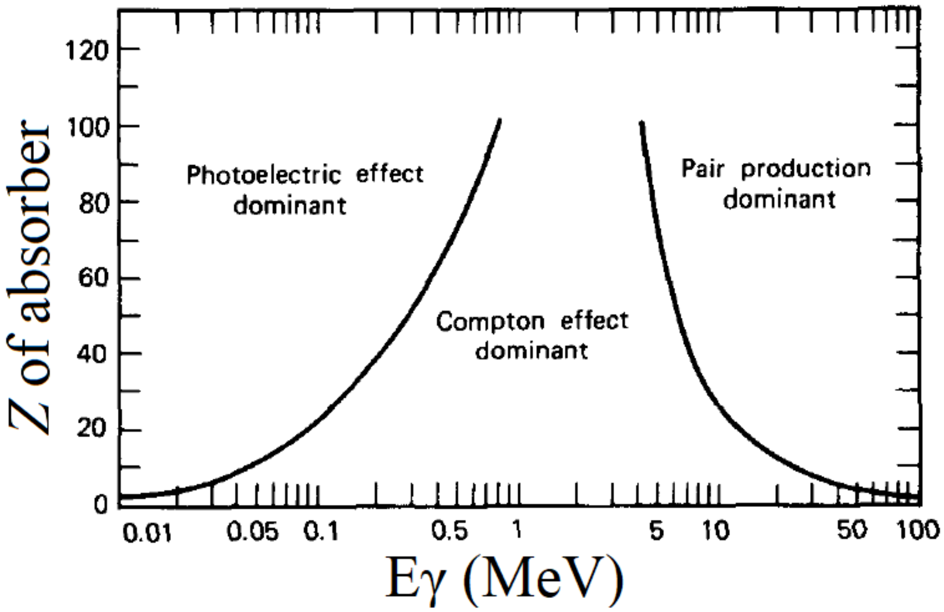

Figure 2.6: A plot showing which interaction dominates depending on the gamma-ray energy and absorber atomic number. The figure is adapted from Ref. [47].

energy, respectively. Compton scattering interactions are dominant over other processes at gamma ray energies between several hundred keV and several MeV, depending on the atomic number Z of the absorbing material (see Figure 2.6). The cross section of this interaction is determined by the Klein-Nishina formula, and increases linearly with Z [48].

For high energy gamma rays, in particular in an energy region far above $2m_0c^2 = 1.02$ MeV, the pair production interaction dominates. In this process, the gamma ray interacts with the electric field caused by the protons in the atoms of the material. Given the shielding that atomic electrons provide, it is reasonable that the cross section of this process is much higher for more probing, higher energy photons. The exact analytic form of the cross section for pair production is calculated through quantum electrodynamics by using Feynman diagrams, and the result is a complicated function that scales to first order by Z^2.

Through this interaction, an electron-positron pair is created in place of the gamma-ray.

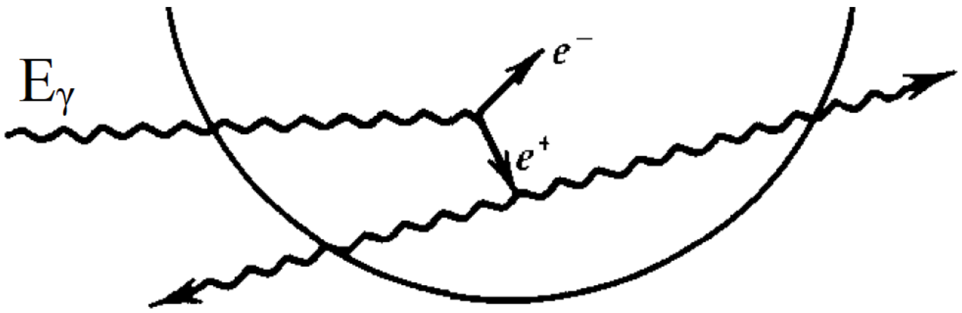

Figure 2.7: A diagram of pair production. The incident gamma ray is replaced with a positron and electron, with the incident energy converted to both kinetic energy of the pair as well as their masses (511 keV/c^2). The positron then annihilates with another electron producing two 511 keV gamma rays. In the diagram shown, both gamma rays escape the detector volume. The figure is adapted from Ref. [45].

The total kinetic energy of the pair is equal to $E_\gamma - 2m_0c^2$. The two particles travel a few millimeters at most in the detector, at which point the positron annihilates with a normal electron in the material to produce two 511 keV gamma rays. If one or both of these gamma rays exit the detector, then the total energy absorbed will be 1 or 2 m_0c^2 less than the full E_γ, yielding a single- or double-escape peak in the resulting detector response. An example response function for a gamma-ray detector is shown in Figure 2.8.

A fourth type of gamma-ray interaction with matter is Rayleigh scattering, which is essentially equivalent to elastic scattering for particle interactions. Since this interaction deposits nearly zero energy in the detector, its effect on detector response is minor. However, in order to correctly model gamma-ray transport, the chance of Rayleigh scattering should be included in simulations. The mean amount of deflection decreases quickly with increasing gamma-ray energy, so its relevance is limited to incident energies below a few hundred keV.

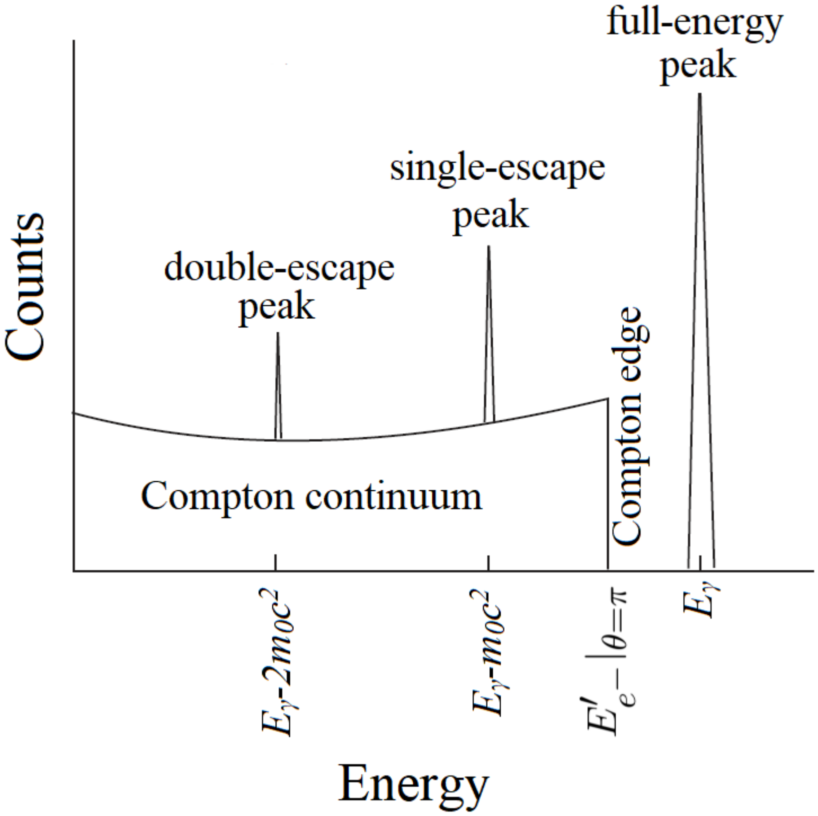

Figure 2.8: An illustration of a typical gamma-ray detector response to a monoenergetic gamma-ray source. It shows several features caused by different gamma-ray interactions and their associated energies, including the full-energy peak for events in which no secondary gamma ray or electron escapes the detector, Compton events in which a scattered gamma ray only deposits partial energy, and events creating escape peaks in which an electron and/or position carry away energy in the form of their rest mass.

2.2.2 Relativistic Doppler Shift

If an excited atomic nucleus is moving at a significant percentage of the speed of light, a stationary observer can observe gamma rays emitted in-flight. These gamma rays would experience a Doppler effect due to special relativity, leading to a difference in the observed gamma-ray energy and one observed from a stationary decay. Since projectile-frame gamma-ray energies correspond to the transition energies among nuclear bound states, correcting for this Doppler shift is necessary for in-flight gamma ray measurements.

Akin to the classical Doppler effect, the amount of Doppler shift modifies the frequency of the gamma ray, and is dependent on the velocity of of the source with respect to the gamma-ray emission direction. The Doppler-shifted energy of a gamma ray observed in the laboratory frame is

$$E_{Lab} = \frac{E_{CM}}{\gamma\,(1 - \beta\cos\theta)} \tag{2.9}$$

where E_{CM} is the energy of the gamma ray in the projectile's frame of reference, β is ratio of the projectile velocity to the speed of light ($\beta = v/c$), θ is the laboratory frame angle between the gamma ray's angle of emission and the projectile's velocity vector, and γ is the Lorentz factor

$$\gamma = \frac{1}{\sqrt{1-\beta^2}}. \tag{2.10}$$

The Doppler shift increases with increasing β, while for a stationary nucleus, $E_{Lab} = E_{CM}$ as expected. The Doppler shift is positive for forward angles ($\theta < \pi/2$) and negative for backward angles ($\theta > \pi/2$). This leads to a Doppler-spreading effect in laboratory-frame gamma-ray energy spectra when decays occur at low but significant velocities ($3\% < \beta < 7\%$ in this work).

One can correct for the observed energy of a Doppler-shifted gamma ray by inverting equation 2.9

$$E_{DC} = E_{Lab}\gamma\left(1 - \beta\cos\theta\right). \tag{2.11}$$

This Doppler-shift corrected energy depends not only on E_{Lab}, but also β and θ. Therefore the three contributions to the resolution of E_{DC} are added in quadrature [49]:

$$\left(\frac{\Delta E_{DC}}{E_{DC}}\right)^2 = \left(\frac{\beta\sin\theta}{1-\beta\cos\theta}\right)^2 (\Delta\theta)^2 + \left(\frac{\cos\theta - \beta}{\left(1-\beta^2\right)\left(1-\beta\cos\theta\right)}\right)^2 (\Delta\beta)^2 + \left(\frac{\Delta E_{Lab}}{E_{Lab}}\right)^2. \tag{2.12}$$

In this work, measurements of E_{Lab} and θ were performed using a segmented gamma-ray detector, and an average β was deduced from the observed angular dependence of the Doppler-shift effect on gamma ray energies. The intrinsic resolution of the detector ($\Delta E_{Lab} = 3$ keV) was small enough to ignore, and so the Doppler-shift corrected energy resolution was primarily dependent on $\Delta\theta$ and $\Delta\beta$. The contributions for $\Delta\theta$ include uncertainties in the decay position and the gamma-ray interaction points in the detector, as well as uncertainty in trajectory of the decaying nucleus. It must be noted that, due to the fact that the error of the measurement of β was dependent on the measurement of θ in this case, Equation 2.12 would be an incorrect use of the quadrature rule for uncertainties. However, for this experiment at Coulomb-barrier energies, the magnitude of the Doppler shift was small enough that the corresponding covariance term should not contribute significantly. This assumption for Doppler-corrected energy resolution was corroborated by reproducing the observed energy resolutions from Doppler broadening with Monte Carlo based simulations, as shown in Chapter 4.

2.3 Compound Reactions as a Spectroscopic Tool with Rare-Isotope Beams

For several decades, heavy-ion fusion-evaporation reactions have been the primary method of studying high-spin excited states in nuclei when combined with gamma-ray spectroscopy. Each possible choice of beam and target combination can produce a wide yet still selective range of nuclei, compared to alternatives like deep-inelastic heavy-ion collisions. However, until recently these studies have been limited to stable beams, which leads to evaporation products being almost exclusively restricted to neutron-deficient nuclei. By using neutron-rich rare-isotope (RI) beams, new structures in exotic nuclei can be explored. With the advent of reaccelerator facilities [50, 51, 52], rare-isotope beams at Coulomb barrier energies have become available, allowing us to take advantage of fusion and pre-equilibrium reaction mechanisms with a novel combination of beam and target [53]. Moreover, before the low-energy RI beams were available, these reactions were performed in normal kinematics. The implementation of reactions with light targets in inverse kinematics has many benefits beyond the expanded scope offered by the exotic beam, including improved Doppler-correction in this work.

Two major production methods for low-energy RI beams are the isotope separation on-line (ISOL) and fragmentation techniques. ISOL production uses a high-intensity beam of protons to impinge on a heavy production target, for instance uranium carbide (UCx). The resulting fragmentation products from the reaction are thermalized in the target and slowly diffuse out to an ion source for ionization and separation. The isotope separation process creates a chemistry dependence on the available beams. Major ISOL facilities include TRIUMF-ISAC [54] and REX-ISOLDE [55]. The NSCL uses the latter fragmentation technique, in which fragmentation products are separated in-flight before being stopped and reaccelerated at lower energies. This procedure is described further in Chapter 3.

The reactions used with RI beams differ for high- and low-energy experiments. For instance, Coulomb excitation was traditionally done at energies below the Coulomb barrier. This ensured that the target and projectile nuclei would only undergo electromagnetic interactions. Once fast RI beams became available, new techniques like intermediate-energy Coulomb excitation were developed [49]. These experiments are more selective in what states they populate because the shorter interaction time only allows for one-step excitations, but the substantial cross sections and the ability to use thicker targets provide many advantages compared to barrier-energy Coulomb excitation. Another reaction mechanism used in conjunction with high-energy beams is knockout [56]. Related to low-energy transfer reactions, knockout is more direct to the point that only the nucleons removed from the heaver projectile interact with the target, allowing a semiclassical description of the reaction based on the impact parameter. Knockout reactions are very selective about populating states that reveal the single-particle character of the resulting nuclei.

For compound reactions including for fusion-evaporation, it is necessary to run experiments near Coulomb-barrier energies. For this reason, its application to newly available RI beams has been delayed until these beams could be developed at lower energies with high intensity, high purity, and quality emittance. Recently the capabilities for these methods have been developed at RIKEN [53], GANIL [57], and REX-ISOLDE [26], but the experiment presented in this thesis represents the first of such studies that involve gamma-ray spectroscopy at the NSCL. It is a primary goal of this work to kick-off spectroscopy studies of exotic, neutron-rich nuclei by employing this novel approach.

Chapter 3

Experiment

The present experimental work was performed at the National Superconducting Cyclotron Laboratory (NSCL) at Michigan State University. The NSCL is uniquely capable of delivering the high purity reaccelerated rare-isotope (RI) beams produced following projectile fragmentation using the combination of the A1900 fragment separator [58] and the reaccelerated beam facility (ReA3) [52]. This yields a chemistry-independent mechanism for the production and reacceleration of RI beams. In this study, a reaccelerated beam of ^{45}K impinged on a natural lithium target and produced a variety of reaction products, including potassium, calcium, scandium, and titanium, through both compound and direct reactions. Ejected light nuclei and emitted gamma rays were detected using a downstream silicon detector and the Segmented Germanium Array (SeGA), respectively. The novel approach for this experiment, based on the JANUS setup used for Coulomb excitation measurements [59], is further explained in the following sections.

3.1 Beam Production

The NSCL provides beams of exotic nuclei via projectile fragmentation. Stable nuclei are ionized in an ion source and accelerated in the coupled cyclotrons K500 and K1200 before being impinged in a thick ^{9}Be production target. The resulting collision fragments include many unstable isotopes in a cocktail secondary beam. A pure beam of the desired isotope is filtered from the others by the A1900 fragment separator.

In order to increase the yields for the desired RI beams, thick production targets and kinematic focusing for collision fragments are desired, necessitating high primary beam energies. Thus, the resulting secondary beam production energies must naturally be high. On the other hand, lower beam energies are often needed for many experimental applications, including this work, so to this end beams are slowed to thermal energies in a gas stopper. For experiments that need beam energies suitable for nuclear reaction studies, the rare isotope is stopped, undergoes charge breeding, and is accelerated again using a secondary linear accelerator, ReA3. ReA3 creates beams with Coulomb-barrier energy ($3 - 5$ MeV/u) with excellent beam emittance and well-defined energy width compared to the alternative procedure of slowing of the beam from production energies using an energy degrader in a single step.

Figure 3.1 shows the full NSCL facility. The full path of the beam for this experiment from the ion source, through the Coupled Cyclotron Facility and the A1900, through ReA3, and finally to the experiment's location in the ReA3 experimental hall will be explained in detail in the following sections, along with brief descriptions of each component to explain how the final beam is produced.

3.1.1 ECR Ion sources

To produce a rare-isotope beam at the NSCL, one must first start with a beam of stable ions, created with an ion source. The NSCL has two ion sources that are operated in alternating experiments: the Advanced Room Temperature Ion Source (ARTEMIS) [61] and the Superconducting Source for Ions (SuSI) [62]. SuSI is more efficient and can deliver higher average charge states than ARTEMIS; however, both are capable of producing the ions for

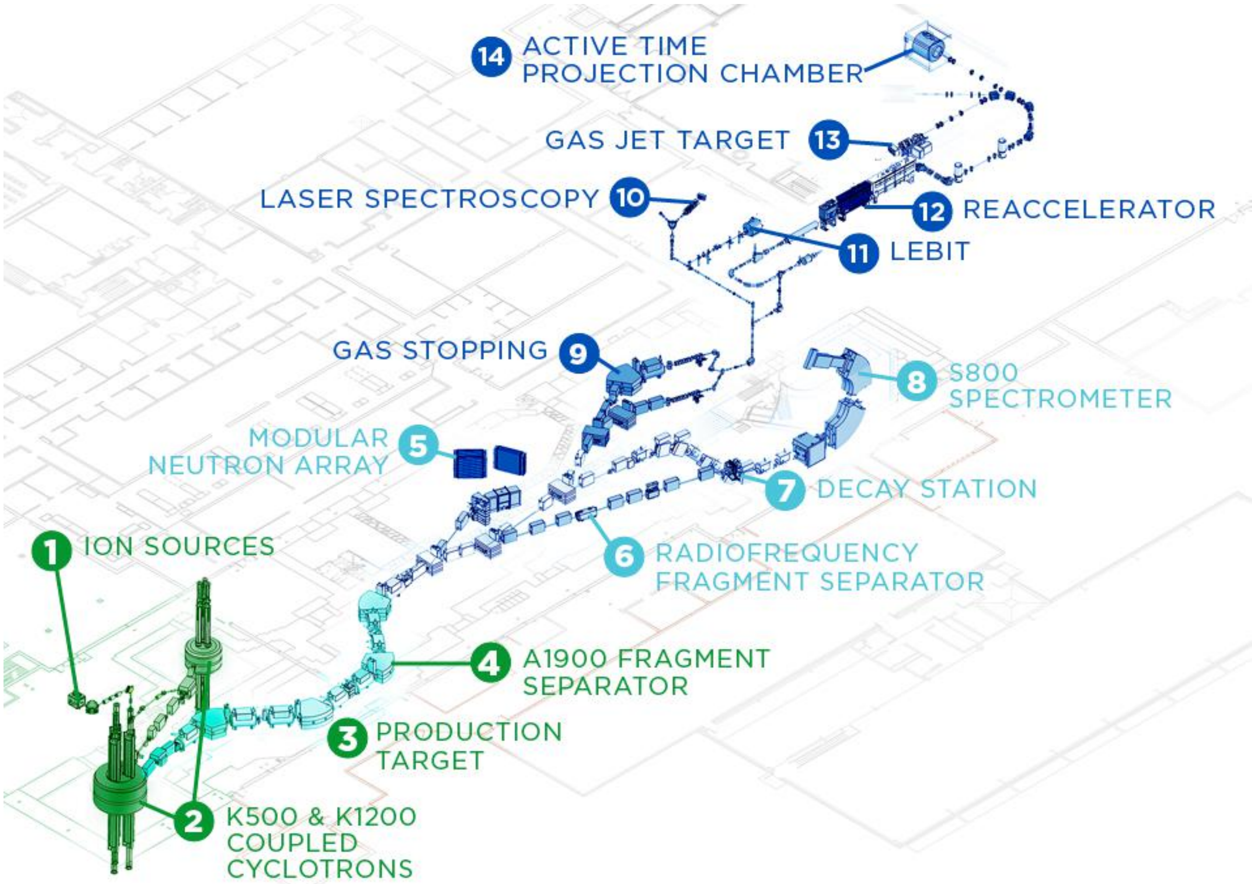

Figure 3.1: A diagram of the NSCL facility. The figure is from Ref. [60].

most beams at the NSCL. For this reason, typically one ion source supplies the current beam while the other is used to prepare the beam development for the following experiment.

SuSI and ARTEMIS are both electron cyclotron resonance (ECR) ion sources. The operation of ECR ion sources entails a gas of the desired ion kept at a low pressure (10^{-6} torr) [63]. In the case of this experiment, metallic ^{48}Ca was heated in an oven to create a ^{48}Ca gas. This gas is ionized into a plasma using a combination of microwaves and a confining magnetic field. Due to the radial hexapole magnetic field created by superconducting magnets, both the ions and free electrons in the plasma move in circles according to the cyclotron frequency:

$$\omega_c = \frac{qB}{m} \tag{3.1}$$

where q is the charge on the ion, B is the magnitude of the magnetic field, and m is the mass of the ion. The microwaves are tuned to the resonant frequency eB/m_e to selectively accelerate the free electrons. This ECR heating creates a positive feedback loop where free electrons collide with ions in the gas, further ionizing them and thus producing more free electrons. The end of this process occurs when ion-ion collisions provide an ion enough energy to escape axial confinement and exit the plasma. This is why the pressure of the gas must be low, otherwise ion-atom collisions would occur more quickly and reduce the average charge state of the exiting ions. In this experiment, the ^{48}Ca ions reached a charge state of 8^{+}. Finally, the ions are guided by the solenoidal field toward the K500 cyclotron.

3.1.2 The Coupled Cyclotron Facility

The Coupled Cyclotron Facility (CCF) comprises of a pair of couple superconducting cyclotrons, the K500 and K1200, which are responsible for the acceleration of stable primary beams at the NSCL. Cyclotron accelerators operate with a strong, static magnetic field that confines motion to a horizontal plane. Transverse motion of an ion in a magnetic field is governed by the Lorentz force law ($\vec{F} = q\vec{v} \times \vec{B}$), from which one can show that the radius of curvature ρ is

$$\rho = \frac{p}{qB} = \frac{\gamma m v}{qB} \tag{3.2}$$

where γ is the Lorentz factor, B is the magnetic field, and m, v, and q are the mass, velocity, and charge of the ion. Often this momentum per charge concept is expressed as an ion's magnetic rigidity, $B\rho$, measured in Telsa-meters. In addition to the magnetic field, an accelerating electric field is repeatedly applied to the ions by three large copper electrodes called dees. A radio-frequency alternating voltage across the dees is tuned to match the ion's cyclotron frequency. As the ions accelerate, the lengths of their paths around the cyclotron increase. To account for relativistic effects, the peripheral parts of the magnetic fields are nonuniform to increase B as velocity increases, while the RF remains constant. This type of cyclotron is described as isochronous, in reference to the constant frequency relative to ion energy. Eventually the ions achieve their maximum velocity possible at the outer edges of the cyclotron, at which point they are extracted.

The K500 and K1200 cyclotrons are coupled together to provide a staged acceleration. The K500 first accelerates the ions at the charge state received from the ion source. When emitted from the K500 and delivered to the K1200, ions have typical energies of 10-20 MeV. At the center of the K1200, the ions encounter a carbon stripper foil which further removes their electrons (^{48}Ca^{20+} in this work). This allows the K1200 to accelerate the ions to their maximum available energy. The names K500 and K1200 refer to the peak accelerating strength of the cyclotrons. Each number is a proton's kinetic energy in MeV after accelerating with the maximum magnetic field strength:

$$K = \frac{e^2}{2m_p}(B\rho)^2 \approx \left(48\frac{MeV}{(Tm)^2}\right)(B\rho)^2 \qquad (3.3)$$

Here, B and ρ pertain to the properties of the cyclotron itself, not an ion's magnetic rigidity.

After being emitted from the K1200 cyclotron, the beam is impinged on a ^{9}Be target and undergoes a fragmentation reaction. These production targets are typically hundreds of mg/cm^2 thick. ^{9}Be is used for its very high number density, while being less reactive than lithium. The projectile fragmentation reaction produces a wide mixture of fragmentation products, often including every element with lower Z than the primary beam [64]. These secondary beam components experience kinematic focusing from the peripheral reactions with ^{9}Be, which often strips several nucleons without greatly reducing momentum. This cocktail of potential secondary beams and the much more intense unreacted primary beam are then sent to the A1900 fragment separator.

3.1.3 A1900 Fragment Separator

The A1900 fragment separator is a large acceptance, achromatic, high resolution separator [58]. Four superconducting dipole magnets and 24 superconducting quadrupole magnets separate the secondary beam of interest in three stages. The four dipole magnets bend the beam along 45 degree arcs. Between each of the dipoles, at points labeled "image" in Figure 3.2, the beam has different amounts of horizontal dispersion. The A1900 separates beams according to the magnetic rigidity of the ions ($B\rho = \gamma mv/q$). All secondary beams start with nearly the same velocity as the primary beam due to the kinematics of the fragmentation reaction, so the slits positioned at the second image location select ions along m/q, the

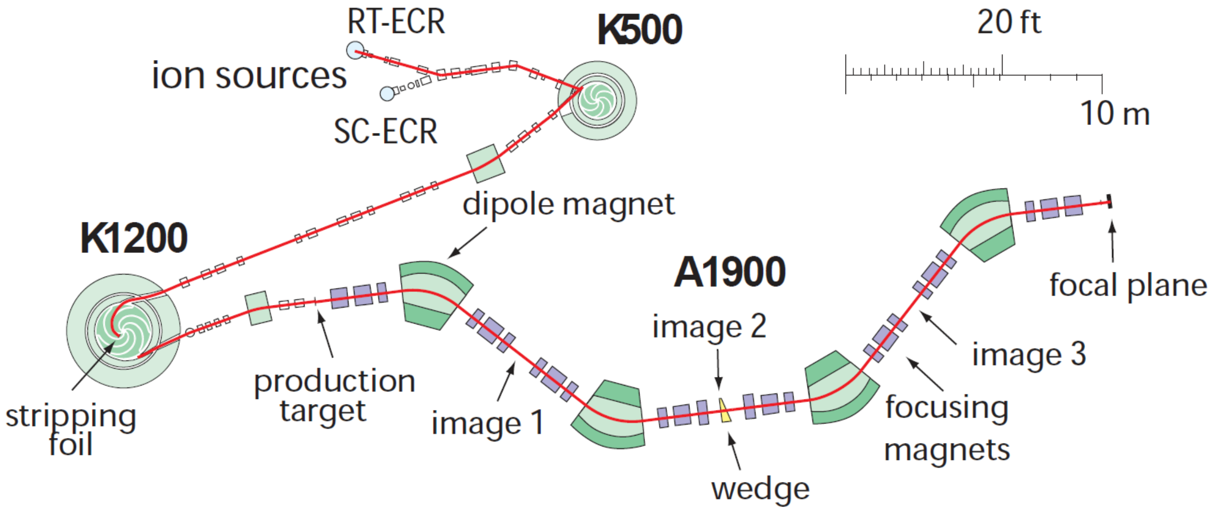

Figure 3.2: A schematic of the NSCL facility, showing the coupled K500 and K1200 cyclotrons and the A1900 fragment separator. The figure was adapted from Ref. [65].

mass to charge ratio. In the second half of the A1900, ions are further separated based on atomic number by first changing their $B\rho$. This is accomplished by placing an achromatic energy degrader (an aluminum "wedge") at the point of maximum horizontal dispersion. The energy loss experienced by the ions in the wedge, per unit of distance, is given by the Bethe-Bloch formula [45]:

$$\frac{dE}{dx} = -\frac{4\pi e^4 n_e Z^2}{m_e \beta^2}\left[\ln\frac{2m_e\gamma^2\beta^2}{I} - \beta^2\right] \tag{3.4}$$

where m_e and e are the mass and charge of the electron, n_e is the electron number density of the wedge, I is the mean excitation potential of the wedge, and Z and β are the atomic number and velocity relative to the speed of light of the incident ion. Since energy loss will differ for different ion atomic numbers Z, ions that previously had similar $B\rho$ no longer will. The last half of the A1900 is a mirror of the first half, selecting along magnetic rigidities $B\rho$ using the superconducting dipole magnets. The ultimate purity of the secondary beam will depend on production of contaminants with similar mass to charge ratios ($B\rho \approx A^{2.5}/Z^{1.5}$) [66] of the beam of interest.

3.1.4 Beam Stopping

In order to utilize reactions that occur near the Coulomb barrier, like fusion-evaporation, outgoing beams from the NSCL must be significantly slowed. First the beam energy is brought down to thermal energies before reacceleration to the desired energy. An alternative approach in which the secondary beam energy is degraded in a single step would produce a beam with very large emittance and energy distribution due to straggling. In this experiment, the beam was stopped in a linear gas cell full of helium, before being extracted using inhomogeneous alternating electric fields and a static electric field [67].

The secondary beam of choice (^{45}K) arrives at the gas stopper, but first passes through several energy degraders. After passing through a window made of beryllium, the rare-isotope beam begins colliding with the helium buffer gas. The chamber itself is 50 cm long and filled with pure helium at a pressure of 1 bar. During the stopping process, beam particles collect electrons, and the charge state is reduced down to 1+ by interaction with the ultra-pure helium. Once thermalized, the ions are guided out of the stopper using a novel "ion surfing" technique [67]. In this mode, a static electric field pushes ions toward a repelling RF "carpet" of electrodes. The ions accumulate in the potential minimum created near the surface of the carpet due to damping from the helium buffer gas. In order to move the ions forward along the longitudinal axis of the gas stopper, phase-shifted high frequency voltages are applied to the electrodes to create a travelling potential wave that the ions can travel on. This scheme is more effective than classical RF transport schemes and ensures

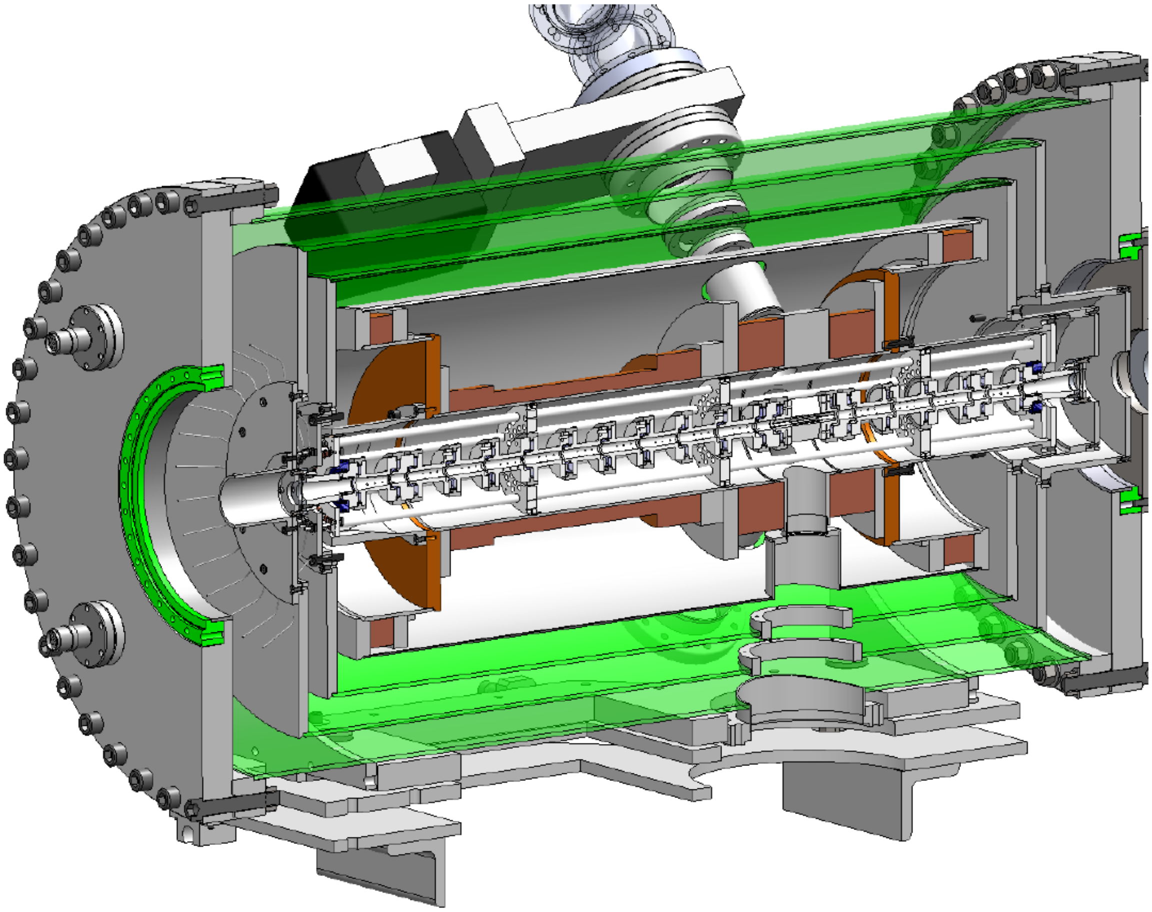

Figure 3.3: Design of the Electron Beam Ion Trap. The figure is from Ref. [60].

fast extraction, key for RI beams with short lifetimes.

3.1.5 The Electron Beam Ion Trap (EBIT)

Before the thermalized ions can be reaccelerated, their charge state must be increased. The Electron Beam Ion Trap at the NSCL [68, 69, 70] is similar to traps used at other post-accelerator facilities [71], but notably is able to operate continuously as the beam is delivered.

The beam exiting the gas stopper arrives with a charge state of 1+. The ions are confined to the trap by two Helmholtz coils and a solenoidal magnet in the radial direction, and 22 small electrodes in the axial direction (see Figure 3.3). An electron gun aimed coaxially further ionizes the beam components, which in turn improves their confinement in the trap. Ions are charge bred up to the desired charge state before the trap opens and allows their exit, moderated to a final beam energy of 12 keV/u. EBIT requires a charge to mass ratio from 0.2 to 0.5 to function. In this work, ^{45}K was charge bred up to 17+ before being injected into ReA3.

3.1.6 Q/A Separator and ReA accelerator

Ions released from EBIT undergo a separation to isolate a single charge state (Figure 3.4). The procedure consists of a 90 degree electrostatic bend and a slit to select along a horizontal energy dispersion, followed by a matching magnetic bend and a slit to select based on momentum dispersion. This ensures a pure beam without contaminants from the stopping and charge breeding processes.

After exiting the Q/A separator, there is a length of beam line known as the Low Energy Beam Transport (LEBT), which primarily contains the 80.5 MHz Multiharmonic Buncher (MHB), which bunches the beam to facilitate the upcoming acceleration stages. The MHB leads to the reaccelerated beam ultimately arriving in bunches to the experimental end station at the same frequency of 80.5 MHz. The possible effects of this bunching were considered with regard to the Segmented Germanium Array's detector response and the data acquisition system. It is possible to run with a trigger condition on the beam; this would reduce detector background and total detection rates. This was not used in this experiment as it was not necessary based on rates that were anticipated.

As seen in Figure 3.5, the acceleration stages of ReA3 begin with a room temperature Radio Frequency Quadrupole (RFQ) structure, which accelerates the beam from the 12

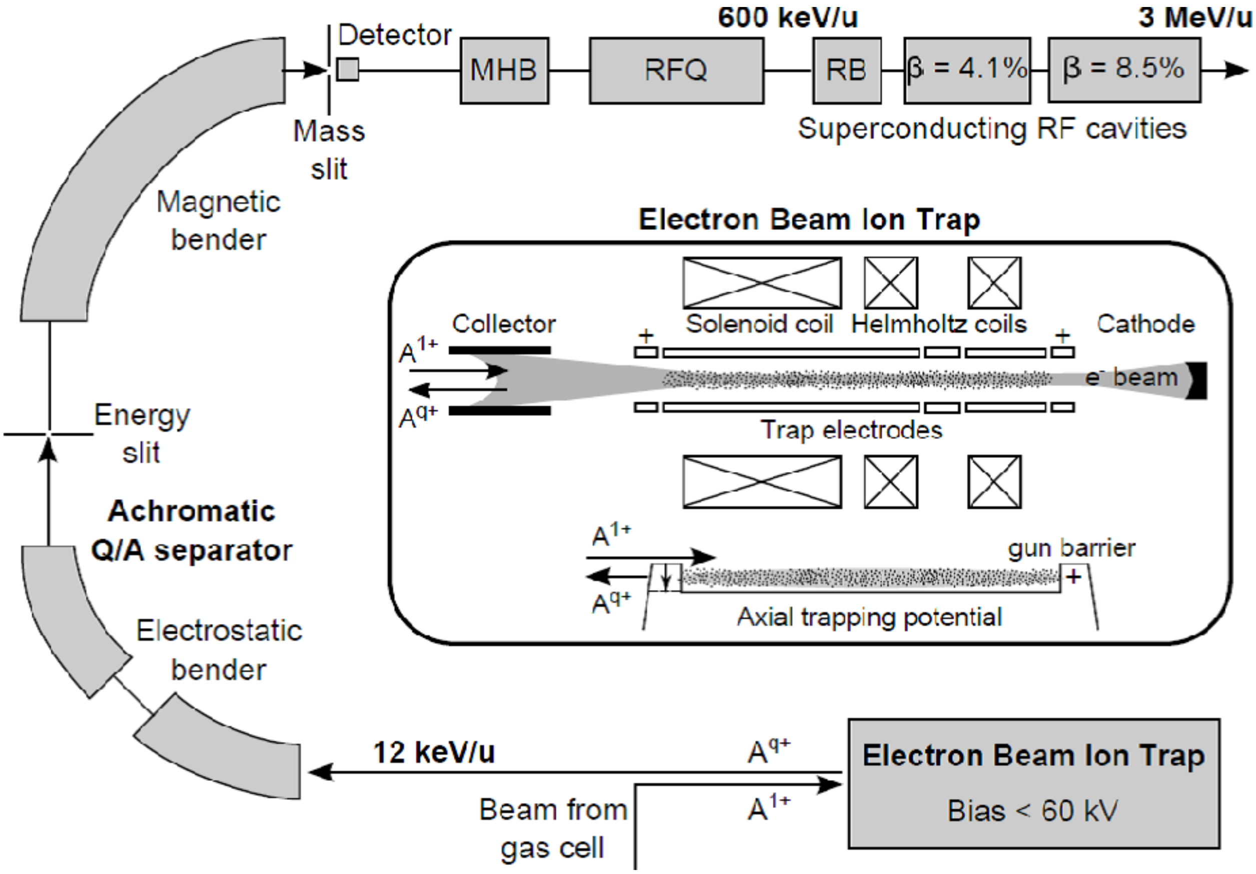

Figure 3.4: Design of ReA3, showing the EBIT, the Q/A separator, the Multiharmonic Buncher, the Radio Requency Quadrupole structure, and lastly the RF cavities. The figure is from Ref. [72].

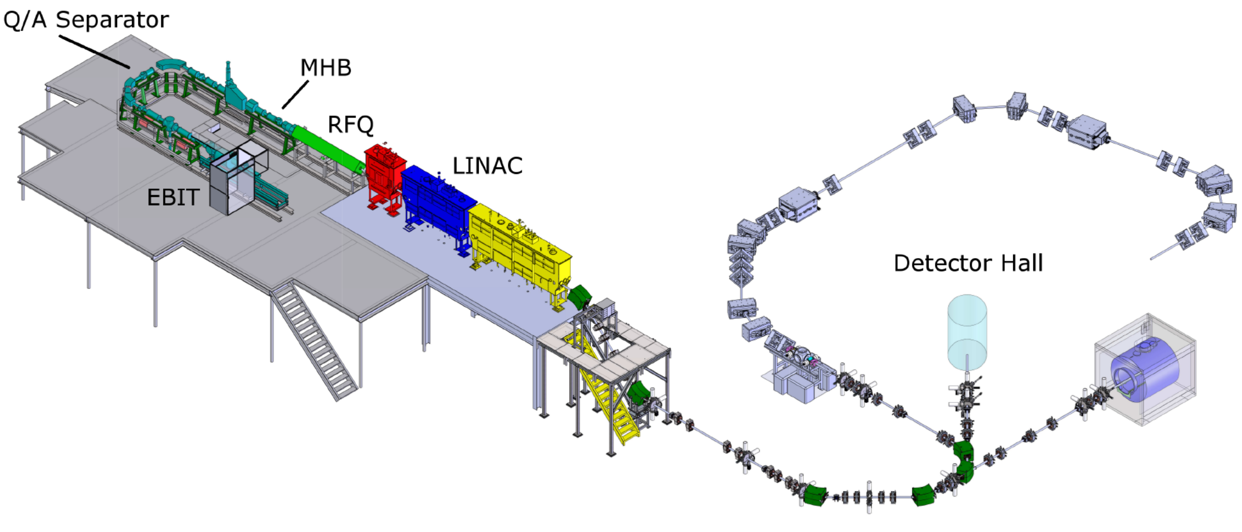

Figure 3.5: Schematic of the full ReA facility, from EBIT to the detector hall where the experimental was performed. The general purpose beam line where the experiment was performed is shown, in between the JENSA (left) and AT-TPC (right) experimental lines.

keV/u kinetic energy out of the EBIT up to 600 keV/u, independent of the chosen beam's Q/A ratio [73]. The beam then reaches the superconducting linear accelerator, comprised of 15 superconducting niobium quarter wave cavities across a set of three cryomodules. The first two cryomodules have their superconducting cavities optimized for a velocity β of 4.1%, whereas the last set is optimized for $\beta = 8.5\%$. This produces a pure, pencil-thin beam bunched at a frequency of 80.5 MHz, and a beam spot of approximately 3 millimeters. The beam energy is dependent on the choice of nuclei, but ^{238}U can be accelerated up to 3 MeV/u, hence the name ReA3. Other beams reach higher energies; for instance in this work, a beam of ^{45}K was accelerated to an energy of 4.66 MeV/u. The beam is transported along the Medium Energy Beam Transport (MEBT) to the detector hall, the location of our experimental end station.

3.1.7 Stable Beam Production and Tuning

In addition to a rare-isotope beam of ^{45}K, a stable pilot beam of ^{40}Ar was produced, without the use of the Coupled Cylotron Facility or the A1900 fragment separator. Instead, ^{40}Ar gas was injected into the EBIT for charge breeding. The Q/A selector was then set up to choose a charge state of 15+ for ^{40}Ar, to roughly match the Q/A ratio of the main beam ^{45}K^{17+}.

To tune the beam, a 3 mm collimator was placed at the target position. Beam currents were measured after this collimator and after a 5 mm aperture upstream of the target, with more than 90% of the beam passing through the target collimator.

3.2 Segmented Germanium Array (SeGA)

The Segmented Germanium Array (SeGA) has proven to be a powerful detection system for gamma-ray spectroscopy experiments at the NSCL [75, 76]. In this work, SeGA consists of 16 high-purity germanium detectors, though up to 18 individual detectors have been used in previous experiments. Each detector contains a germanium crystal, a liquid nitrogen reservoir, and charge-sensitive preamplifiers, as shown in Figure 3.6.

When designing germanium gamma-ray detectors for in-beam experiments, there is a trade-off in the higher efficiency afforded by large-volume detectors against their low angular sensitivity (as well as the increased cost to grow large crystals). By dividing the detector's charge collection into discrete segments, the gamma-ray interaction position within the crystal can be known, which allows for precise Doppler-shift reconstruction of gamma-ray energies. In SeGA, an n-type coaxial germanium crystal measuring 8.0 cm long and 7.0 cm in diameter is electronically segmented into 8 lateral divisions ("slices"), and further divided into 4 quadrants, giving a total of 32 segments per crystal (Figure 3.7). However, this seg-

Figure 3.6: A germanium detector from SeGA. The large green cylinder is the liquid nitrogen reservoir, the preamplifiers are directly below the dewar inside the casing, and the germanium crystal itself is the inside the cylinder at the bottom of the image. The figure is from Ref. [74].

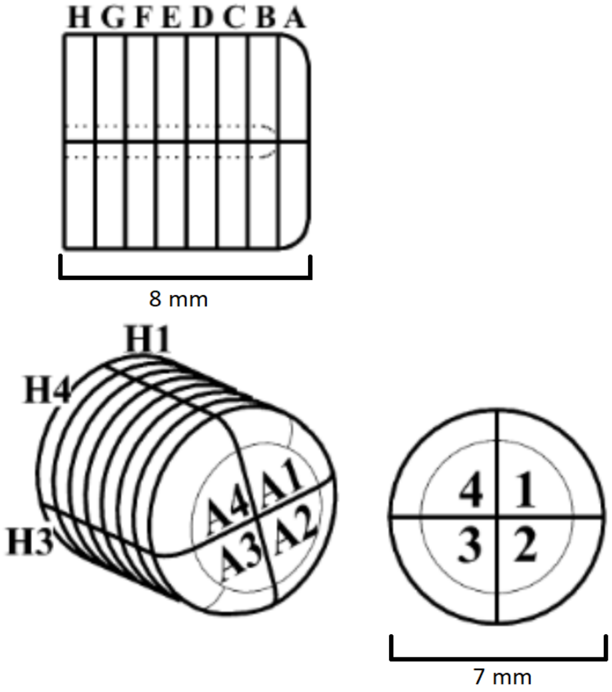

Figure 3.7: Diagrams of the crystals in SeGA. Lateral divisions and quadrants are labeled with letters and numbers, respectively. The interior of the coaxial detector is shown with a dotted line. The figure is from Ref. [75].

mentation is only present on the exterior of the crystal. The central contact of the bulletized closed-end crystal is connected to a single internal electrode biased to an operating voltage of about 4000 V. Each of the external 32 segments is connected to ground, leading to the potential difference that causes electrons to collect along the central contact and holes to collect on the segments.

As explained in the section 2.2.1, for significantly energetic gamma rays in the range of several hundred keV or more, it is unlikely that all of the energy is deposited directly within a single segment of the crystal. With this in mind, event construction with SeGA uses the central contact energy to determine the total energy deposited, while segment hits are used to determine the interaction position. This determination impacts the calculated emission angle of the gamma ray after the reaction in the target, and thus the Doppler correction. In this analysis, the first interaction position of the gamma ray is assumed to be the segment with the largest energy deposition. This has been shown to be an effective choice for interaction position in similar detectors [77], as opposed to a more complicated tracking algorithm which would require a much higher angular sensitivity. Sub-segment position resolution is possible using SeGA by recording and analyzing the waveforms of the segment input signals [78]. This entails an algorithm measuring pulse shape of the central contact signal to determine radial position and transient signals from neighboring segments to determine lateral and azimuthal positions. In this experiment, the geometric center of the segment was a sufficient determination of interaction position for successful Doppler-correction of gamma-ray energies.

As discussed previously, germanium's small band gap of $E_g = 0.67$ eV compared to silicon's 1.14 eV causes a significant leakage current at room temperatures from random thermal excitations. To minimize the leakage current, the germanium detectors in SeGA are cooled to a temperature of 100 K using individual liquid nitrogen reservoirs contained in 2 liter dewars. The germanium is kept in thermal contact with the liquid nitrogen, which is replenished by an automated filling system during operation. In fact, SeGA detectors are kept in this cooled state whether they are currently in operation or not, because allowing the detectors to repeatedly warm and cool causes their vacuum seal to degrade over time.

The SeGA detectors can be arranged in several different configurations that allow for improved efficiency or angular resolution, as needed by the experiment. With unsegmented detectors of a cylindrical shape, detectors are typically arranged with the circular face pointed directly at the reaction or decay position; this is to minimize the angular resolution, which relates to the size of the entire detector. However, with the segmentation of SeGA, a much larger solid angle coverage can be achieved by a side-on configuration. In this experiment, the compact "barrel" configuration was chosen to maximize the possible solid angle subtended by the detectors. As shown in Figure 3.8, this configuration places 16 detectors parallel to the beam axis in a forward and backward ring of 8 detectors each.

Each SeGA detector had a total of 33 signals to read out during the experiment: 32 for each segment cathode contact and 1 for the central anode contact. These signals were preamplified with on-board charge-sensitive preamplifiers. Having preamplifiers incorporated into the detector itself minimizes stray input capacitance. The preamplified signals were then sent to XIA 100 MHz PIXIE-16 FPGA modules to be digitized and ultimately read out to the NSCLDAQ data acquisition system, as discussed in Section 3.4.

3.2.1 Calibration

Energy calibrations of SeGA are typically performed by placing a standard gamma-ray source at the target position before or after an experiment, and comparing the measured signal

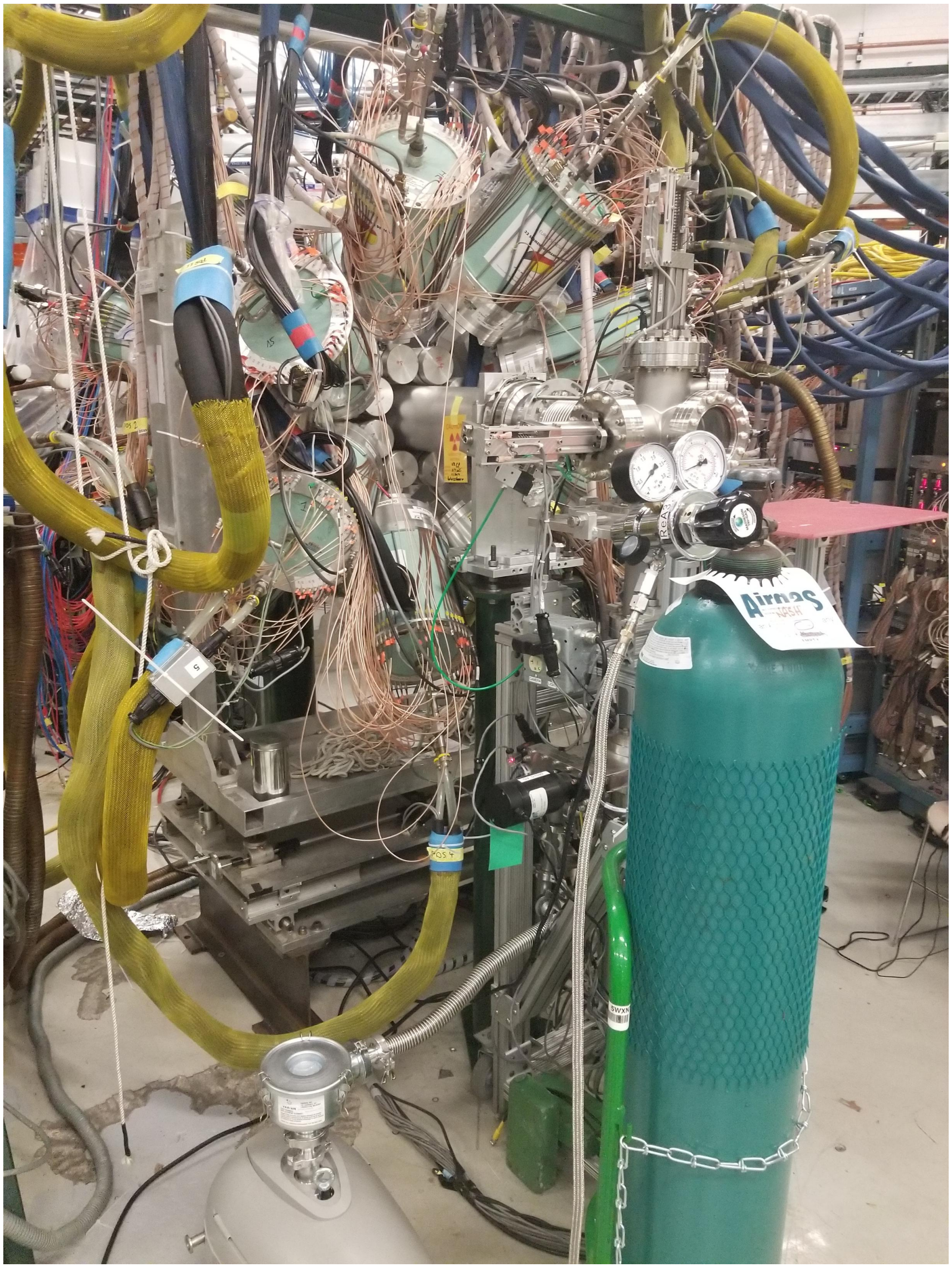

Figure 3.8: The downstream side of the full SeGA array, arranged in the compact barrel configuration around the beam line at the ReA3 end station. Eight detectors are present on this side, constituting the array's forward ring, with a matching set of eight detectors on the upstream side.

amplitude to the well-known gamma-ray energies, thus providing a basis for measuring new gamma-ray transition energies. This procedure was indeed performed in this experiment, with a ^{226}Ra source before the experiment and ^{152}Eu and ^{60}Co sources afterward. These calibrations were used to correct gamma-ray energies for the results of the ^{40}Ar pilot beam, specifically the central contact energies which represent the total energy deposited in the detector. The segment energies were left with a relatively rough calibration based on previous measurements, which was acceptable given their primary use for position information rather than energy information. The resulting calibration is satisfactory for the data resulting from the argon beam, with a laboratory-frame 1 MeV gamma ray having a full-width-at-half-maximum (FWHM) of about 4 keV when summed over all 16 detectors. However, this calibration had the potential to be greatly improved for the important ^{45}K-beam data by introducing time-dependent corrections.

Using gamma-rays from the beta decay of the ^{45}K RI beam allowed for a much improved SeGA energy calibration, with an energy resolution of 2.7 keV for a 1 MeV gamma ray when summed over all 16 detectors. These background gamma rays produced from the unreacted beam dominated SeGA's gamma-ray singles spectra, as seen in Figure 3.9. A total of twelve gamma-ray transitions were chosen from the deexcitation ^{45}Ca that had well-known energies and spanned nearly the full range of SeGA's detector response, from 170 to 3300 keV. By detecting changes in these peak energies over the course of the experiment, time-dependent corrections could be made to the calibration of SeGA's detectors, which improved energy resolution of the array and fixed instabilities observed in two specific detector signals.

In one case, a detector in the downstream ring of SeGA experienced a slow drift in gamma ray energy throughout the experiment (Figure 3.10). This linear drift over 10-15 keV was corrected by including separate calibration parameters for each run during the ^{45}K-

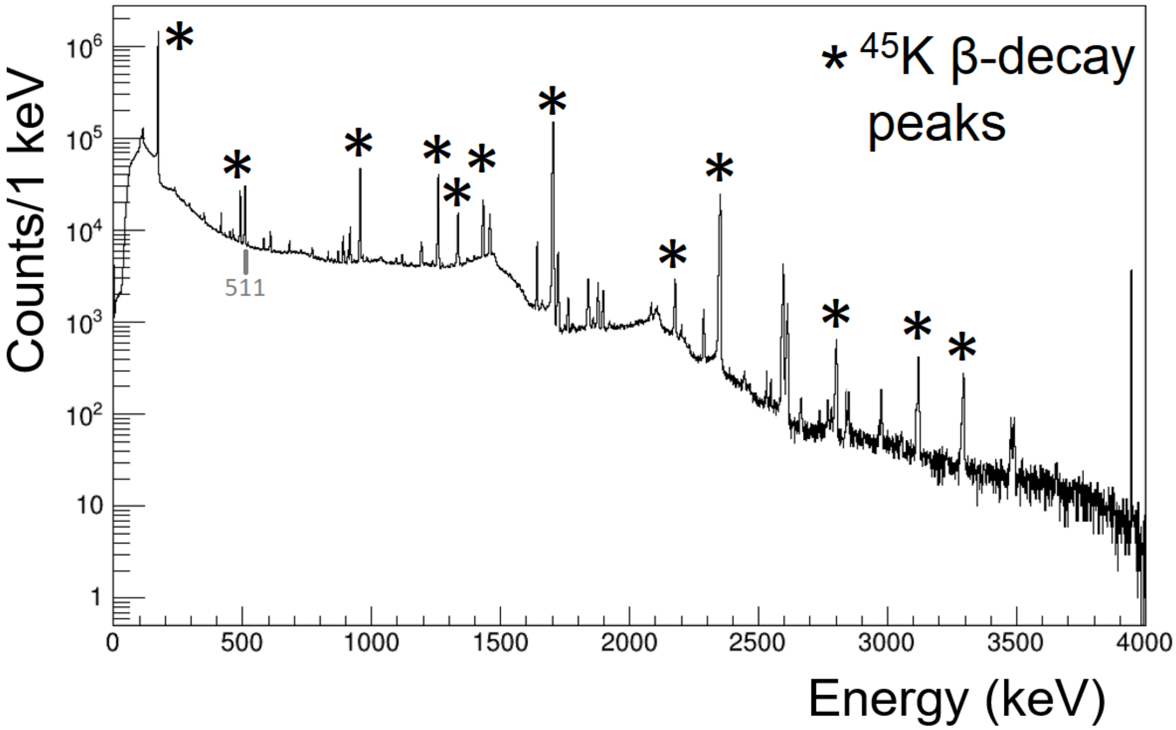

Figure 3.9: Laboratory frame gamma-ray singles spectra from SeGA with ^{45}K RI beam. Spectrum is dominated by beta-decay gamma rays from ^{45}Ca deexcitation. Twelve of these peaks, which have very well-known energies, were used for time dependent corrections to the energy calibration, and are labelled with an asterisk.

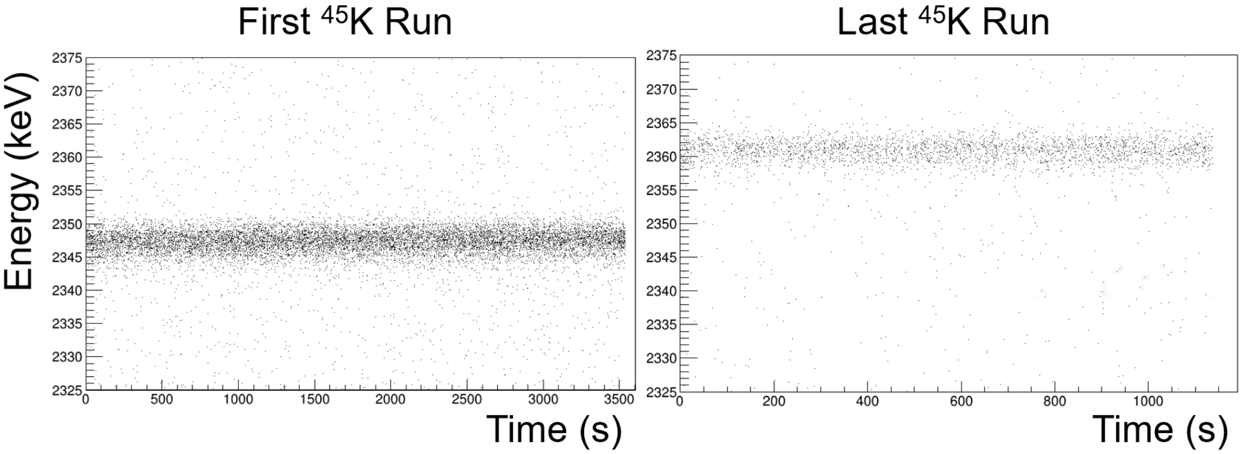

Figure 3.10: Plots of gamma-ray energy vs time elapsed in a given run, showing a ^{45}K beta-decay energy experiencing a slow drift of 14 keV over the course of the experiment. This behavior was observed for one detector, and was fixed with run-by-run corrections to the energy calibration.

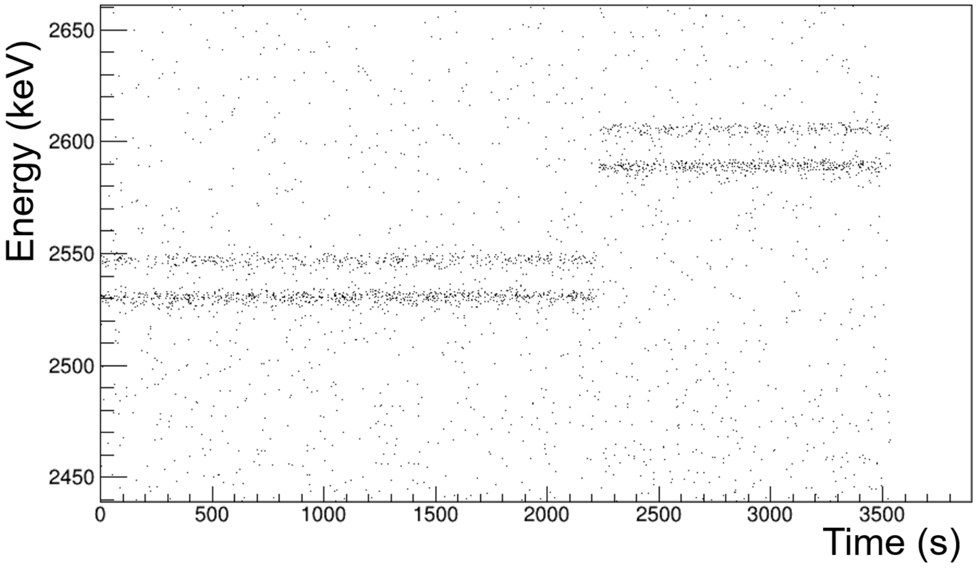

Figure 3.11: Plots of gamma-ray energy vs time elapsed in a single run, showing two ^{45}K beta-decay peaks experiencing a sudden shift of 50 keV. This behavior was observed for one detector, and had to be corrected with sub-run time dependence to the energy calibration. The cause of this behavior has since been attributed to one of the channels in the data acquisition system.

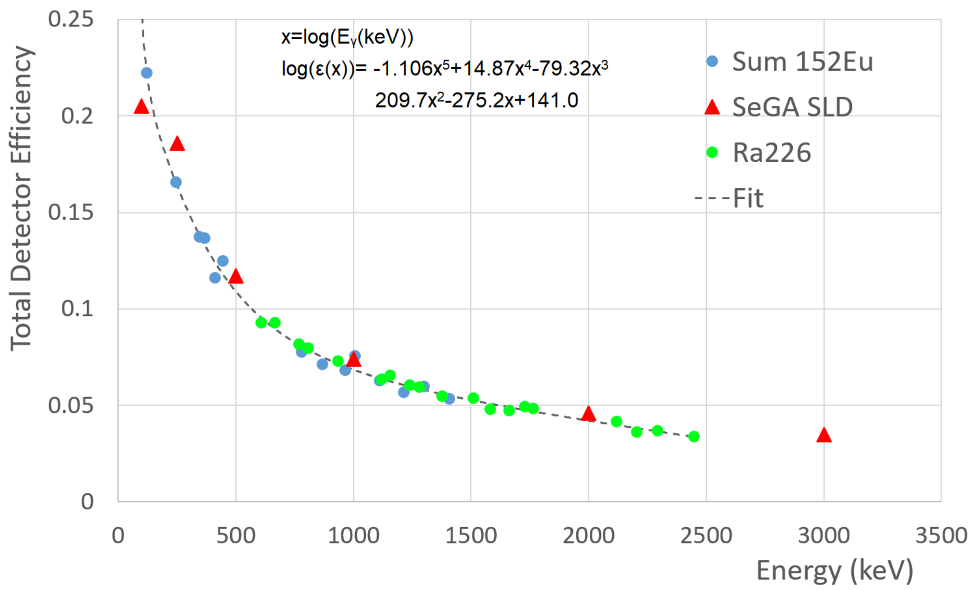

Figure 3.12: Gamma-ray detection efficiency of SeGA determined from ^{152}Eu and ^{226}Ra sources, compared to SeGA's Service Level Description. The data from the ^{226}Ra source was scaled relative to the data from the ^{152}Eu source, which had a more precisely known activity. Data was fit using a polynomial curve in log-scale, similar to the procedure in Ref. [79].

beam data. For a second detector, in the upstream ring of SeGA, sudden instability caused virtually instant shifts in gamma-ray energy of 50 keV were observed (Figure 3.11). Both of these instabilities could have occurred due to thermal effects, noise in the detector and preamplifier signals, or other potential causes. It should be noted that this effect has been observed previously, including with different data acquisition systems [79]. Nevertheless, time dependent corrections that tracked sudden shifts in energy and corrected them allowed the detector's response to be used in the analysis. Calibration parameters were the result of a linear fit from observed peak channels and true gamma-ray energies; quadratic fits were performed as well and deemed unnecessary.

Efficiency calibration for SeGA provided an essential means of extracting absolute cross sections during this experiment. In addition, understanding the photopeak efficiency of SeGA's experimental setup is important when verifying any simulation performed during analysis by assuring that the geometry and gamma-ray interaction and attenuation is being modeled properly. There are several factors that contribute to a detector's observed efficiency, including the intrinsic germanium efficiency (which is dependent on gamma-ray energy) and solid angle coverage. Additional materials present in the experimental setup can impact photopeak efficiency, for example the aluminum frame and casings of SeGA, the beam pipe, and the materials holding the target and charged particle detector.

Photopeak efficiency for SeGA was determined with the same ^{152}Eu and ^{226}Ra source measurements mentioned previously. The ^{152}Eu source produced gamma-ray peaks whose intensities were compared to the source's precicely known activity. To extend the range of gamma-ray energies covered by the calibration up to 2.5 MeV, a ^{226}Ra source was used, and the resulting gamma-ray yields were scaled to the previous ^{152}Eu result. Figure 3.12 shows the total photopeak efficiency for SeGA as a function of gamma-ray energy. Also shown is the nominal values from the Service Level Description of SeGA [80] for the barrel arrangement used in this work. SeGA's efficiency was further characterized by a logarithmic fit, which was subsequently used to calculate gamma-ray yields.

3.3 Charged Particle Detection

This work utilized a segmented double-sided silicon detector to measure charged particles emitted from reactions occurring in the target, and thus partially select reaction channels when in coincidence with gamma rays. The chosen detector was an annular S3-type detector manufactured by Micron Technology, Inc. The dimensions of the active volume of the detector were an inner radius of 1.1 cm, and outer radius of 3.5 cm, and a thickness of 0.1 cm. This is a thicker detector than the one used in JANUS experiments [59], which deal with

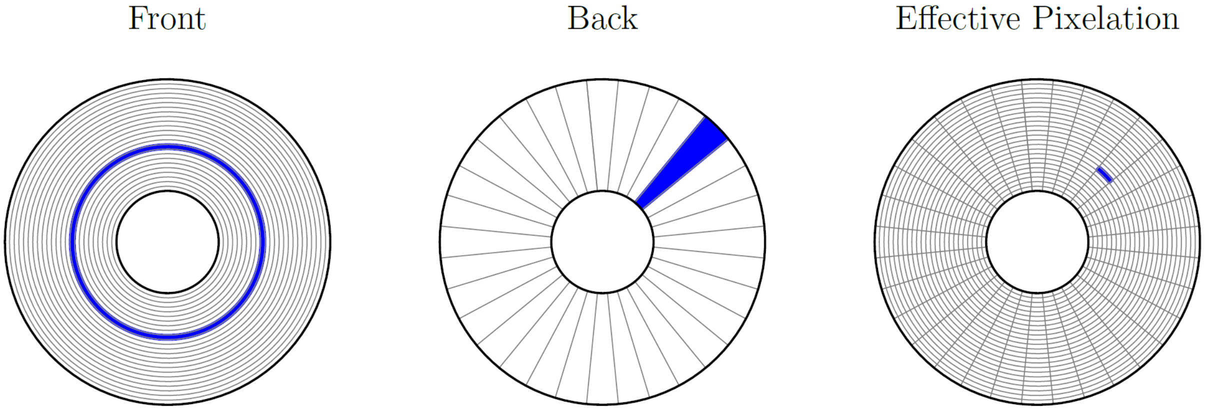

Figure 3.13: Segmentation of S3-type annular silicon detectors. Energy deposited in the ring and sector shaded in blue will lead to the position resolution shown.

scattered heavy particles that have a much shorter range in silicon than the lighter particles observed in this experiment. The detector was placed perpendicular to the incoming beam and 3.1 cm downstream of the target, subtending polar angles from 20 to 50 degrees relative to the beam axis. This distance was chosen to optimize yield for alpha particles recoiling from compound reactions in the target anticipated from PACE4 calculations, as described in section 3.5.2.

The silicon detector's segmentation (Figure 3.13), allows for knowledge of the incoming charged particle's trajectory. On the upstream side of the detector, the surface is segmented radially into 24 rings, each 0.1 cm thick. On the reverse side, 32-fold azimuthal segmentation divides the detector into sectors, each covering 11.25 degrees in ϕ. After applying a voltage to the detector, charge will collect on both sides and generate two signals. These signals can be paired to determine a pixel of interaction for the charged particle. By collecting and analyzing 56 signals, $24 \times 32 = 768$ pixels provide the position resolution for the detector.

To prevent a leakage current from creating noise in the signals, a bias voltage of 70 V was

Figure 3.14: The upstream side of the experimental end station, showing the backward ring of SeGA and the silicon preamplifiers. Aluminum foil was used to provide shielding for the detector signals.

applied across the detector. When applying the bias, the voltage was steadily increased until the measured leakage current leveled off, indicating that the entire volume was depleted. This ensures a very high efficiency in charge collection throughout most of the detector volume, other than a small dead layer near the detector surface. Signals from the silicon detector were read-out to nearby preamplifiers, as shown in Figure 3.14.

As with SeGA, the silicon charged-particle detector needs calibration before the detector signals can be related to energy deposition. This was accomplished by placing a source of alpha particles 3.1 cm from the silicon detector and comparing the detector response to the known energies of the source. In this case, a source consisting of three nuclei, ^{239}Pu, ^{241}Am, and ^{244}Cm, emitted alpha particles at energies of 5.15, 5.48, and 5.80 MeV. This produced Figure 3.15, which shows that the 3-alpha source was placed about a centimeter from the center of the detector.

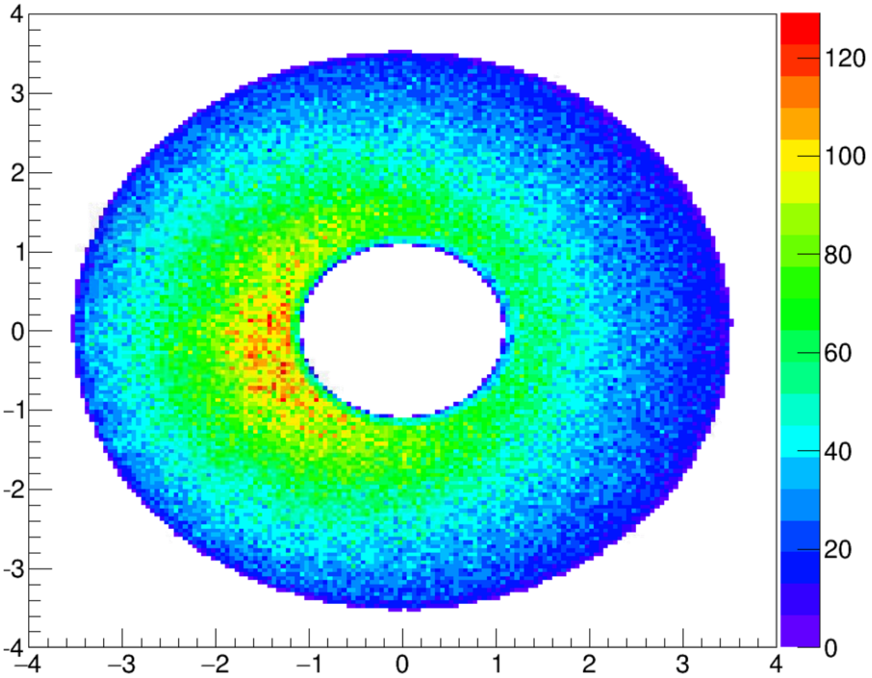

Figure 3.15: The hit pattern for the silicon detector when exposed to a 3-alpha source. The vertical and horizontal axes are height and width in cm, and the color is the number of counts in each pixel. Events are positioned randomly within an individual pixel for visual effect.

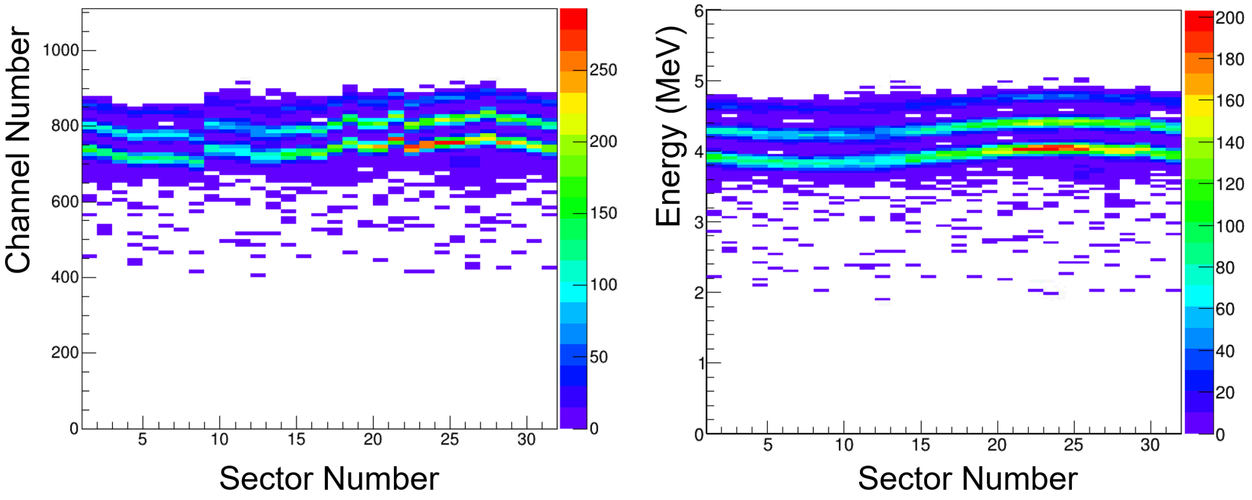

Figure 3.16: An example of the silicon detector response to a 3-alpha source for a single ring channel. Events across the entire ring would appear as poorly resolved (i.e., if projected onto the y-axis), but when presented with correlated hits in each of the 32 sector channels, a clear sinusoidal pattern emerges, related to the change of the angle of incidence and thus the energy loss due to dead layer. On the left is the uncalibrated signal, and on the right is the calibrated result. Note the significant energy loss of roughly 1 MeV from the known alpha particle energies of 5.15, 5.48, and 5.80 MeV. This energy loss varies along different rings and is higher for larger θ with respect to the beam axis.

In an ideal silicon detector, all signals would contain three peaks corresponding to the three known alpha energies, which could then be fitted linearly to calibrate the silicon detector. However, due to a significant dead layer at the surface of the detector, the amount of charge collected depends on the angle of the incoming particle (Figure 3.16). To account for this effect, gain matching was performed with an effective dead layer thickness as a variable to be optimized. The effective dead layer thickness and a range table for alpha particles in silicon were used to calculate energy loss due to dead layer (see Equation 2.2), and the resulting adjusted alpha particle energy was compared to the observed channel number for the 3-alpha peaks. The precise location of the source itself was also allowed to vary. Through an iterative procedure based on correlated hits in the ring and sector segment signals, an effective dead layer of 8 microns was determined to best explain the dependence on incident alpha angle.

3.4 Data Acquisition

Preamplified signals from SeGA and the silicon detector were processed using an all-digital acquisition system. The Digital Data Acquisition System (DDAS) [81] and the NSCLDAQ framework were used to digitize and readout data in this experiment. Digital electronics like the XIA PIXIE-16 FPGA modules used here replace traditional analog electronics; one digitizer module can perform the roles of a shaper, discriminator, analog-to-digital converter (ADC), and time-to-digital converter (TDC). DDAS has advantages over the older systems that include higher energy resolution, lower energy thresholds, and lower dead-time [82]. The potential for higher energy resolution is created by improved Doppler-corrections from sub-segment position resolution, which is accomplished by recording the waveforms of SeGA's

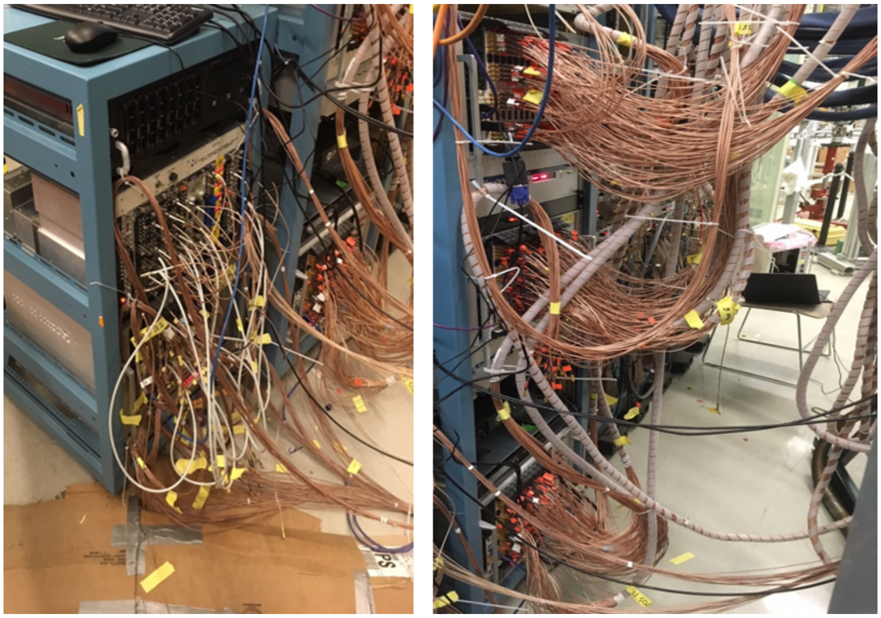

Figure 3.17: DDAS as it was used in this experiment. On the left is the XIA mainframe for the silicon detector, and on the right are the mainframes for SeGA. The figure is from Ref. [83]

segment information. As mentioned earlier, this was not necessary for this work.

The number of SeGA and silicon signals determined the number of PIXIE-16 modules that were necessary. Each of SeGA's 16 detectors read out 33 signals, including the single central contact and 32 segment pulses. After adding the silicon detector's 24 ring and 32 sector signals, a total of 584 signals (528 for SeGA and 56 for silicon) needed to be digitized. Each PIXIE-16 can digitize 16 signals, so a total of 37 modules were necessary. These modules were stored in 4 separate XIA mainframes, 3 for SeGA and 1 for the silicon detector (see Figure 3.17). In order for the recorded timestamps to correlate across mainframes, a global synchronization pulse is distributed from a designated director module to the others via a custom FPGA module.

There are a total of 39 100 MHz 16-bit PIXIE-16 modules available for SeGA's DDAS to allow for up to 18 detectors, which would be sufficient for the purpose of this experiment.

However, the JANUS experiments that were performed before and after this work required more than 39 modules due to the second silicon detector. Extra 250 MHz PIXIE-16 modules were used for the JANUS silicon detectors, and so were also used in this work. Either frequency was acceptable, and the discrepancy was easily addressed with a conversion of the 16-bit timestamps offline.

Each PIXIE-16 module has FPGAs that process signals and facilitate communication between director and assistant modules within an XIA mainframe. One important aspect of this processing is that the fast trapezoidal filter algorithms must be configured by the user to respond to gamma-rays of interest. DDAS employs two such algorithms: the first generates a trigger on a leading-edge threshold, and the second utilizes a constant fraction discriminator (CFD) algorithm that operates on the response of the trigger filter. For this experiment the second filter was not used, so timestamps were determined by setting a user-specified leading-edge threshold. This means that a significant amplitude walk occurs for gamma-ray events of different energies, but as shown in Section 4.1 this is addressed in the offline analysis. Rise and gap times for the trapezoidal filter were set for based on observed noise from leakage currents.

The operation of DDAS described in this section is referred to as triggerless. This is possible in part due to the low rates observed in typical ReA experiments, as well as the lower dead time of the digital system. Since rates are expected to increase in the future, it should be noted that DDAS has the means to accept constructed coincidence triggers and validation signals to reduce the necessary bandwidth. In this work, running without any triggers beyond each channel's individual trigger allowed for the ^{45}K beta-decay background gamma rays to be measured simultaneously during machine time, which was useful to monitor the gain and improve the energy calibration, as explained previously.

The four XIA mainframes used in this experiment were independent data acquisition systems, in the sense that their data is written to four separate computers. The NSCLDAQ framework is designed to accept multiple sources of data and merge them into a single output data stream. This final data stream was written to disk by the NSCLDAQ. NSCLDAQ also handled the starting and stopping signals sent to the XIA mainframes when a run began and ended, which prevented the systems from becoming out of synchronization.

3.5 Experimental Setup

Figure 3.18 shows a diagram of the setup prepared at the end of the ReA3 beamline. The target location is important to know for the sake of the measurement for proper Doppler correction of gamma-ray energies and extracting cross sections. The lithium target was placed 3.1 cm upstream from the silicon detector. The resultant target position corresponds to 3.7 cm upstream of the center of the SeGA array.

This section will discuss the considerations and preparation that went into making use of a self-supporting lithium target as well as the S3-type silicon detector.

3.5.1 Target Details

The beams from this experiment impinged on a 5.8 mg/cm^2-thick natural lithium target. There were several limiting factors related to target thickness that were key to realizing the present measurement.

First, maximizing the yield of reaction products necessitated a relatively thick target. The listed beam intensity for ^{45}K at ReA3 is 9.8×10^4 pps. This is many orders of magnitude lower than stable beam intensities typically used for gamma spectroscopy studies of

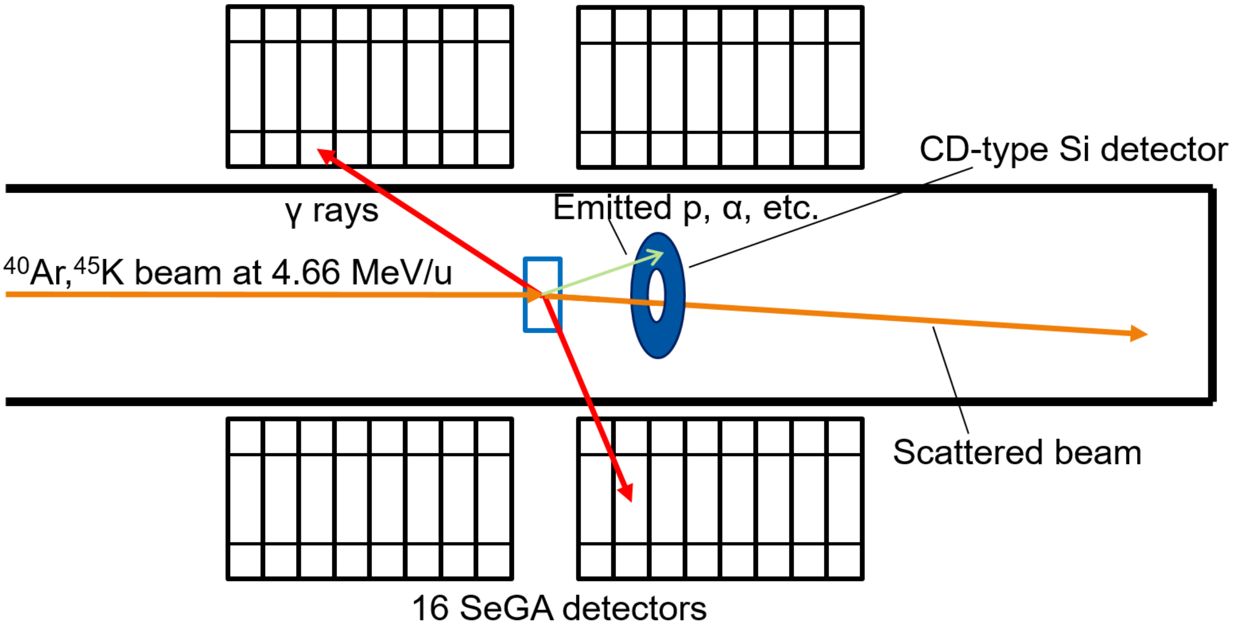

Figure 3.18: Diagram of the experimental setup. SeGA detectors are arranged compactly in forward and backward rings around the beampipe, and detect gamma rays. The silicon detector is placed downstream of the lithium target to select events involving charged particle emission. Unreacted and scattered beam travels through the setup to the beamstop downstream, while the reactions products mostly stop in the target.

reaction products produced at Coulomb barrier energies. Therefore, unlike studies of similar reactions with stable beams, yield is a major concern for this experiment. For this reason, a target thickness was desired that could cover a large range of beam energies, from the initial 4.46 MeV/u down to a lower bound at which reactions populating states of interest would no longer be energetically allowed. The Bass interaction barrier [84] is a useful limit for interaction of two nuclei. For the ^{45}K+^{7}Li system important for this work, the interaction barrier is 8.5 MeV, or 1.4 MeV/u after accounting for the conversion to the laboratory frame energy. Based on the energy loss of ^{45}K in ^{7}Li from range tables, this corresponds to a target thickness of 6.8 mg/cm^{2}. A target with a greater thickness would not be expected to increase yield for the nuclear reactions relevant for the results of this experiment.

Second, a sufficiently thick target can assure that reaction products of interest stop in the target, while unreacted beam particles pass through the target and travel downstream before undergoing beta decay. The compound reactions studied in this work tend to create reaction products at lower energies than more direct, peripheral reactions. This energy dissipation allows compound reaction products to remain in the target and emit gamma rays without a Doppler shift. These gamma rays would have to be emitted several picoseconds after the formation of the reaction product, since it typically takes roughly 1 ps for the recoiling nuclei come to a stop. Therefore isomeric states with long lifetimes and any subsequent decays would be expected to be observed as distinct peak structures in SeGA's energy spectra without Doppler broadening. Meanwhile, unreacted beam produced significant gamma-ray background, as seen in Figure 3.9. It was important that the ^{45}K beta decay to ^{45}Ca downstream of the target in order to not exceed maximum rate limit in SeGA's detectors (3 kHz of events above 100 keV). The data acquisition was also a potential limiting factor, and so rates were monitored throughout the experiment to not exceed 10 kHz across all channels.

Lastly, the target thickness was related to the problem of scattered lithium nuclei recoiling out of the target and potentially dominating the readings from the silicon detector. The elastic scattering cross section for the angles subtended by the silicon detector is expected to increase at lower energies near the interaction barrier, compared to scattering at the initial 4.66 MeV/u. The scattered lithium ions would not be distinguishable from alpha events in the silicon detector, and could have confounded the ability of the detector to effectively select compound reaction events. To address this, a 25-μm film of conductive mylar was installed (Figure 3.19), which had enough stopping power to eliminate virtually all of the lithium ions recoiling from the target, but not enough to hinder a significant number of protons or alpha particles emitted during lithium-induced reactions, due to their higher average energy and lower Z. Both scattered beam and beam-like reaction products experienced forward focusing, within 6 degrees relative to the beam axis and beyond the range of the silicon detector. This created the added benefit of simplifying the Doppler-shift correction for the decay of short-lived states to be made assuming that they were emitted by recoiling nuclei traveling along the beam axis.

When preparing the lithium target for the experiment, care had to be taken due to lithium being highly reactive in air. When exposed to air, lithium will visibly tarnish after only a few minutes, turning from silver to black as it reacts with atmospheric nitrogen to form lithium nitride. It will also form lithium oxide, which is white in color, over a longer period of time. To minimize exposure to air, the lithium targets used in the experiment were prepared in a glove box containing argon gas (Figure 3.20). The lithium arrived in an evacuated glass ampule, which was cut open inside the glove box. Target preparation was done entirely within the glove box, until the target was ready to be installed at its location in Figure 3.19 and immediately inserted into the beampipe and kept in vacuum.

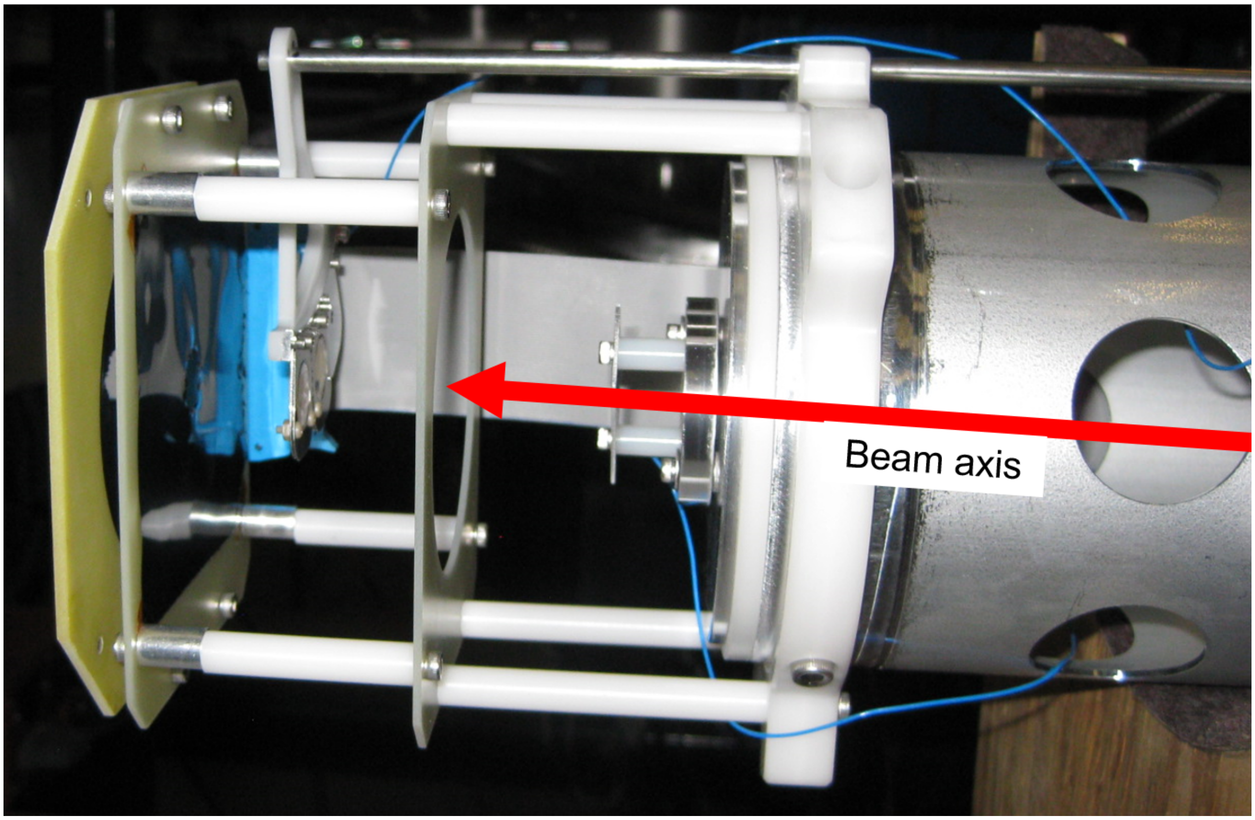

Figure 3.19: Target location for the experiment. Multiple targets and a 3 mm collimator were affixed to a triangular frame which could be rotated from outside the beampipe, facilitating a potential change of target without having to lose and regain vacuum. The silicon detector is visible on the left, with the black conductive mylar in front of it, which was used to shield the detector from recoiling lithium ions.

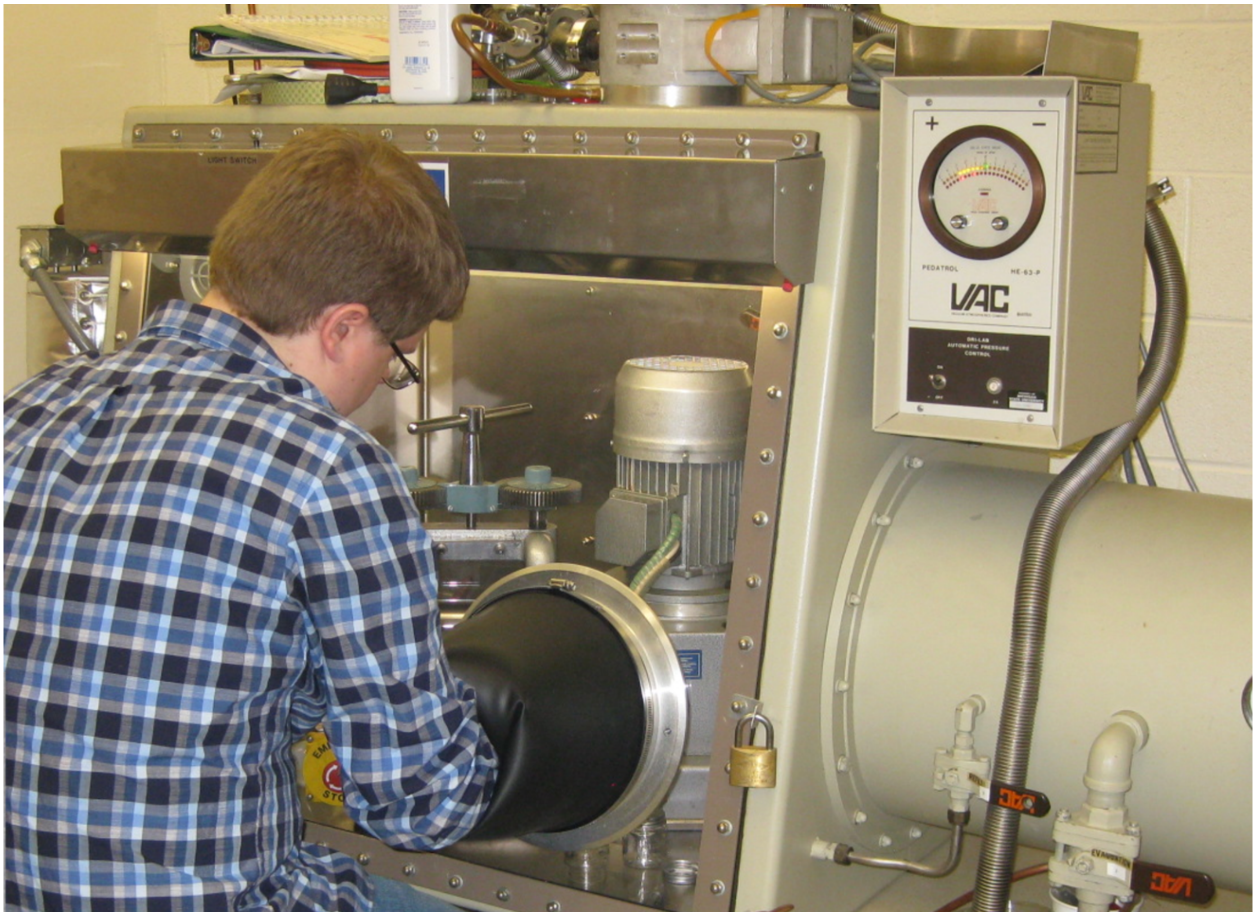

Figure 3.20: Preparation of the lithium target in a glove box filled with Argon.

Several lithium foils were cut and measured. The targets were transferred for weighing using airtight mason jars, and their thicknesses were calculated. To achieve the desired thickness, foils were rolled using a metal roller contained within the glove box, seen in Figure 3.21. When rolling foils, it was important to use a polypropylene foil in between the lithium and the metal to prevent the foil from sticking and becoming too brittle. Ultimately, three target foils were installed along with the 3 mm collimator, with thicknesses of 5.8, 6.1, and 6.5 mg/cm^2. The 5.8 mg/cm^2 target was chosen and used for the full experiment. Results were monitored using online analysis, including signs of nitrogen or oxygen contamination originating from the short period when the target was exposed to air, but there was no indication of contamination for the 5.8 mg/cm^2 target, and there was no need to make use of the alternates.

3.5.2 Expected Silicon Detector Response from Lithium-Induced Reactions

Prior to the experiment, considerations regarding the use of the S3-type silicon detector were made in order to maximize yield in reaction channels of interest. In order to predict cross sections for the lithium-induced reaction channels, the fusion-evaporation code PACE4 [85] was used. This code uses statistical models to predict cross sections for complete fusion reactions as well as angular and energy information for the reaction products. The reaction channels predicted by PACE4 are shown in Figure 3.22, for both the ^{40}Ar stable beam and the ^{45}K RI beam. The predicted excitation functions for reaction channels with significant cross sections can be found in Figure 3.23. Because of the thick target, a single calculation for a given beam energy would not be representative of the expected average cross section. As the

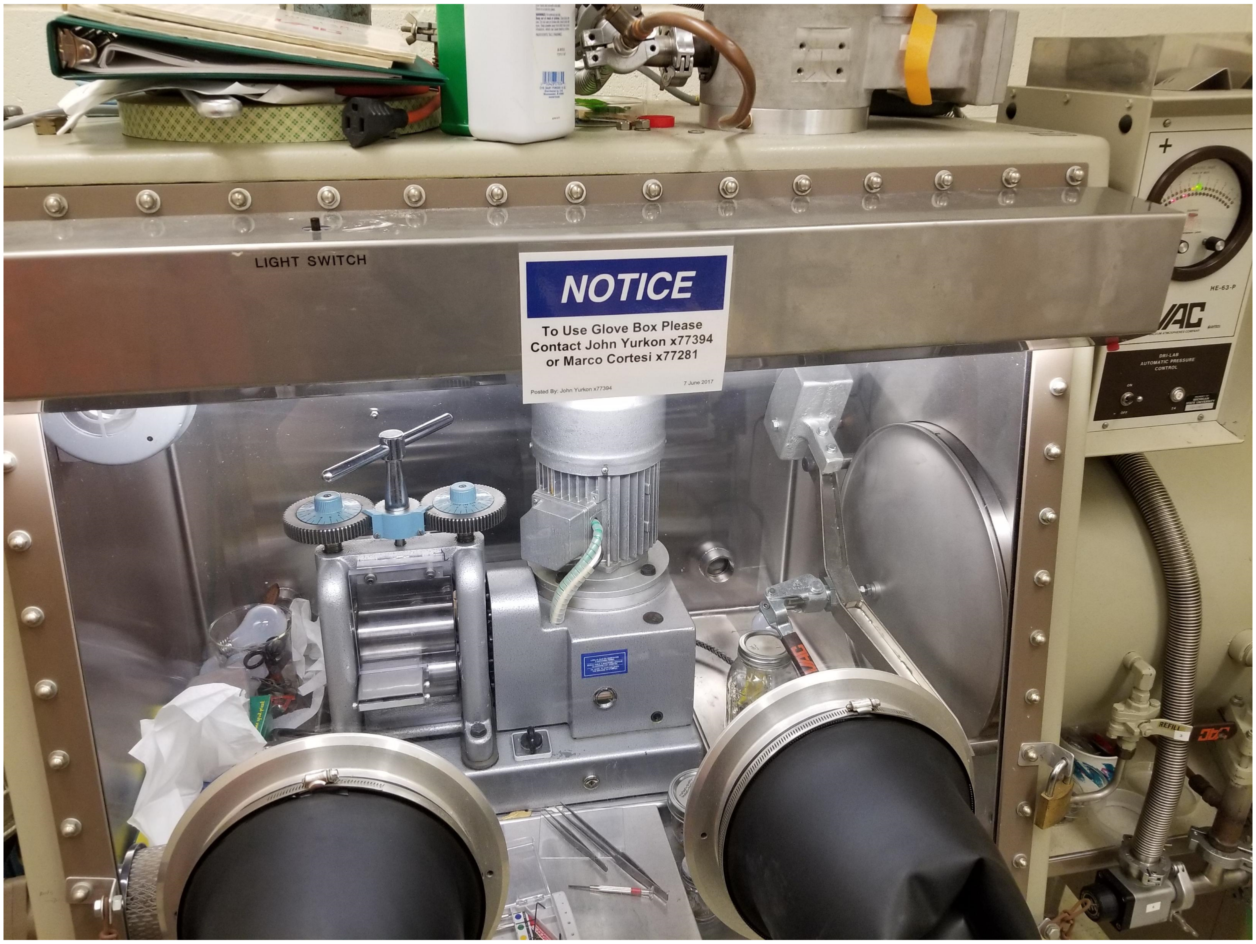

Figure 3.21: Interior of glove box used for lithium target preparation. Mason jars used for the transfer of materials are visible, as well as the metal roller used to achieve the desired thickness of the self-supporting lithium.

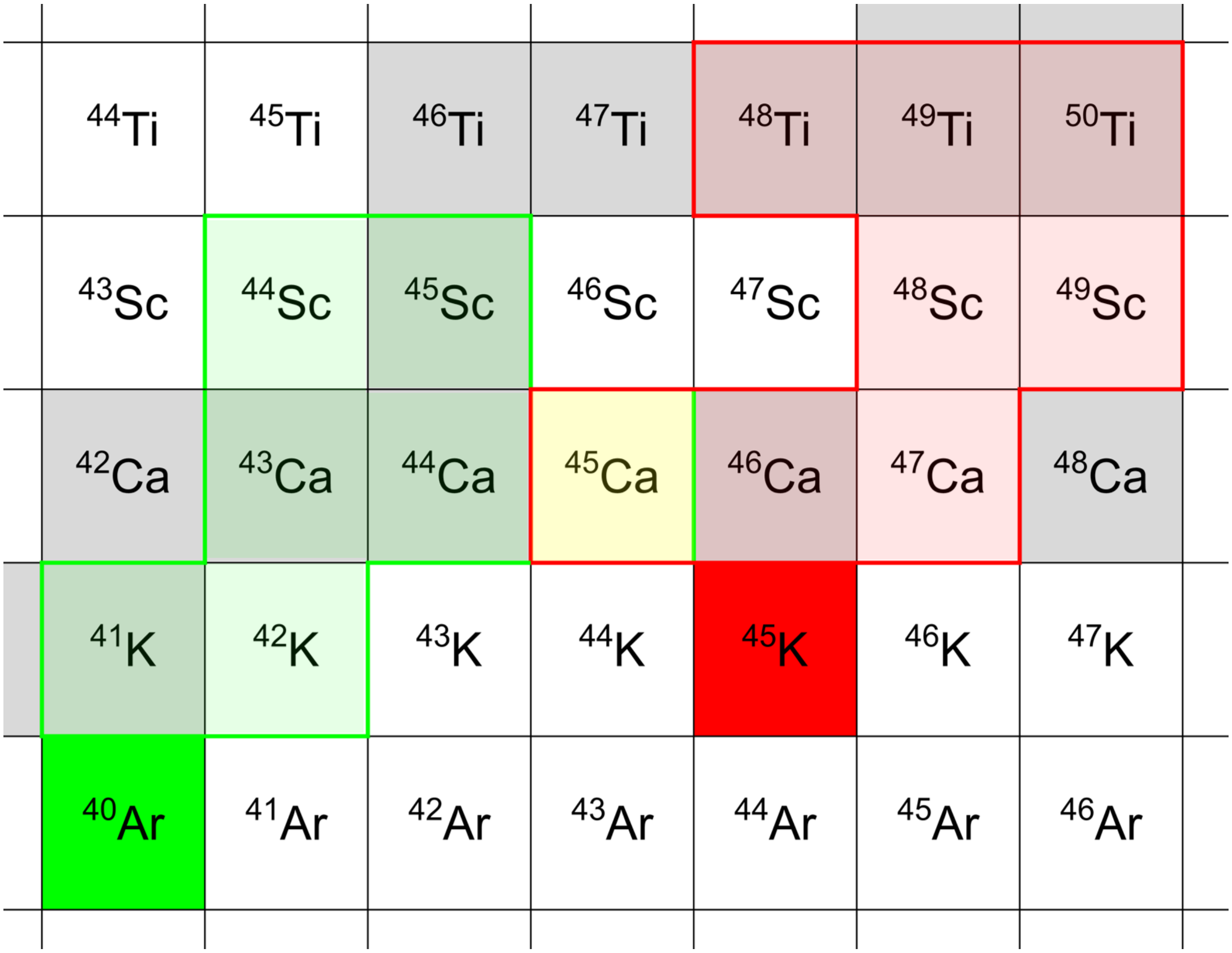

Figure 3.22: A chart of nuclei predicted to be populated via fusion-evaporation reactions according to PACE4 [85] calculations, using a ^{7}Li target. Products shaded in green are produced from the ^{40}Ar stable beam, while products shaded in red are produced from the ^{45}K RI beam. Shaded nuclei represent reaction channels with significant cross sections (50 mb or more depending on beam energy), corresponding to enough yield to potentially observe gamma rays in coincidence with SeGA.

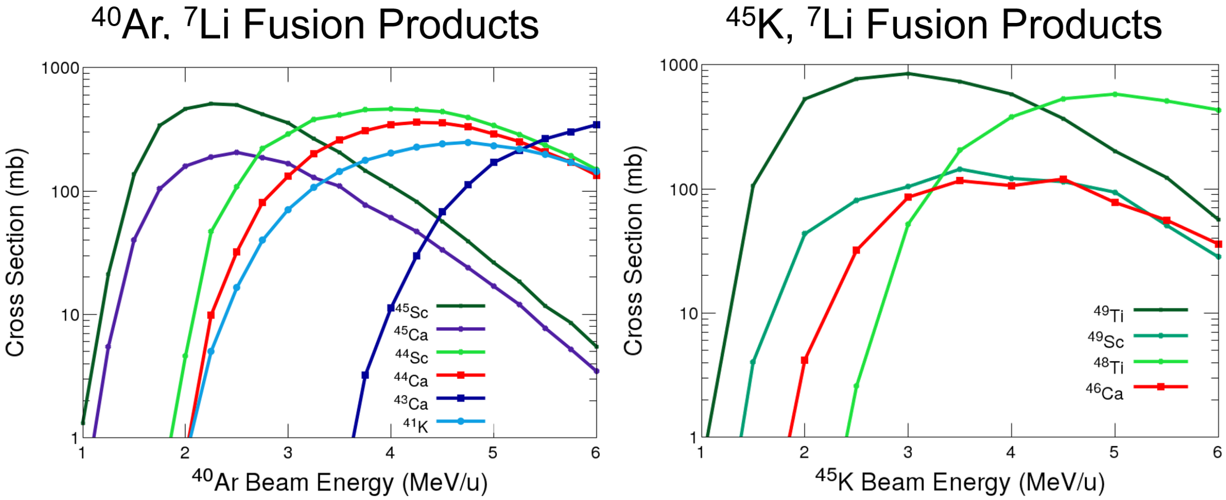

Figure 3.23: Excitation functions of the major fusion products predicted by PACE4, using a ^{7}Li target and ^{40}Ar (left) and ^{45}K (right) beams. Beam energy in the experiment ranged from the maximum 4.66 MeV/u down to 1.83 MeV/u and 1.96 MeV/u for the ^{40}Ar and ^{45}K cases respectively due to energy loss in the target. Over this range, large cross sections are expected for calcium channels, including ^{46}Ca. The channels corresponding to fusion followed by neutron evaporation (scandium for the ^{40}Ar beam and titanium for the ^{45}K beam) would not be coincident with charged particle detection in the silicon detector, while the others would be coincident with alpha particles or protons.

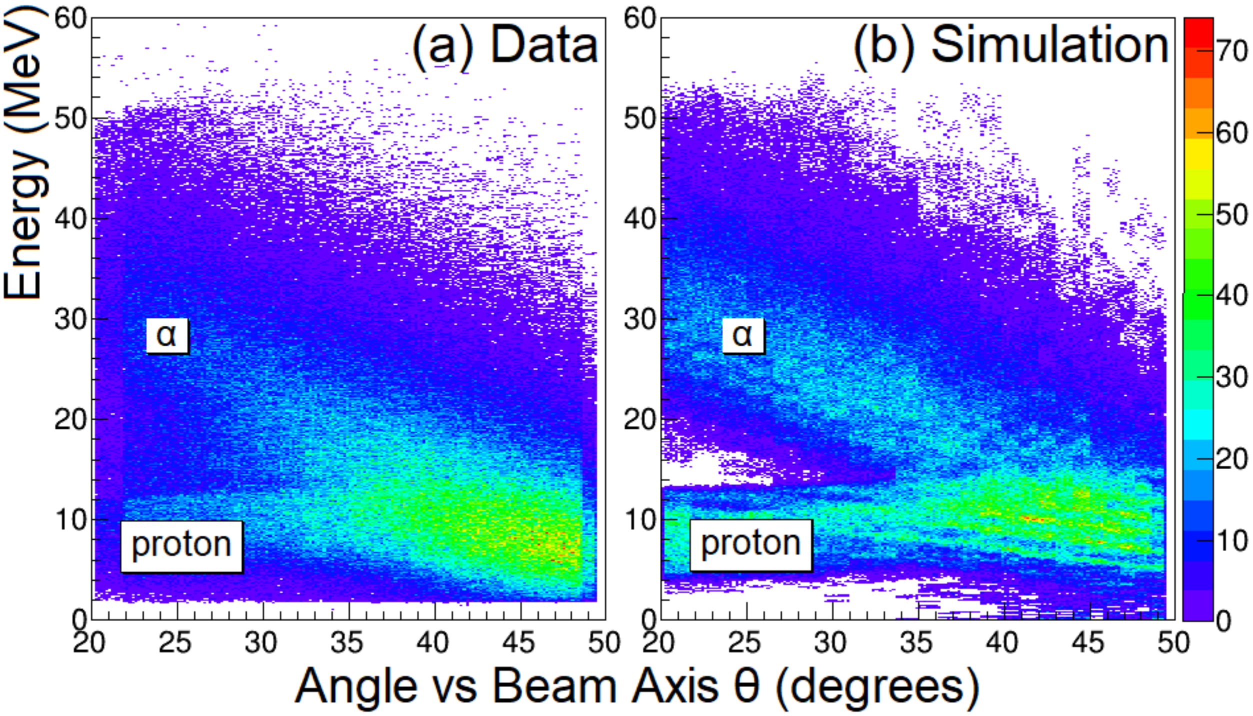

Figure 3.24: Particle identification using energy and angle information from the silicon detector. The experimental result (a) is compared with simulations (b) based on PACE4 [85] and SRIM calculations [86]. The different behaviors of proton and alpha particles are well reproduced, including the maximum deposited energy of protons at around 12-14 MeV. The visible bands in the simulation result are artifacts of the step size used in determining reaction position in the lithium target. The alpha gate mentioned in Section 4.3 is defined for each angular bin by setting a minimum deposited energy to remove proton events.

beam energy is reduced in the target, the predicted reaction products from PACE4 change to heavier nuclei, closer to the mass of the compound nucleus. With a target thickness of 5.8 mg/cm^2, the corresponding beam energies were from 4.66 MeV/u down to 1.83 MeV/u for the ^{40}Ar and 1.96 MeV/u for the ^{45}K beam. The considerations for the experimental setup also took into account the angular and energy distributions for reaction products as well as evaporated protons and alpha particles. The final distance set between the lithium target and silicon detector was chosen to maximize the predicted coverage of the alpha particles from the ^{7}Li(^{45}K,$\alpha 2n\gamma$)^{46}Ca channel.

Instead of the standard particle identification based on ΔE-E, the total energy deposited was measured in the single thick detector in order to cover the recoiling particles emitted in a wide energy range. This avoided potential loss of yield from detector dead-layer effects. As demonstrated in Figure 3.24(a), the angle-energy correlation shows that protons and alpha particles are distinguishable. This particle information provides a useful means to select reaction channels of interest. While $Z = 1$ and 2 events were not completely distinguishable, assessment of new gamma-ray transitions in this work was accomplished with the more stringent particle-gamma-gamma coincidence techniques. The measured data were reproduced by the simulated results shown in Figure 3.24(b), which was performed by prompting SRIM calculations [86] with the output of PACE4 [85] to determine the energy deposited in silicon. This included energy loss in the target, with reaction positions determined by the PACE4 excitation functions, and energy loss in the 25-μm mylar foil. The results appear in good agreement with the expectation set by Figure 3.24(b), though a difference in the angular distribution in alpha particles is clearly visible. This calculation helped to ensure the feasibility of the setup as well as quantify the effect of the mylar foil compared to foils with different thickness or from different materials.

3.6 Data Analysis Tools

This section will discuss the analysis software used and modified for this experiment. This includes methods used during the experiment, the analysis performed to to sort the read out of the NSCLDAQ framework in data structures, and the procedure used to simulate gamma-ray events from coumpound reaction mechanisms at Coulomb barrier energies.

3.6.1 Online Analysis

In order to determine the best course of action during an experiment, experimenters at NSCL need an analysis tool that can quickly sort data from active data streams and present that information in a graphical user interface. In this experiment, SpecTcl [87] was used for this purpose. SpecTcl is an object oriented C++ framework that an experimenter can use to create custom histograms and other analysis operations.

3.6.2 Offline Analysis

The analysis of data after it was taken and stored was performed in this experiment using the GRUTinizer analysis package. GRUTinizer, as detailed in Appendix A of Ref. [74], allows for the sorting of raw data from multiple detector systems using customizable configurations. GRUTinizer is multi-threaded to benefit from modern multi-core cpu architectures in modern computers, quickly sorting large quantities of data. GRUTinizer can receive data from multiple input sources, including from hard drive storage or streamed from a live experiment. The GRUTinizer package is based on CERN's ROOT framework [88], and takes advantage of ROOT's toolkit for analysis and display features.

3.6.3 Simulation

Simulations were performed as part of the data analysis for this experiment. This was carried out using the G4Lifetime program [89], which is based on the GEANT4 [90] simulation toolkit. G4Lifetime was used to simulate gamma-ray emission from decaying particles, specifically ^{46}Ca, and the response from SeGA. This subsection will focus on explaining modifications made to G4Lifetime to more accurately simulate reaction processes in experiments that proceed near Coulomb barrier energies.

The two primary modifications made to G4Lifetime allowed for a variable reaction depth in the simulated target and accounted for compound reaction kinematics by including parameterized PACE4 outputs. First, where the events are generated in the program, the option to add a generic cumulative distribution function (CDF) based on predicted cross sections was added. This CDF was evaluated with a random number to determine the reaction depth. Previously, reactions in G4Lifetime were either uniformly distributed through the target or placed at the target's center. While this works for the purpose of fast-beam experiments, for energies near the Coulomb barrier more specificity is necessary to properly simulate the emission of prompt gamma-rays from reaction products.

The second modification involves taking the energy and angular distributions of reaction products in PACE4 and including those kinematics in the simulation to account for the energy loss due to compound nucleus formation. The existing G4Lifetime assumes to first order that the momentum of beam-like products stays the same, which is consistent with direct reactions with fast beams, like knockout. However, the loss of momentum in a compound reaction is significant and needs inclusion in the simulation to reproduce observed Doppler shift on gamma-ray energies. The PACE4 output energy and angle distributions were parameterized as a function of beam energy so that the simulated reaction kinematics could be accurately reflected throughout the target (Figure 3.25).

These modifications were necessary to reproduce the observed Doppler broadening in peaks from ^{46}Ca gamma decay. Comparison of the simulation output to ^{46}Ca data can be found in Section 4.3.1. In future analysis, techniques like these can be used in gamma-ray decay lifetime measurements for similar ReA experiments.

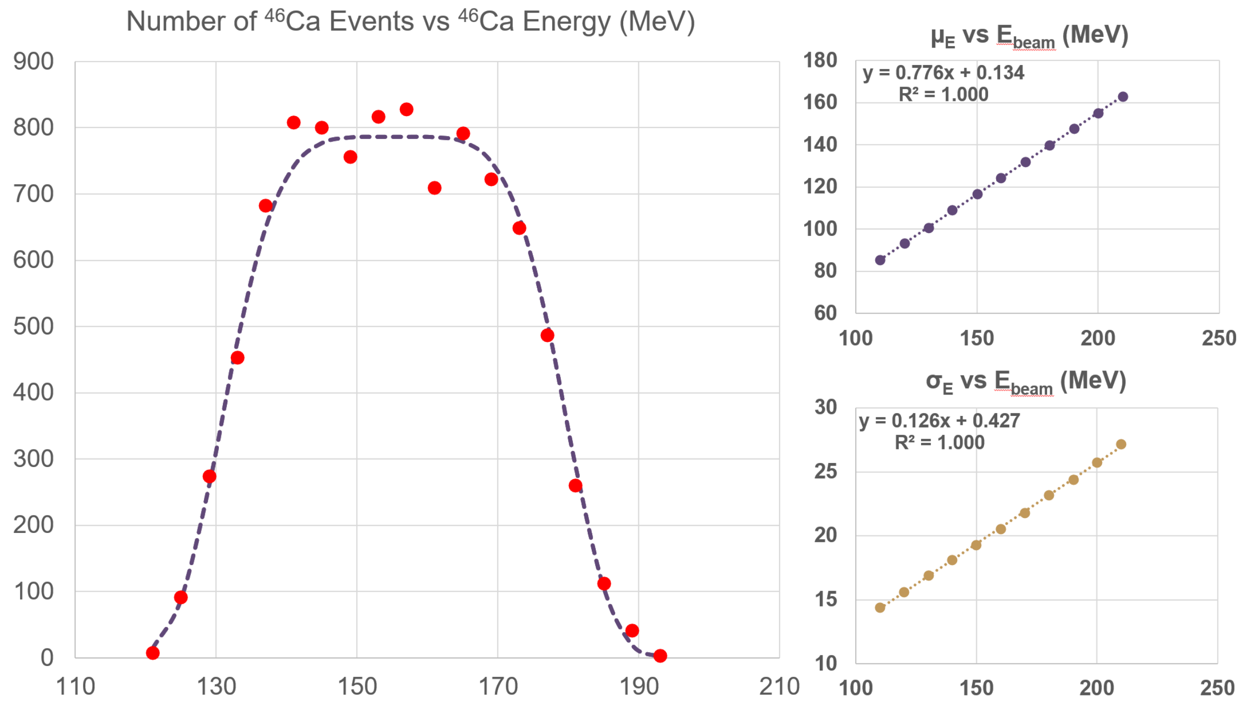

Figure 3.25: Plots illustrating the method of parameterizing the PACE4 output for ^{46}Ca fusion from ^{45}K and ^{7}Li. This allowed events to be generated in Geant4 simulations with the proper kinematics. The left plot shows an example distribution of ^{46}Ca outgoing energy for a single beam energy (in this case 200 MeV). The distribution is fit by a generalized Gaussian distribution with three parameters: β, a shape parameter, as well as the typical mean (μ) and standard deviation (σ) parameters. The latter two were fitted for different beam energies, corresponding to different reaction locations within the target, shown on the right. The shape parameter was observed to have very little dependence on beam energy and was held at a constant fitted value of 4.81.

Chapter 4

Data Analysis and Results

This Chapter details several of the results from the experiment performed at the NSCL. First, the methods used to analyze the data using particle-gamma coincidence are explained. Then, the observed reaction channels accessed with the stable ^{40}Ar beam are discussed. The methods of analysis, including the successful measurement of prompt gamma-ray transitions using particle-gamma-gamma coincidence and Doppler correction, are demonstrated. In the third section, the primary results of the experiment are presented, obtained from the use of a ^{45}K rare-isotope (RI) beam. This includes the identification of new gamma-ray cascades in the level structure of ^{46}Ca, as well as results relevant to the present neutron-transfer reaction channels to ^{46,47}K.

4.1 Particle-Gamma Coincidence

The lithium-induced reactions in this experiment populate excited states in a variety of nuclei, each of which undergoes gamma-ray emission with characteristic gamma-ray energies. However, additional particle information is necessary to confirm the origin of a given gamma-ray event detected with SeGA, especially for newly observed decays with unknown energies. To verify that events occur in coincidence, events can be correlated using their timing information. In the case of two gamma-ray events in cascade decay of an excited nucleus, coincidence can be determined if the intermediate state is sufficiently short-lived.

For coincidence events in which particle and gamma ray events are detected in different detectors, the timing information for each can be compared to a coincidence window based on the timing resolutions of the two detectors. For this experiment, charged particle ejectiles ($Z = 1$ or 2) were detected using the silicon detector, allowing for partial determination of the reaction channel of coincident gamma rays.

In Figure 4.1, gamma-ray energy from SeGA is plotted against the difference between a correlated silicon event's timestamp and the SeGA event's timestamp. The negative values shown indicate that the silicon event precedes the SeGA event; this is a constant offset from the digital data acquisition that was left uncalibrated. All signals from the two detectors that occur within a 10 microsecond window are correlated into a single event in the analysis; however this window is much larger than the practical timing resolution of the detectors. To reduce background from random coincidences, a SeGA-energy dependent timing gate was applied, as shown in red in Figure 4.1. The two-dimensional gate was necessary because a leading-edge trigger was used for SeGA events, which introduces an energy dependence for timestamps due to the increasing rise-time for lower energy gamma-ray events.

Figure 4.2 shows the equivalent spectra as the previous figure, but for the ^{45}K RI beam. Much higher counts of time-random coincident gamma rays can be observed as horizontal lines. These correspond to the ^{45}K beta decay transitions shown in the SeGA singles spectrum (Figure 3.9). The unreacted ^{45}K are collected at the beam stop and undergo beta decay with a mean lifetime of 25.7 minutes, creating significant ^{45}Ca gamma-ray background compared to the particle-coincident gamma rays. This background must be removed using the two-dimensional timing gate outlined in red. Other horizontal lines, observed in both figures, are background gamma rays from neutron-induced reactions, including $^{27}\mathrm{Al}(n, n\gamma)$ at 2212 and 3004 keV and $^{74}\mathrm{Ge}(n, n\gamma)$ at 596 and 868 keV. Neutrons emitted during reactions in the

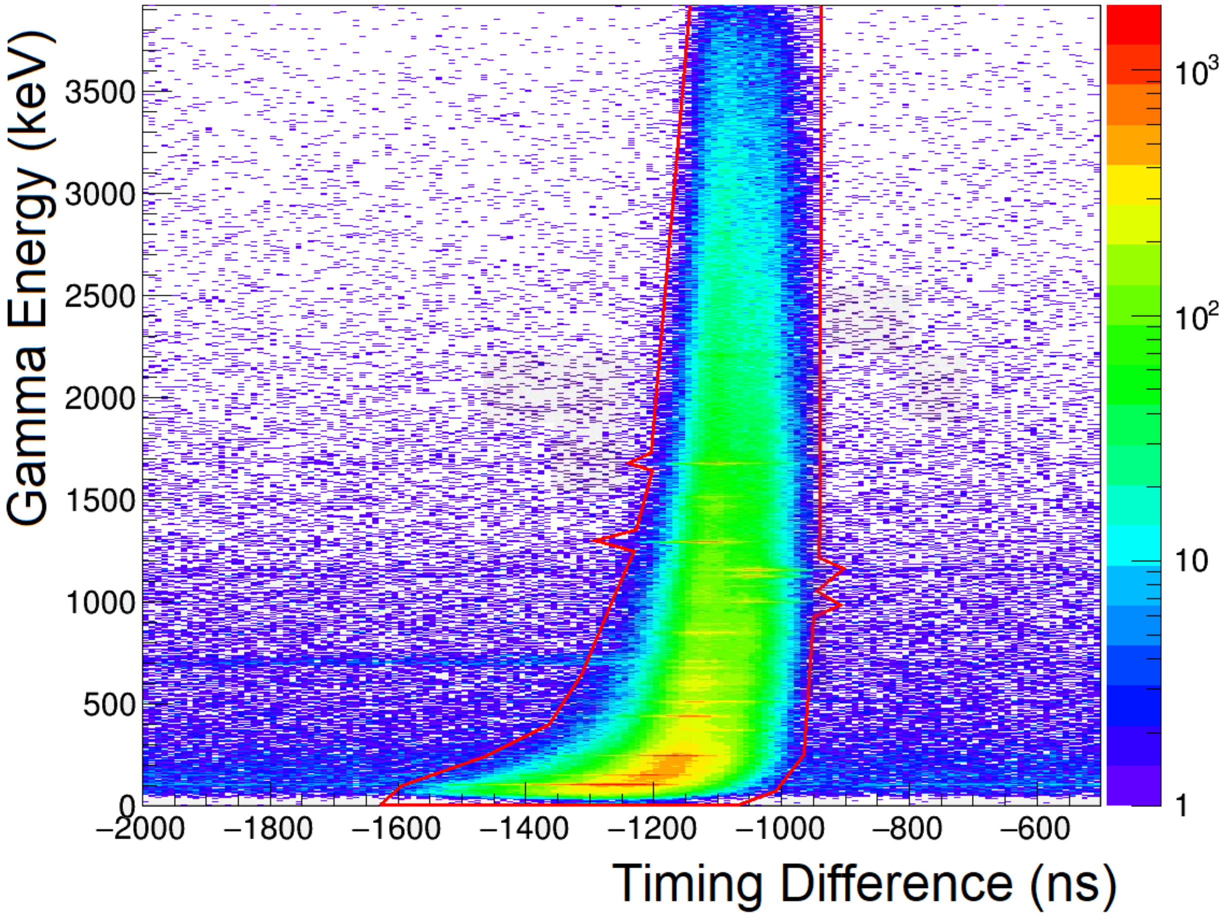

Figure 4.1: A plot for the data from the ^{40}Ar beam comparing gamma-ray energy from SeGA to the difference in time between the gamma-ray event and its associated particle event from the silicon detector. A two dimensional gate (shown in red) was necessary to account for the walk due to the gamma-ray trigger, which causes the acceptance window to shift at lower gamma-ray energies.

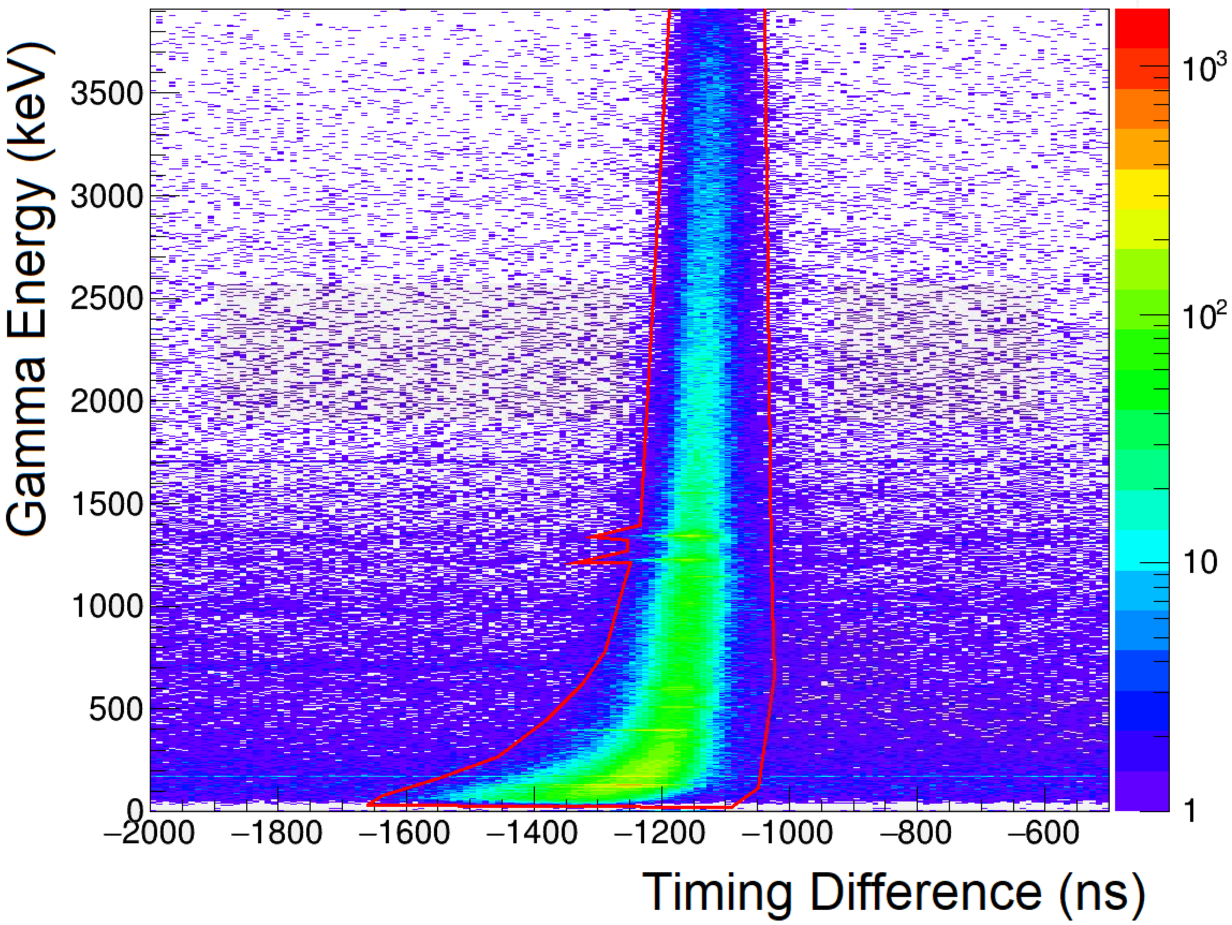

Figure 4.2: A plot for the data from the ^{45}K RI beam showing the same as Figure 4.1. ^{45}K beta decay events are seen with no timing coincidence (horizontal lines).

target create secondary reactions with the aluminum found in the detector frame, beam-line components, and the germanium crystals in SeGA.

4.2 Results Obtained from an ^{40}Ar Beam with Lithium-induced Reactions

The lithium-induced reactions from the ^{40}Ar pilot beam populated excited states in ^{41}Ar, ^{41,42}K, ^{43,44}Ca, and ^{44}Sc, which then underwent gamma decay, resulting in the spectra in Figure 4.3. The observed laboratory frame gamma rays were either significantly long lived themselves or populated from long-lived feeding transitions. This delayed emission of gamma rays ensures that the excited nucleus has stopped in the target, producing a distinct peak seen in the laboratory frame. The labelled gamma-rays are consistent with the energies of known transitions in these nuclei [91, 92, 93, 94], and are summarized in Table 4.1. In Figure 4.3(b), the particle-coincident gamma-ray spectrum is shown and plotted against the deposited energy in the silicon detector. By comparing the two spectra, it is clear that the charged particles coincident with calcium gamma-ray transitions have a maximum deposited energy of about 12 MeV. This is consistent with the expected detector response for protons shown in Figure 3.24. Therefore, an additional gate on deposited energy in the silicon detector can partially distinguish the reaction channel by selecting higher energy $Z = 2$ events. The ^{44}Sc (Z=23) channel does not emit charged particles, and so these fusion-evaporation events are not present after applying the particle gate. For the ^{7}Li(^{40}Ar,^{41}Ar)^{6}Li reaction, direct neutron transfer creates a ^{6}Li nucleus, either in a stable ground state or an unbound excited state. In the former case, the ejected ^{6}Li is not energetic enough to be measured by the silicon detector, due to the thick target and the mylar foil used to prevent

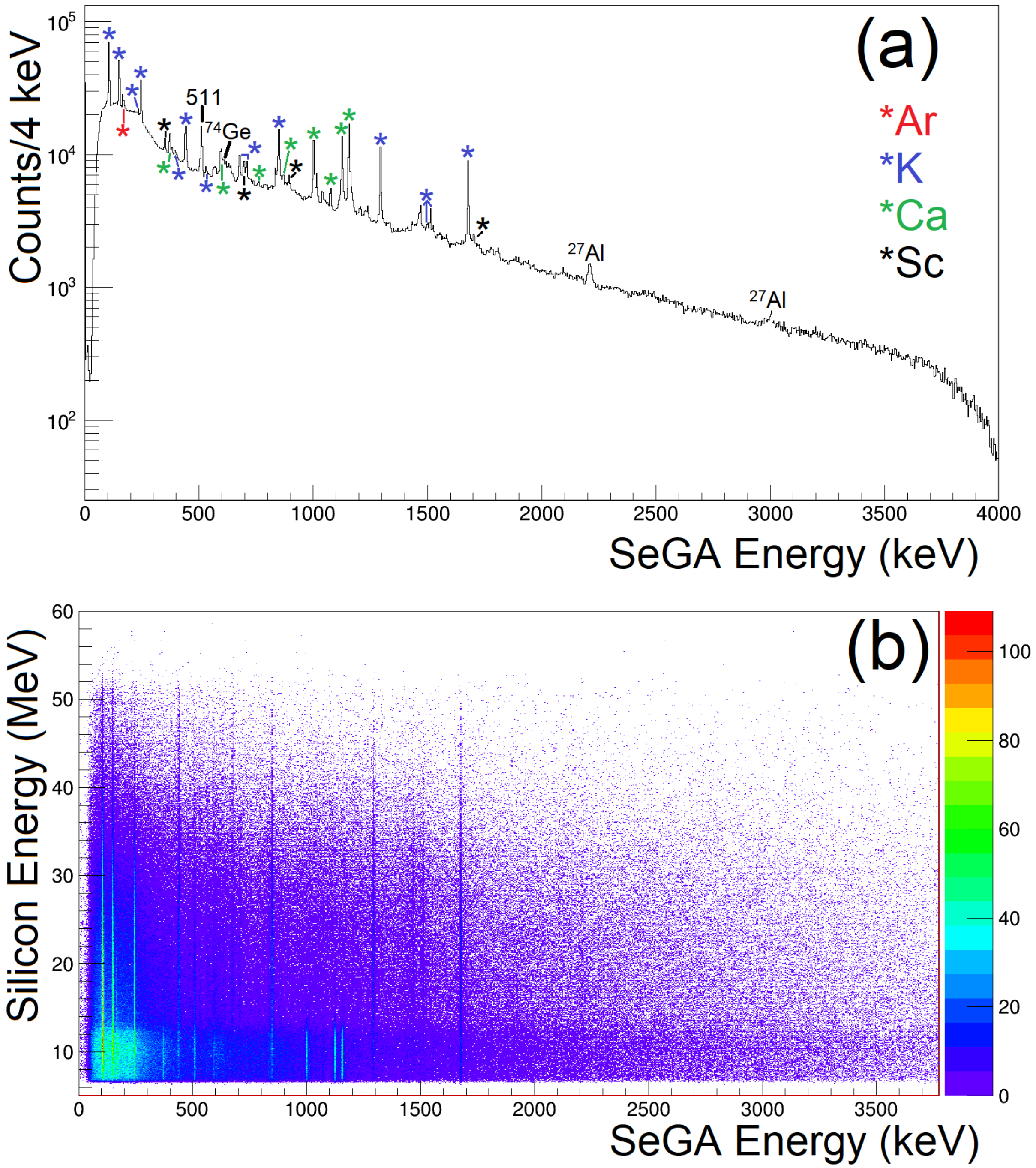

Figure 4.3: (a) Laboratory frame gamma-ray energy singles spectrum from SeGA with stable ^{40}Ar beam. Evidence of reaction products ranging from argon, potassium, calcium, and scandium isotopes are labelled. (b) Two dimensional plot of the particle-coincident gamma-ray energy spectrum against the energy of the associated particle event. Proton events, associated with ^{43,44}Ca gamma rays, appear with a maximum energy of about 12 MeV, whereas alpha particle events (^{41,42}K gamma rays) can deposit greater energy. Gamma-ray events originating from fusion-evaporation, associated with the ^{44}Sc yrast cascade, are not present in the particle-coincident spectrum.

the detection of ^{7}Li scattering events. In the case of an unbound ^{6}Li, it will spontaneously decay into an alpha particle and a deuteron, one or both of which can be detected in the silicon detector.

Two additional gamma-ray transitions were observed from reactions with the ^{40}Ar beam using Doppler effect energy correction and particle-gamma-gamma coincidence (Figure 4.4). In the analysis presented in this thesis, Doppler correction was made with simplifying assumptions for reaction kinematics. Due to the inverse kinematics of the reactions present, beam-like reaction products experienced forward focusing within approximately 6 degrees relative to the beam axis. Outgoing particles could then be assumed to travel along the beam line for the purposes of calculating the angle of gamma-ray emission. For the velocity parameter in Equation 2.11, the angular dependence of the laboratory frame-energy was used to choose a β that minimized the energy resolution after Doppler correction. By performing gamma-gamma coincidence, laboratory frame gamma rays can be used to search for Doppler-shifted gamma rays from prompt decays in cascade. In Figure 4.4, the results of this method are shown for a gate on the 1002 keV laboratory frame peak, associated with the decay of the 6^{+}_{1} state of ^{44}Ca ($\tau = 19.3$ ps), and a gate on the 677 keV laboratory frame peak, associated with the $6^{+}_{1} \rightarrow 5^{-}_{1}$ transition for ^{42}K ($\tau = 1.6$ ns). Choosing β of 0.03 and 0.065 for two Doppler-corrections produces two clear peaks at 1803(3) keV and 572(1) keV, consistent with the previously known $8^{+}_{1} \rightarrow 6^{+}_{1}$ yrast decay of ^{44}Ca ($\tau = 765$ fs) [96], and the $7^{+}_{1} \rightarrow 6^{+}_{1}$ decay of ^{42}K ($\tau < 1.6$ ps) [97].

Table 4.1 lists the gamma-ray transitions that were identified, with the intensity of the observed gamma-ray peaks with SeGA's photopeak efficiency. For the ^{41}Ar neutron transfer reaction, only the first $5/2^{-}_{1}$ excited state was significantly populated at $E_x = 167$ keV. For the other channels, several states could be identified from their gamma decays, up to $19/2^{-}_{1}$

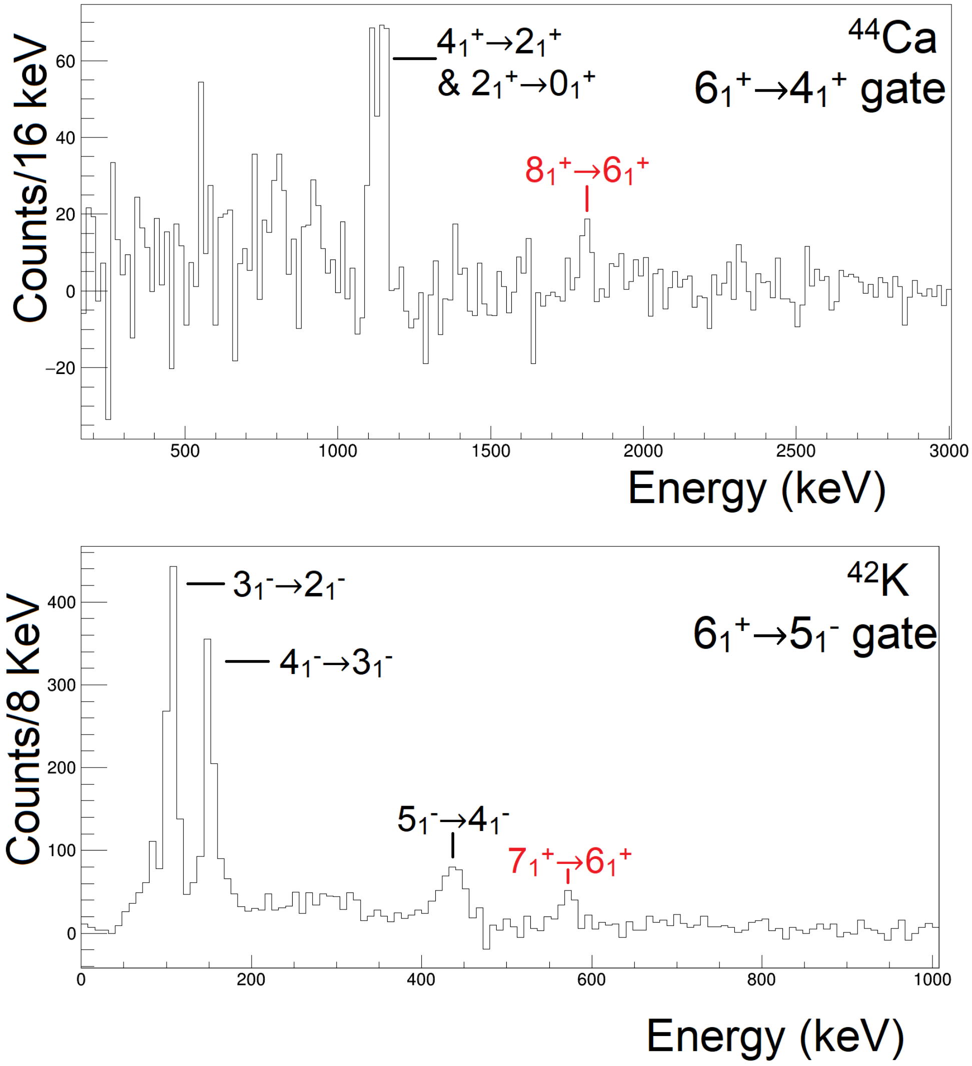

Figure 4.4: Background-subtracted particle-gamma-gamma coincidence spectra gated on (top) the 1002 keV $6_1^+ \rightarrow 4_1^+$ decay of ^{44}Ca and (bottom) the 677 keV $6_1^+ \rightarrow 5_1^-$ decay of ^{42}K. Doppler-correction with β of (top) 0.03 and (bottom) 0.065 were used. Prompt transitions are now clearly visible after Doppler-shift correction as labelled in red and listed in Table 4.1.

Nucleus	E_{initial} (keV)	$J_i^\pi \rightarrow J_f^\pi$	E_γ (keV)	E_{final} (keV)	I_γ
^{41}Ar	167.1(5)	$5/2_1^- \rightarrow 7/2_1^-$	167.5(5)	0	100
^{41}K	1293.7(5)	$7/2_1^- \rightarrow 3/2_1^-$	1293.7(5)	0	100
	1677.2(5)	$7/2_1^+ \rightarrow 3/2_1^-$	1677.2(5)	0	97.2(8)
	2528.2(7)	$11/2_1^+ \rightarrow 7/2_1^+$	851.0(5)	1677.2	95(1)
	2762.3(7)	$11/2_1^- \rightarrow 7/2_1^-$	1468.6(5)	1293.7	22(1)
	2774.7(9)	$13/2_1^+ \rightarrow 11/2_1^+$	246.6(5)	2528.2	58.2(8)
	4275(1)	$15/2_1^- \rightarrow 13/2_1^+$	1500.4(5)	2774.7	6(2)
		$15/2_1^- \rightarrow 11/2_1^-$	1513.1(5)	2762.3	17(1)
	4983(1)	$19/2_1^- \rightarrow 15/2_1^+$	708.7(5)	4275	17(1)
^{42}K	106.5(5)	$3_1^- \rightarrow 2_1^-$	106.5(5)	0	100
	257.7(7)	$4_1^- \rightarrow 3_1^-$	151.2(5)	106.5	84.1(8)
	638.5(7)	$3_2^- \rightarrow 4_1^-$	381(1)	257.7	3(1)
		$3_2^- \rightarrow 3_1^-$	531.8(5)	106.5	5(1)
		$3_2^- \rightarrow 2_1^-$	638.4(5)	0	3(1)
	698.6(9)	$5_1^- \rightarrow 4_1^-$	440.7(5)	257.7	62.3(8)
	1143.1(7)	$4_1^+ \rightarrow 3_2^-$	504.6(5)	638.5	3(3)
	1375(1)	$6_1^+ \rightarrow 4_1^+$	232.8(5)	1143.6	5(3)
		$6_1^+ \rightarrow 5_1^-$	676.9(5)	698.6	20(1)
	1538.7(9)	$3_2^+ \rightarrow 4_1^+$	395.6(5)	1143.6	5(3)
	1947(1)	$7_1^+ \rightarrow 6_1^+$	572(1)	1375	5(2)
^{43}Ca	372.7(5)	$5/2_1^- \rightarrow 7/2_1^-$	372.7(5)	0	100
	1678.0(5)	$11/2_1^- \rightarrow 7/2_1^-$	1678.0(5)	0	88(5)
	2754.5(7)	$15/2_1^- \rightarrow 11/2_1^-$	1076.5(5)	1678.0	91(1)
^{44}Ca	1157.4(5)	$2_1^+ \rightarrow 0_1^+$	1157.4(5)	0	100
	2283.8(7)	$4_1^+ \rightarrow 2_1^+$	1126.4(5)	1157.4	72.9(8)
	3044(1)	$4_2^+ \rightarrow 4_1^+$	761(1)	2283.8	2(1)
	3286.0(9)	$6_1^+ \rightarrow 4_1^+$	1002.2(5)	2283.8	43.5(8)
	3913(1)	$5_1^- \rightarrow 6_1^+$	629(1)	3286.0	2(1)
		$5_1^- \rightarrow 4_2^+$	868.9(5)	3044	5(2)
	5091(3)	$8_1^+ \rightarrow 6_1^+$	1805(3)	6386.0	2(2)
^{44}Sc	350	$4_1^+ \rightarrow 2_1^+$	349.6(5)	0	35.3(8)
	968.2(5)	$7_1^+ \rightarrow 6_1^+$	697.0(5)	271.24	100
	2671.5(7)	$9_1^+ \rightarrow 7_1^+$	1703.3(5)	968.2	33(4)
	3566.4(9)	$11_1^+ \rightarrow 9_1^+$	894.9(5)	2671.5	40(3)

Table 4.1: The experimental energy levels and transitions observed in products of lithium-induced reactions with the ^{40}Ar stable beam. Relative intensity (I_γ) is presented and corrected by a scaling factor that accounts for differences in gamma-ray efficiencies [95].

for ^{41}K, 7_1^+ for ^{42}K, $15/2_1^-$ for ^{43}Ca, 8_1^+ for ^{44}Ca, 11_1^+ for ^{44}Sc. The spins of these states indicate a preference of lithium-induced reactions to populate high-spin yrast states. For the ^{44}Sc fusion-evaporation channel, the 6_1^+ state at $E_x = 271$ keV is known to decay primarily by internal conversion to the 2_1^+ ground state with a mean lifetime of 84.6 hours; therefore, this transition was not observed during the experiment. As listed in the table, the 4_1^+ state is higher lying than the 6_1^+, so the typical E2 decay is impossible. Two gamma rays, the 1678.0(5) keV $11/2_1^- \rightarrow 7/2_1^-$ decay for ^{43}Ca and the 1677.2(5) keV $7/2_1^+ \rightarrow 3/2_1^-$ decay for ^{41}K, overlap in energy. Background-subtracted gamma-gamma coincidence was used, leading to greater uncertainty in the intensity of the ^{43}Ca $11/2_1^-$ decay.

4.3 Results Obtained from a ^{45}K Beam with Lithium-induced Reactions

Using the ^{45}K RI beam, new states and transitions were identified using similar methods as the ones explained above. The laboratory-frame spectrum of gamma-ray energies from events coincident with recoiling light particles is shown in Figure 4.5. The gamma rays labelled as ^{45,46}Ca should be coincident with alpha particles, which can deposit more energy in the silicon detector than the protons from ^{47,48}Sc reaction channels. To select only alpha particles for the purpose of corroborating potential calcium gamma-ray emission, an alpha gate was defined based on the silicon detector response. Rather than a constant energy threshold that excludes all lower energy events, the angular dependence of the energy deposition as indicated by Figure 3.24 was taken into account.

With the application of the alpha gate, the ^{45,46}Ca peaks remain, including three peaks with energies consistent with the ^{46}Ca yrast decays $6_1^+ \rightarrow 4_1^+$, $4_1^+ \rightarrow 2_1^+$, and $2_1^+ \rightarrow 0_1^+$ at

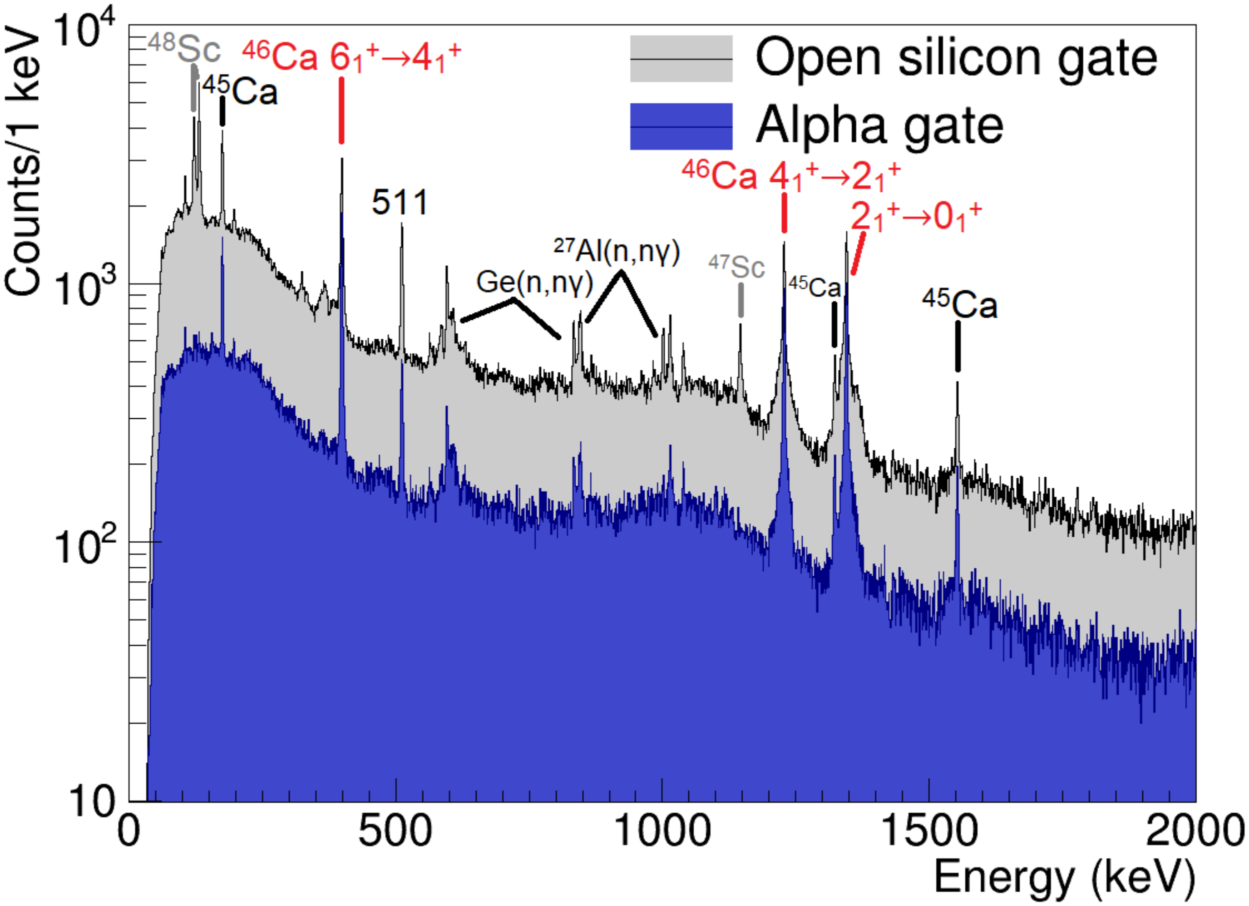

Figure 4.5: Laboratory-frame particle-gamma coincidence spectrum. The plot compares the spectra with an open gate against the results when gating on alpha particles. Gamma-ray peaks from the reaction products ^{45,46}Ca and ^{47,48}Sc are labelled, as well as background from neutron-induced reactions.

399.2(5), 1228.7(5), and 1346.0(5) keV, respectively. This 6_1^+ state is a known isomer with a mean lifetime τ of 15.0(7) ns [98, 99]; consequently, these decays occur after the nucleus has stopped in the target, resulting in a sharp peak. However, the $4_1^+ \rightarrow 2_1^+$ and $2_1^+ \rightarrow 0_1^+$ decays have broad shoulders on either side of the peaks. These originate from the Doppler-broadening experienced in events where the 4_1^+ and 2_1^+ states are populated directly and decay promptly, while the ^{46}Ca is still in flight. There are also three peaks present from the decay of ^{45}Ca, corresponding to $5/2_1^- \rightarrow 7/2_1^-$, $(11/2^-)^- \rightarrow 7/2_1^-$, and $(15/2^-) \rightarrow (11/2^-)$ transitions at 174, 1554, and 1324 keV. The latter two of these decays are from states previously populated in fusion evaporation reactions, where they were given their tentative assignments and determined to have mean lifetimes greater than 3 ps [96]. However, unlike the $(11/2^-)$ and $(15/2^-)$ states, the $5/2_1^-$ state is populated from the beta decay of ^{45}K, which populates low-lying ^{45}Ca states in the gamma-ray singles spectrum. This produces a large gamma-ray background to the measurement of lithium-induced reaction products due to the ^{45}K RI beam. It was determined that the expected random coincidences with charged particle detection would only account for about 10 percent of the intensity seen in the $5/2_1^- \rightarrow 7/2_1^-$ peak in Figure 4.5, implying that the state is significantly populated with lithium-induced reactions. Lastly, the same neutron-induced aluminum and germanium background peaks are still present that were in the results from the ^{40}Ar beam.

The following subsections will present the primary results of this thesis. First, excited states in ^{46}Ca populated with the ^{7}Li(^{45}K,$\alpha 2n\gamma$)^{46}Ca reaction channel are explored, including the observation of new states and transitions. Then, results for the direct neutron transfer channels to ^{46,47}K are presented, including the extraction of differential cross sections.

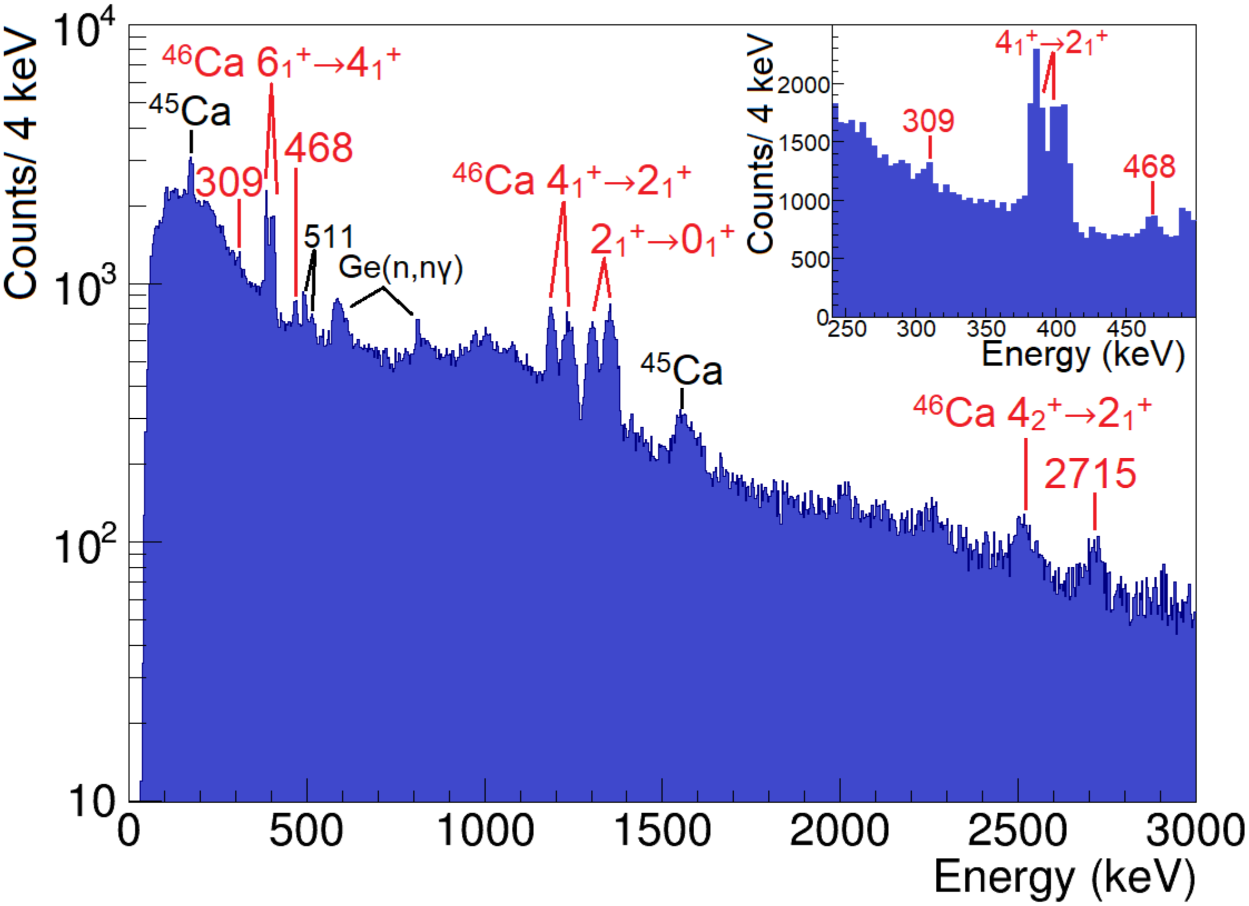

Figure 4.6: Doppler-corrected particle-gamma coincidence spectrum, with a gate on alpha particles. A fast transition known from ^{46}Ca is observed ($4_2^+ \to 2_1^+$) [40], as well as newly identified peaks at 468 and 2715 keV and a peak structure at 309 keV, as seen in the inset. Laboratory-frame gamma rays are seen as doublets due to the different geometrical effects of the forward and backward SeGA detectors in the Doppler correction.

4.3.1 ^{46}Ca

As explained in the previous section, the velocity parameter for Doppler correction was tuned to correct angular dependence of each peak of interest. Figure 4.6 presents the alpha-gated Doppler-corrected spectrum with $\beta = 6.75\%$. The effect of Doppler-correction on peaks from the laboratory frame spectrum is to split the peak into higher and lower energy structures, corresponding to the forward and backward rings of SeGA. This feature is visible for the $6_1^+ \to 4_1^+$, $4_1^+ \to 2_1^+$, and $2_1^+ \to 0_1^+$ transitions. A recently discovered ^{46}Ca prompt decay,

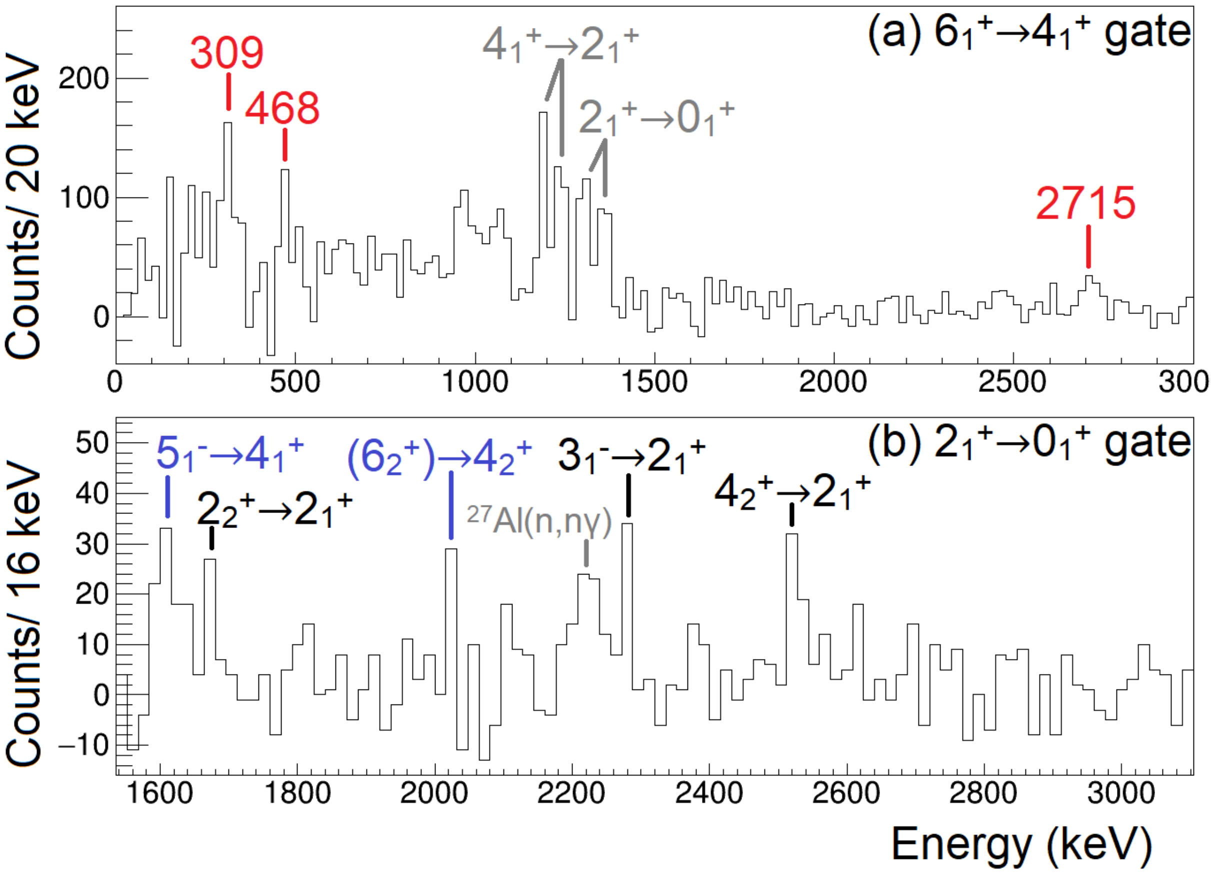

Figure 4.7: Background-subtracted particle-gamma-gamma coincidence gated on 399-keV (a) and 1346-keV (b) gamma rays confirmed new ^{46}Ca transitions. New transitions to (un)known states are labeled in blue (red). The counts around 900-1100 keV in (a) are remnants of the Compton edges of the 4_1^+ and 2_1^+ decays.

$4_2^+ \to 2_1^+$ [40], is corroborated by the broad peak observed at a consistent energy of 2513(3) keV. In addition, the gamma-ray spectrum clearly presents newly identified peaks at 468 and 2715 keV, together with a peak structure at 309 keV. There is also a hint of a peak visible at 2006 keV. These alpha-coincident peaks are confirmed to be from ^{46}Ca by means of gamma-gamma coincidence.

By gating on the transition for the 6_1^+ decay, these three new transitions were confirmed at 309, 468, and 2715 keV (Figure 4.7(a)) and found to decay in a cascade above the 6_1^+ based on mutual coincidence relations (Figure 4.8). The 2715-keV gamma ray has a higher

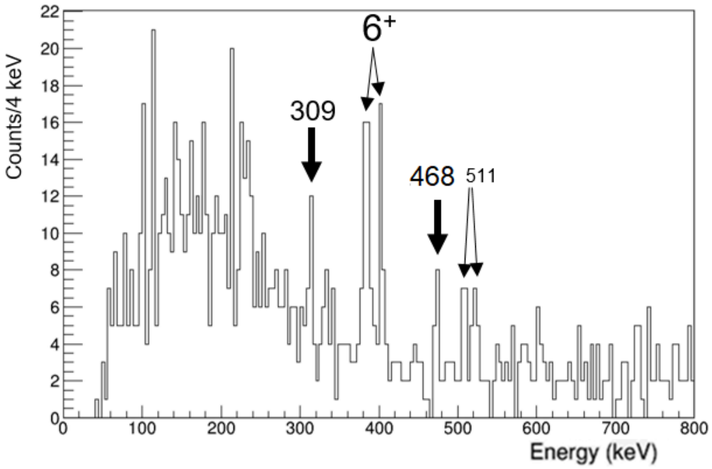

Figure 4.8: Particle-gamma-gamma coincidence gated on 2715-keV gamma rays, showing mutual coincidence with the 309- and 468-keV transitions.

intensity than the other two gamma rays in the cascade, leading to the level scheme shown in Figure 4.9 and Table 4.2. The 309-keV and 468-keV transitions had equivalent intensities, so tentative placement in the level scheme was based on the ideal value of β for Doppler-shift correction ($\beta = 6.75\%$ for 309 keV and $\beta = 6.5\%$ for 469 keV). In addition, the gamma-ray peaks which correspond to decays from known states, including 5^- and (6_2^+) whose J^π were originally deduced from angular distributions of (t,p) reactions [37], were newly observed in the present study using coincidence with the decay of the first excited state ($J^\pi = 2_1^+$), as shown in Figure 4.7(b). It should be noted that the energy gate used to select alpha particles is removed for Figure 4.7 to maximize yields in ^{46}Ca gamma rays.

Figure 4.10 contains comparisons of alpha-gated ^{46}Ca data and a simulation performed using a modified version of G4LifeTime [89]. While not essential to the spectroscopy results summarized in Table 4.2, these simulations informed the identification of new peaks and the uncertainty in their Doppler-corrected energies by reproducing observed energy resolutions. In Figure 4.10(a), the broad shoulders in the data for $4_1^+ \rightarrow 2_1^+$ and $4_1^+ \rightarrow 2_1^+$ peaks is

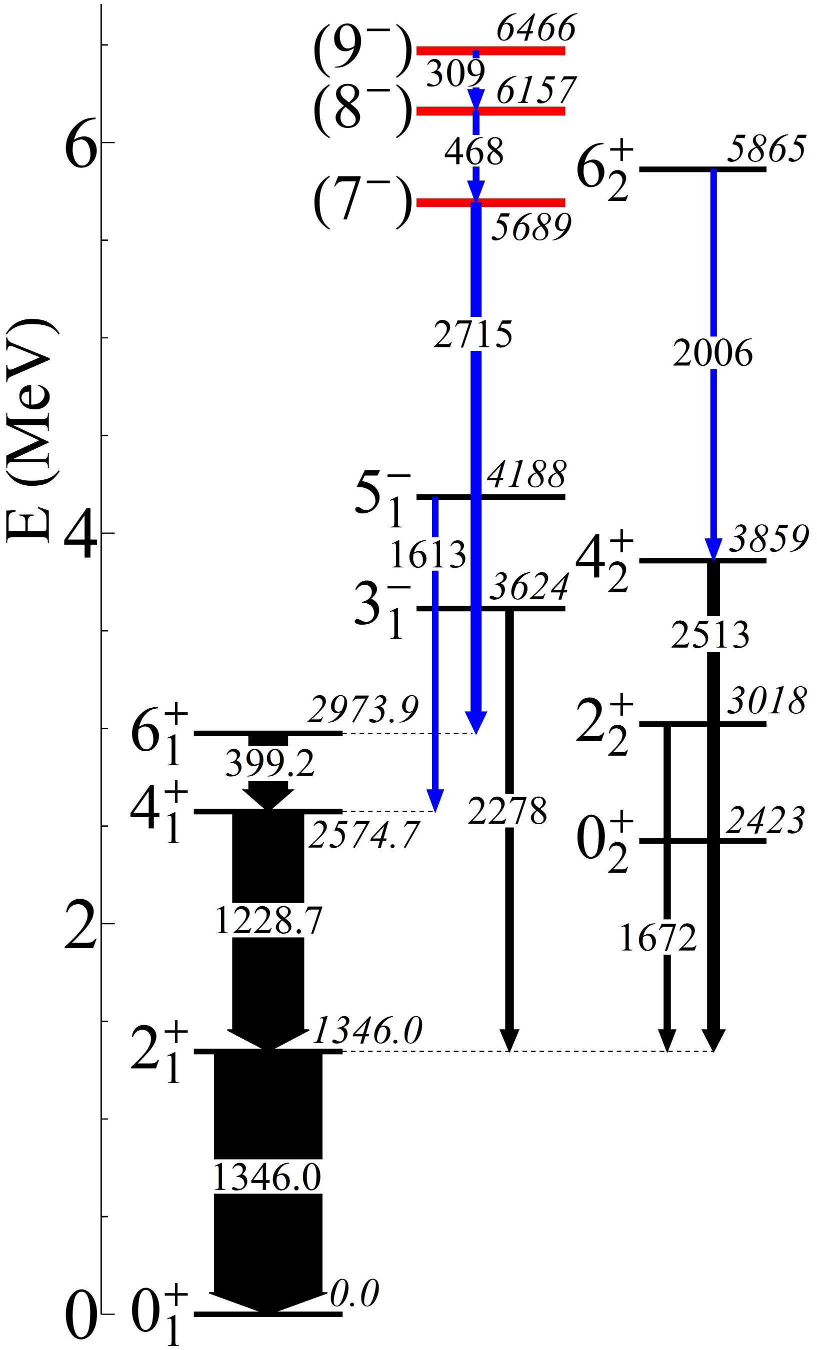

Figure 4.9: Experimental level scheme of ^{46}Ca. Excited states (gamma-ray transitions) newly identified from this work are shown in red (blue).

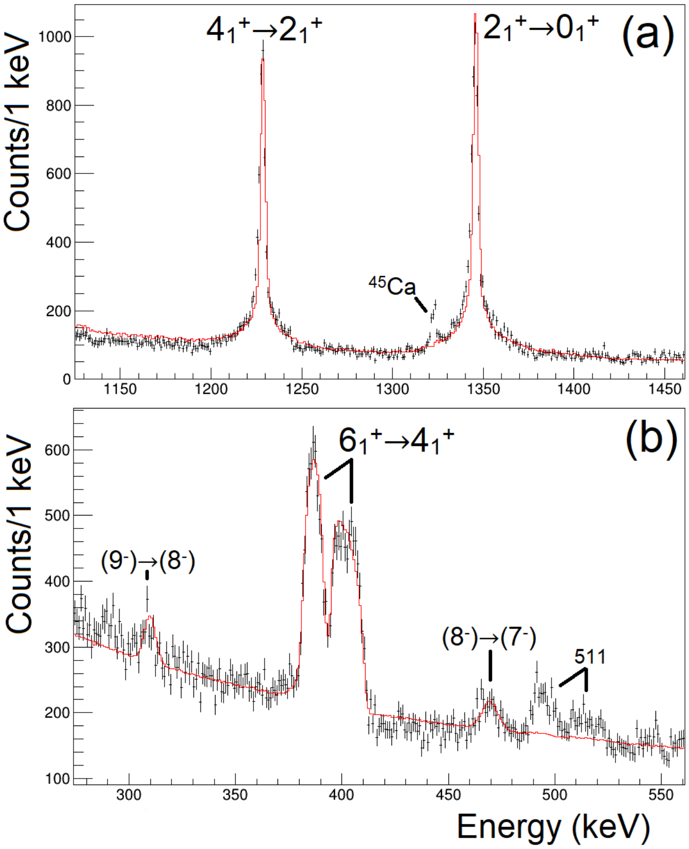

Figure 4.10: Output of G4Lifetime simulation of gamma radiation from a ^{7}Li(^{45}K,α2n)^{46}Ca fusion reaction (using the Geant4 toolset). (a) Laboratory-frame spectrum. The shoulders on the $4_1^+ \rightarrow 2_1^+$ and $4_1^+ \rightarrow 2_1^+$ peaks are reproduced. (b) Doppler-corrected spectrum ($\beta = 6.75\%$). The observed resolution of the new peaks is consistent with expectation.

E_{initial} (keV)	$J_i^\pi \to J_f^\pi$	E_γ (keV)	E_{final} (keV)	I_γ
1346.0(5)	$2_1^+ \to 0_1^+$	1346.0(5)	0	100
2574.7(7)	$4_1^+ \to 2_1^+$	1228.7(5)	1346.0	65.9(6)
2973.9(9)	$6_1^+ \to 4_1^+$	399.2(5)	2474.7	35.7(6)
3018(3)	$2_2^+ \to 2_1^+$	1672(3)	1346.0	3.0(19)
3624(4)	$3_1^- \to 2_1^+$	2278(4)	1346.0	6.5(10)
3859(3)	$4_2^+ \to 2_1^+$	2513(3)	1346.0	10.8(14)
4188(3)	$5_1^- \to 4_1^+$	**1613(3)**	2574.7	4.8(7)
5689(2)	$(7^-) \to 6_1^+$	**2715(2)**	2973.9	9.2(14)
5865(5)	$(6_2^+) \to 4_2^+$	**2006(3)**	3859	5.1(11)
6157(3)	$(8^-) \to (7^-)$	**468(2)**	5689	4.5(6)
6466(4)	$(9^-) \to (8^-)$	**309(2)**	6157	5.7(8)

Table 4.2: The levels of ^{46}Ca identified in this experiment. Intensity (I_γ) is presented relative to the 1346-keV gamma-ray yield and is corrected by a scaling factor that accounts for differences in gamma-ray efficiencies [95] as well as effective target thickness available for each reaction channel. New results from this experiment are in bold, others are in agreement with accepted ENSDF values [100]. The tentative spin-parity assignments for the new states are discussed in Section 5.1.1.

reproduced. The amount of observed Doppler-broadening was confirmed to be a lifetime effect from directly populating these states; without the feeding from the isomeric 6_1^+ state, these decays happen at least partially in-flight, implying an upper bound on their lifetime. In this experiment, the sensitivity to lifetime was very low, but similar techniques could be used for future experiments. This comparison informed the uncertainty in the intensity of the 4_1^+ and 2_1^+ decays. In Figure 4.10(b), the simulated new peaks for the 468- and 309-keV transitions have resolutions consistent with the ones from data. The sensitivity to the choice of β for these peaks, i.e. the degree to which the peaks experienced Doppler-broadening, helped to corroborate their assignment as prompt ^{46}Ca decays, and informed the quantification of uncertainty in the true energy of the gamma-ray transitions.

4.3.2 ^{46,47}K

The direct neutron transfer channels for the ^{45}K beam required an additional gate to distinguish the resulting gamma rays from the other results. In one neutron transfer, the ^{6}Li ejectile can decay into an alpha particle and deuteron, if ^{6}Li is in an excited state. The ground state of ^{5}Li is unbound, so in the case of two neutron transfer an alpha particle and proton are always created. These two particles have a chance of reaching the silicon detector at nearly the same time. Therefore the application of a multiplicity-2 gate for charged particles was found to be essential to clearly identify the potassium events from the gamma-ray background. Figure 4.11 shows the resulting Doppler corrected energy spectrum ($\beta = 0.03$), showing a clean spectra with a series of peaks consistent with known ^{46,47}K transitions. In the inset of Figure 4.11 is an experimental level scheme for the one neutron transfer case, while for ^{47}K only the first excited state of $3/2_1^+ \rightarrow 1/2_1^+$ was populated. The strong population of the $3/2_1^+$ state in ^{47}K via two-neutron transfer from the $3/2_1^+$ ground state of ^{45}K indicates a correspondence between the two states. This will be discussed further in Section 5.2. The similar magnitude for the one-neutron and two-neutron channels may be surprising, given an expected order of magnitude difference in one-neutron and two-neutron transfer cross sections. However, this is related to the possibility that the ground state of ^{6}Li is populated in one-neutron transfer. In such an event, the ^{6}Li does not decay, and so the event is excluded from the multiplicity-2 gate.

Differential cross sections were extracted from the intensities of the peaks in Figure 4.11, resulting in Figure 4.12. The observed gamma-ray decays are listed in Table 4.3. In order to calculate the differential cross section, the ^{5,6}Li laboratory-frame angle after the reaction was reconstructed by looking at the two hits in the silicon detector on an event-by-event basis.

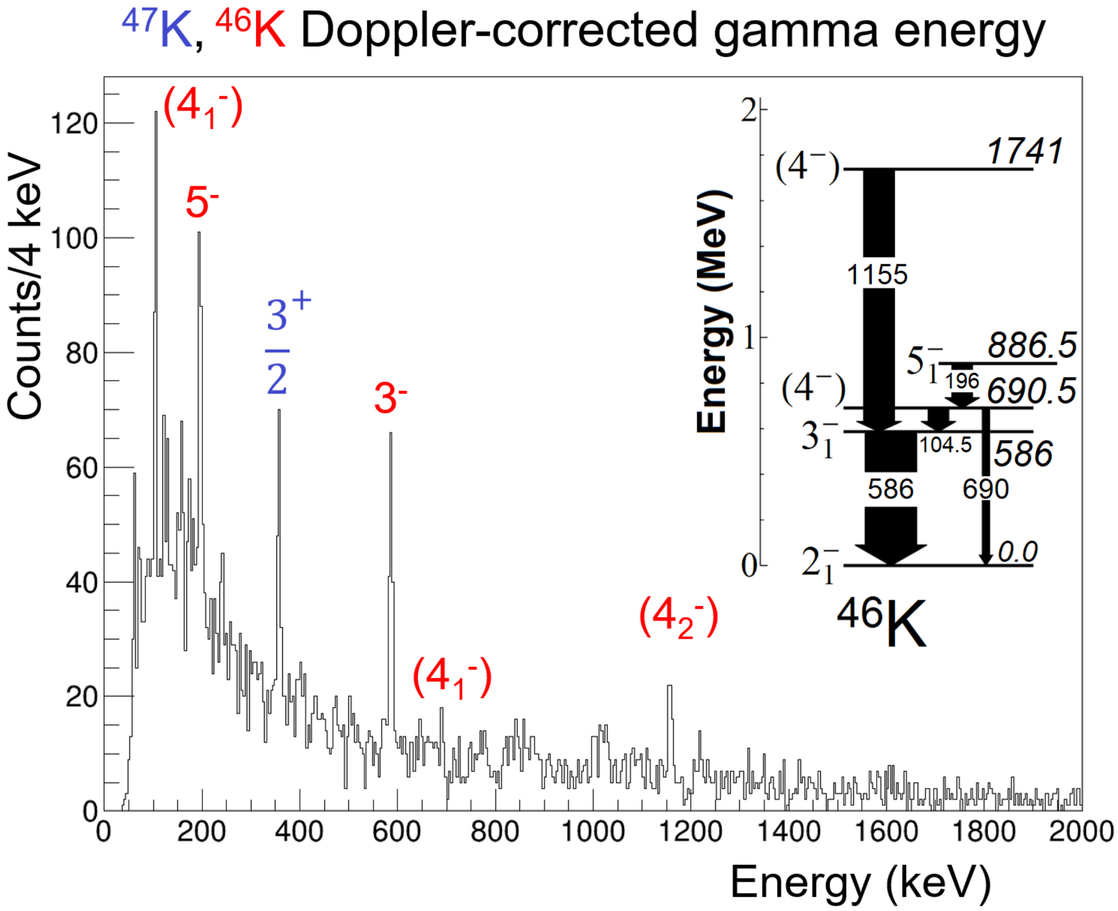

Figure 4.11: Experimental gamma-ray spectrum showing ^{46,47}K gamma rays, produced by a multiplicity 2 cut on events in the silicon detector. A level scheme of the observed ^{46}K states (labelled in red) is shown, with intensity represented by the widths of the transition arrows. A β for Doppler correction of 0.03 was used that minimized Doppler broadening observed in the peak from $3/2^+$ first excited state decay in ^{47}K (labelled in blue).

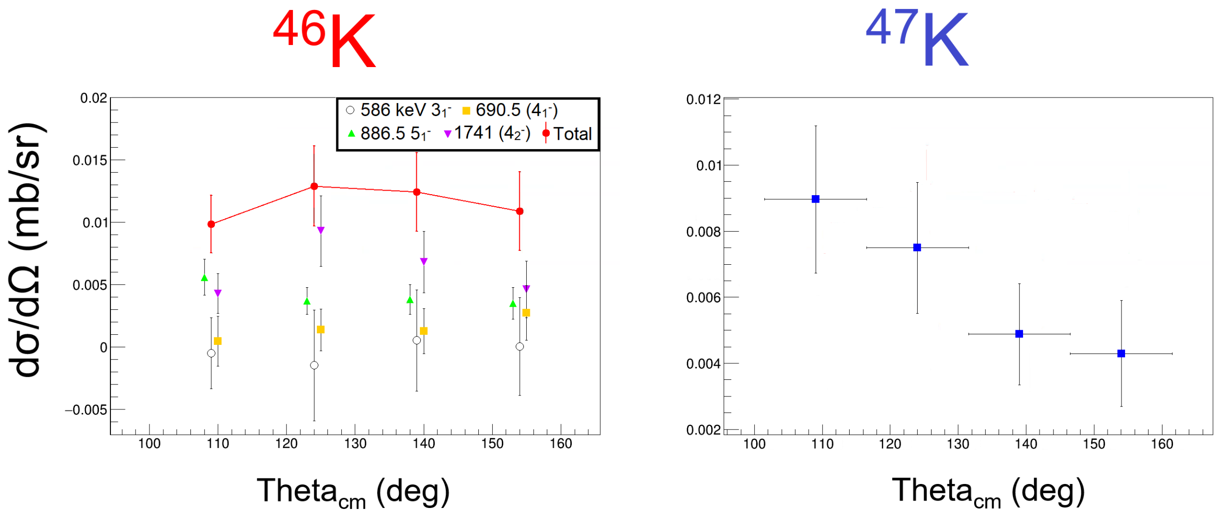

Figure 4.12: Partial differential cross section extracted from gamma ray intensities for ^{46,47}K. (Left) When compared to the level scheme in Figure 4.11, it appears that only the two higher-lying observed states were directly populated to a significant degree. Horizontal error bars are omitted here for clarity; the four angular bins have a width of 15 degrees. (Right) unlike the isotropic distribution for ^{46}K, the differential cross section shows a clear trend for ^{47}K two neutron decay.

Nucleus	E_{initial} (keV)	$J_i^\pi \to J_f^\pi$	E_γ (keV)	E_{final} (keV)	I_γ
^{46}K	586(1)	$3_1^- \to 2_1^-$	586(1)	0	100
	690.5(10)	$(4_1^-) \to 3_1^-$	104.5(8)	586	37(2)
		$(4_1^-) \to 2_1^-$	690(1)	0	13(6)
	886.5(10)	$5_1^- \to (4_1^-)$	196(1)	690.5	44(2)
	1741(2)	$(4_2^-) \to 3_1^-$	1155(2)	586	63(2)
^{47}K	359(1)	$3/2_1^- \to 1/2_1^-$	359(1)	0	100

Table 4.3: The experimental energy levels and transitions observed from $^{46.47}$K identified in this experiment. Relative intensity (I_γ) is presented and corrected by a scaling factor that accounts for differences in gamma-ray efficiencies [95].

The energy and angular information from the events were used to calculate the ejectile's trajectory, with the larger of the two energy deposits assumed to be the alpha particle, and the other the proton/deuteron. This was converted to a center-of-mass frame, and events were grouped into four angular bins with 15 degree widths. These bins do not account for the total angular coverage of the silicon detector, in order to correct for the silicon detector's acceptance. Errors are primarily statistical from the measured gamma-ray intensities, with errors in target thickness, beam intensity, etc. also included. The total differential cross section is consistent with an isotropic distribution.

The differential cross section for each of the states observed in ^{46}K is shown in Figure 4.12, with corrections for feeding included. The cross sections to the 3^-_1 and (4^-_1) states at 586 and 690.5 keV indicate that these states are not directly populated, but are instead fed by the 5^-_1 and (4^-_2) states at 886.5 and 1741 keV. For the two-neutron transfer to the $3/2^-_1$ state in ^{47}K, a trend emerges in the differential cross section. Interpretation of this trend is explored in Section 5.2.

Chapter 5

Discussion of Results

The new results for ^{46}Ca and ^{47}K from this work bring with them an improved understanding of nuclear structure in this region. For ^{46}Ca, comparison with shell model calculations reveals three distinct band structures in this nucleus, implying the continuation of shape coexistence from lighter mass calcium nuclei. The differential cross section of the two-neutron transfer reaction for ^{47}K is also compared to theoretical calculations. The comparison supports the direct reaction nature of this reaction process and therefore demonstrates the usefulness of such reactions in probing structural changes in neutron-rich nuclei.

5.1 Interpretation of ^{46}Ca Results

5.1.1 New State Spin-Parity Assignment

As the ^{46}Ca experimentally constructed level scheme in Figure 5.1(a) indicates, the new energy levels observed in this work were given tentative spin-parity assignments of (7^-), (8^-), and (9^-) for the 5689-, 6157-, and 6466-keV states. The conditions under which this new cascade was observed limit the possibilities of the spin and parity of the states among the cascade. All three gamma rays shown in Figure 4.7 required Doppler-correction in order to be identified and thus were emitted in flight, corresponding to fast ($\tau < 10$ ps) decays. For the 5689-keV state, the 2715-keV transition directly populates the 6^+_1 state, and other

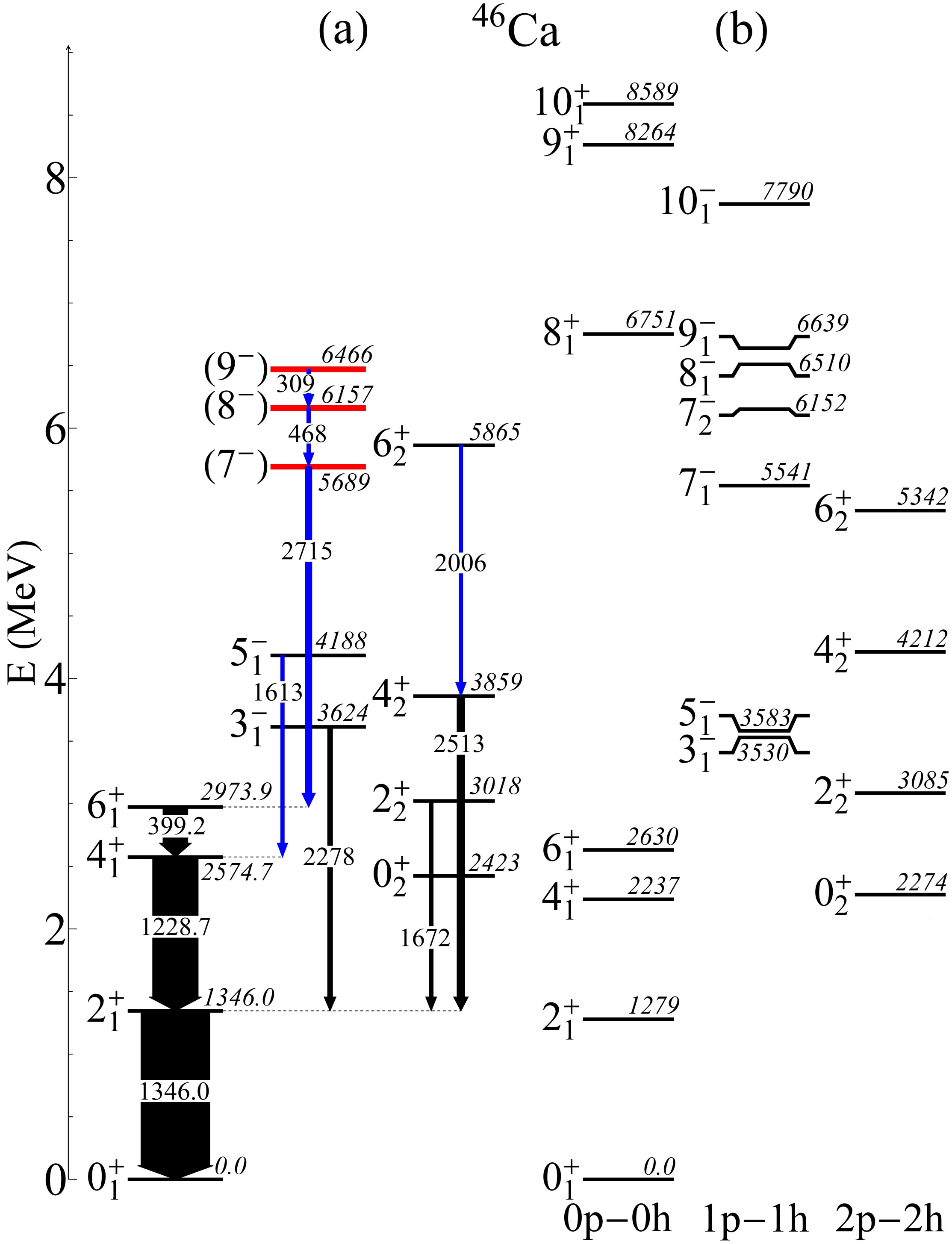

Figure 5.1: Experimental level scheme of ^{46}Ca (a) compared to results of $sd-pf-sdg$ shell model calculations (b). Excited states (gamma-ray transitions) newly identified from this work are shown in red (blue).

transitions to lower-spin ($J < 6$) states were not observed. This non-observation indicates a high spin value for the 5689-keV state, above $J = 6$, leaving the natural parity assignments of 7^- or 8^+. For the other two transitions, their relatively low energies and short limit on their lifetimes exclude the possibility of E2 or higher multipolarity. Assuming a conservative upper limit on their lifetime of 10 ps, transition strengths have corresponding lower limits of $B(E1) > 7.4 \cdot 10^{-4}$ W.u., $B(M1) > 0.031$ W.u., and $B(E2) > 371$ W.u. for the 468-keV decay and $B(E1) > 2.6 \cdot 10^{-3}$ W.u., $B(M1) > 0.11$ W.u., and $B(E2) > 2960$ W.u. for the 309-keV decay. According to recommended upper limits for the A=45-90 region [101], which are given as 0.01, 3, and 300 W.u. for E1, M1, and E2 respectively, the cascade decay should predominantly occur via either E1 or M1 transitions. These observations prompt two possible assignments: (9) → (8) → (7) or (10) → (9) → (8), which are discussed further in the following section.

5.1.2 Comparison with Shell Model Calculations

Figure 5.1(b) presents the result of the large-scale shell model calculation in the $sd-pf-sdg$ valence space including cross-shell excitations for negative-parity one-particle-one-hole (1p-1h) states as well as positive-parity 0p-0h and 2p-2h states, without mixing across configurations. The SDPF-MU interaction [102] with the modification found in Ref. [17] was used, which bases its single-particle energies and two-body matrix elements on the USD [103] and GXPF1B [104] interactions within the sd and pf shells, respectively. Interactions across shells are mediated by a monopole-based universal interaction, V_{MU} [105]. Electromagnetic strengths were calculated using effective charges $(e_p, e_n) = (1.5e, 0.5e)$ and effective $g_s' = 0.7g_s$ and $g_l' = 1.0g_l$ modified from bare g values.

The present calculations for the 0p-0h states shown in Figure 5.1(b) are essentially the same as the results from an fp-shell shell model calculation using the GXPF1A Hamiltonian. However, the predicted locations of the 8_1^+-10_1^+ states are much higher than the cascade of transitions newly observed in this work. The broad reliability of GXPF1A to accurately reproduce high-spin yrast level energies is well-established [106], so this discrepancy with the observed level spacing does not support a $10_1^+ \rightarrow 9_1^+ \rightarrow 8_1^+$ assignment, though it is not completely ruled out by the present data. If one looks at the results for the 1p-1h and 2p-2h excitations, the observed levels were more consistent with the $(9^-) \rightarrow (8^-) \rightarrow (7^-)$ cascade transition. In particular, the $8_1^- \rightarrow 7_2^-$ transition is predicted to have an M1 strength of $B(M1) = 0.57$ W.u., consistent with the experimental lower limit of 0.031 W.u.. The other $8_1^- \rightarrow 7_1^-$ transition is less likely to correspond because its predicted transition strength of 0.030 W.u. is close to the conservative lower limit. Similarly, the predicted strength of $B(M1) = 0.16$ W.u. for the $9_1^- \rightarrow 8_1^-$ transition is consistent with the experimental lower limit of 0.11 W.u. This suggests that the observed cascade corresponds to the $9_1^- \rightarrow 8_1^- \rightarrow 7_2^-$ shell model levels.

5.1.3 Collectivity in Calcium Isotopes

The behavior of the band-like structures illustrated in Figure 5 can be studied by comparisons to neighboring nuclei as well as with shell model calculations [107]. For the negative-parity band, the observed $(9^-) \rightarrow (8^-) \rightarrow (7^-)$ cascade in ^{46}Ca has a much smaller level spacing as compared to the $(7^-) \rightarrow 5^-$ energy difference, and does not follow the increasing $J(J+1)$ level spacing as observed for the rotational-like negative-parity band in ^{44}Ca (Figure 5.2). In the case of ^{44}Ca, strong E2 transitions are observed among the negative-parity states, whereas the 3_1^-, 5_1^-, and (7^-) states in ^{46}Ca appear to primarily decay by E1 transitions to the yrast band, suggesting a particle-hole character for these states. This view is also

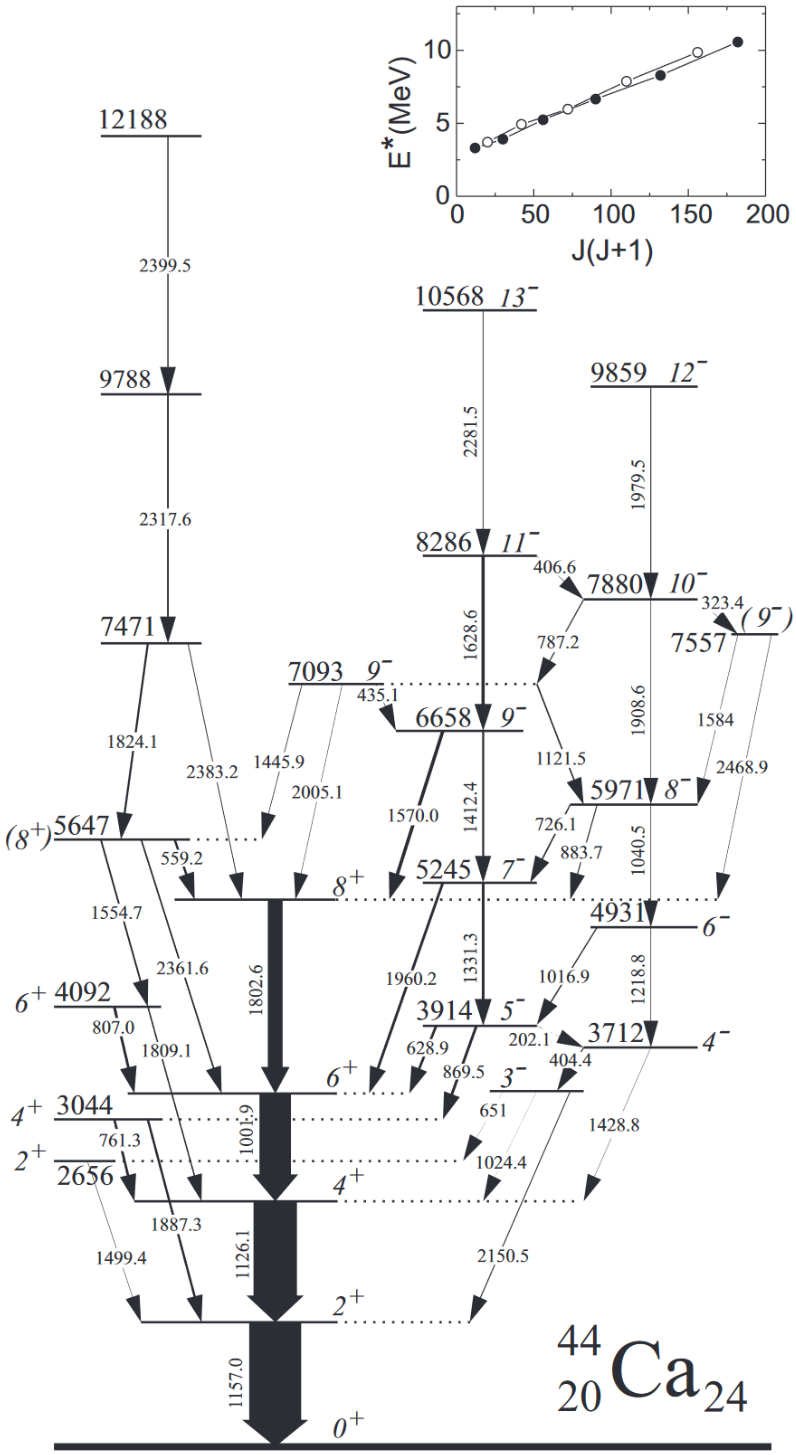

Figure 5.2: A level scheme showing band structures in ^{44}Ca, populated in the ^{30}Si(^{18}O,2p2n)^{44}Ca fusion-evaporation reaction. The inset shows excitation energy vs. angular momentum for negative parity states with odd-J (filled circles) and even-J (unfilled circles). The figure is from Ref. [28].

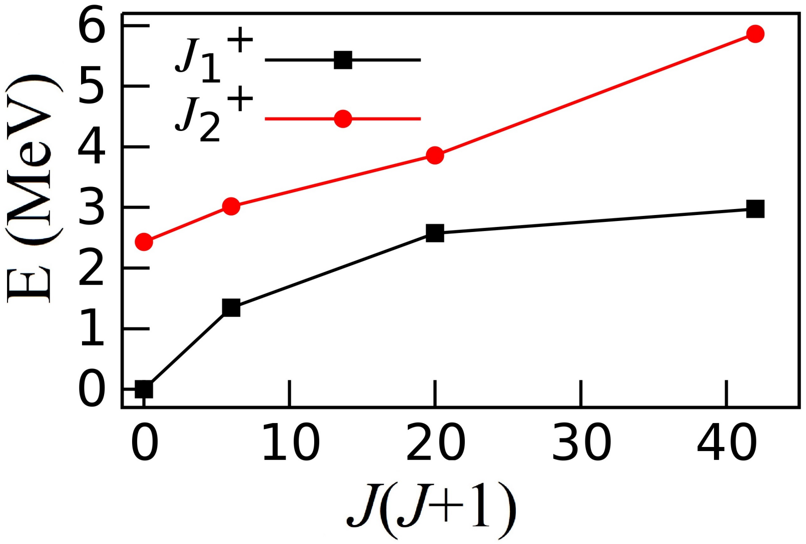

Figure 5.3: A plot showing excitation energy vs. angular momentum for the yrast J_1^+ (black) and yrare J_2^+ (red) bands observed in ^{46}Ca, populated in a lithium-induced reaction with a ^{45}K RI beam. The lines are meant to guide the eyes.

supported by the large gap between the 5_1^- and (7^-) states, which is comparable to that observed for the 0_{gs}^+ and other yrast levels, because 5_1^- can be formed as the $(d_{3/2}^{-1})(f_{7/2}^1)$ spin-stretched state coupled to 0_{gs}^+, whereas the (7^-) state requires core excitations.

On the other hand, it should be noted that the $(6_2^+) \rightarrow 4_2^+$ gamma transition energy was found to follow the $J(J+1)$ trend expected for a rotational band (Figure 5.3), confirming the deformed band structure on top of the 0_2^+ state. The shell model calculations show a somewhat compressed band structure; however, they predict large $B(E2)$ values within the yrare band (26.3, 35.2, and 32.0 W.u. for the 2_2^+, 4_2^+, and 6_2^+ decays, respectively), suggesting substantial collectivity. The present calculations also show dominant proton 2p-2h excitations in these yrare states. These results indicate the prevalence of shape coexistence in ^{46}Ca formed by the different particle-hole (0p-0h and 2p-2h) configurations, confirming the transition of 0_2^+ bands (suggested in Ref. [29]) from dominant 4p-4h (6p-4h) configurations in ^{40}Ca (^{42}Ca) to proton 2p-2h excitations.

5.2 Interpretation of ^{47}K Results

Neutron transfer offers a complementary approach to the compound reactions used to populate new states in ^{46}Ca. Reactions like fusion have been shown to effectively probe band structures in exotic neutron-rich nuclei when induced with rare-isotope (RI) beams; however, as more neutron-rich beams become available, the increasing tendency for neutron evaporation can limit how exotic the reaction products can reach into the neutron-rich regime. Neutron transfer provides a more selective alternative to probe low-lying states in nuclei more exotic than the RI beam itself with sensitivity to the single-particle nature of those states.

In this work, the $3/2^+$ first excited state of ^{47}K was populated by two-neutron transfer induced by the ^{45}K RI beam, and the differential cross section for this reaction was extracted. In the following subsections, the motivation for studying this reaction channel and the interpretation for the cross section are presented.

5.2.1 Intruder Configurations

The shell structure of the chain of odd-mass potassium (Z=19) isotopes is dominated by the single hole in the positive parity *sd* shell relative to magic calcium nuclei. Given the normal single particle levels according to the nuclear shell model, the hole state $\pi 1d^{-1}_{3/2}$ is expected to be the lowest energy configuration, producing a ground state spin-parity assignment of $3/2^+$. While this is true for the isotopic chain from ^{39}K to ^{45}K, the $1/2^+$ first excited state systematically lowers in energy until the two states become inverted in ^{47}K [108]

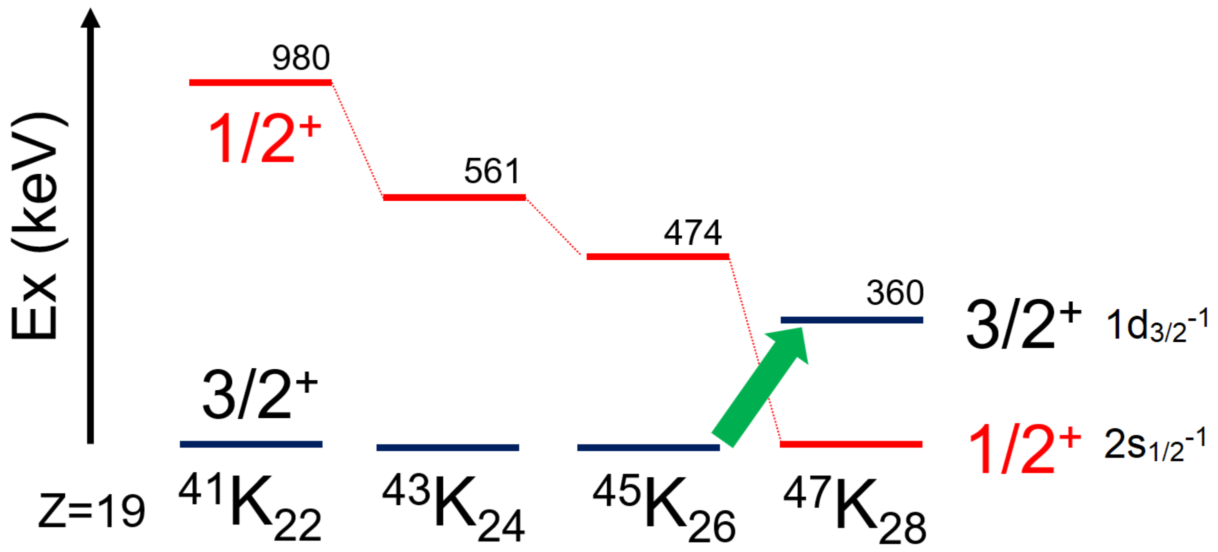

Figure 5.4: Systematics for odd-mass potassium isotopes for the ground and first excited state. The strength of population to the $3/2^+$ state in ^{47}K from two neutron transfer can inform studies of shell evolution.

(Figure 5.4), corresponding to a rapid decrease in the $\pi 1d_{3/2}$ single particle energy relative to $\pi 2s_{1/2}$. This is a prime example of an intruder configuration. Beyond ^{47}K, the intruder configuration continues in ^{49}K, but re-inverts back to a $3/2^+$ ground state in ^{51}K [109].

The explanation for this inversion of level energies is given by an isospin-dependent monopole residual interaction [110]. This interaction is produced by an attractive tensor force between protons with angular momentum $j = \ell \pm 1/2$ and neutrons with $j' = \ell' \mp 1/2$, and the magnitude increases as the j' orbit fills with more neutrons (Figure 5.5). For the odd-A potassium isotopes, these correspond to the occupation of the $\nu 1f_{7/2}$ creating a more tightly bound $\pi 1d_{5/2}$. This tensor force reaches its maximum once the $\nu 1f_{7/2}$ orbital is filled in ^{47}K, and by ^{51}K the dominant interaction is now the repulsive central force component of the monopole interactions between $\pi 2s_{1/2}$ and $\nu 2p_{3/2}$, since these orbits have the same number of nodes [109].

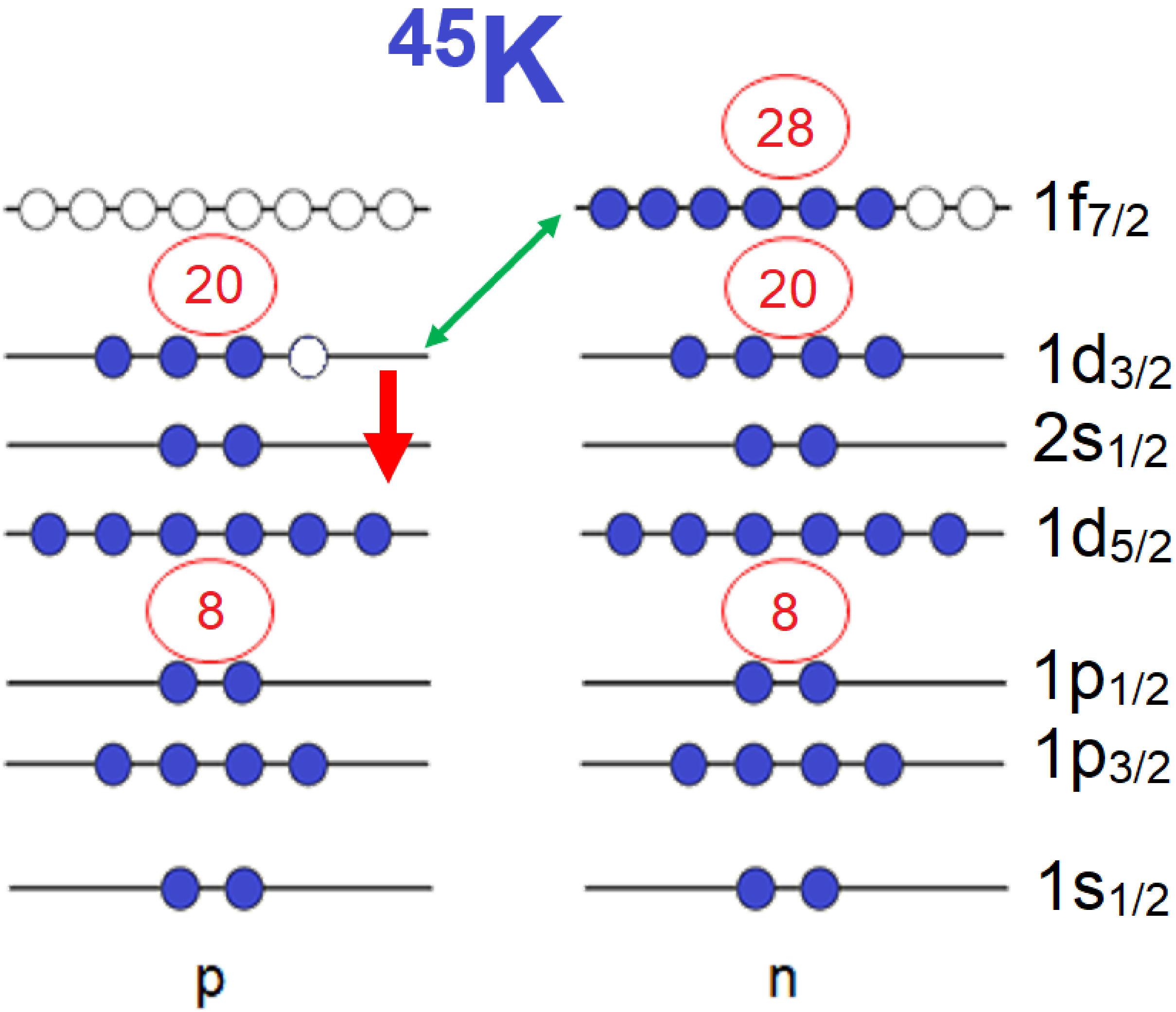

Figure 5.5: Shell model orbitals for ^{45}K in the normal configuration. A strong attractive tensor interaction between the $\pi 1d_{3/2}$ and $\nu 1f_{7/2}$ orbitals (shown with green arrow) increases in strength with increased number of neutrons in the $\nu 1f_{7/2}$, leading to an intruder configuration with a proton hole in $\pi 2s_{1/2}$ becoming the basis for a new ground state configuration in ^{47}K.

5.2.2 Fresco Calculations

In order to account for the ^{47}K cross section in Figure 4.12 and better understand the reaction process, data are compared to Coupled Reaction Channels (CRC) calculations for two-neutron transfer reactions. This allows the result to be related to the structural properties of potassium nuclei.

Fresco [111] is a CRC nuclear reactions code designed to treat several different reaction models under the same framework, including elastic scattering with optical model potentials, transfer reactions, and inelastic excitations to bound states or to the continuum. More information on the methods of the calculations and the relevant scattering theory can be found on Fresco's website [112].

In order to realistically describe nuclear reactions using Fresco, details about the initial and final states of nuclei in the reaction must be specified. Inputs include the excitation, spin, and parity of all involved nuclear states for each mass partition, as well as the masses, charges, and relative Q-values of the partitions. Depending on the reaction being modelled, wave functions for the relevant nuclei need to be described, often by specifying optical model potentials. One shape of optical model potential, the Woods-Saxon form, does a good job of reproducing measured cross sections for a large amount of data. The Woods-Saxon potential has the form

$$V(r) = \frac{V}{1 - e^{\frac{r - r_0 A^{1/3}}{a}}} \tag{5.1}$$

where V is the well depth, r_0 is the reduced radius ($R = r_0 A^{1/3}$ is the radius in fm), and a is the diffuseness parameter. This form has a real and imaginary component to account for inelastic channels, so there are a total of six free parameters. For one or two particle transfer, there must be defined one and two-nucleon wave functions between the transferred particles and the cores of the target and projectile nuclei. The equations for each mass partition have basis states which are generally non-orthogonal, except for simple cases which can be modelled with the Distorted Wave Born Approximation (DWBA) formalism. The model Schrödinger equation can be projected onto the different basis states, giving rise to a coupled set of equations where each nuclear wave function is an unknown. These are solved iteratively to find a differential cross section from S-matrix elements [113]. It should be noted for particle transfer that the couplings between mass partitions include non-local couplings that are generally dealt with using perturbations to allow the numerical solutions to converge.

There are many ways to go about modelling two-nucleon transfer with Fresco. For this analysis, the procedure of D. Chattopadhyay et al. [114] was used as a reference. Their study of ^{7}Li transfer-breakup channels with a ^{112}Sn target was used to confirm that the methodology of this work is consistent with a previously successful approach.

The ^{112}Sn(^{7}Li,^{5}Li)^{114}Sn reaction channel at 30 MeV modelled in Ref. [114] is reproduced in Figure 5.6. For this calculation, an entrance channel optical potential was determined from a fit to data for ^{112}Sn+^{7}Li elastic scattering measured in the same experiment. For the exit channel (^{114}Sn+^{5}Li), the same potential parameters were used, but a Woods-Saxon square form was employed. The 0_1^+ ground state and the 1300 keV 2_1^+ state of ^{114}Sn were included in the outgoing mass partition, along with the unbound ground state of ^{5}Li. These states were chosen based on Q-value calculations, following the procedure of Ref. [115], which distinguished different excitation channels by using the energies of the projectile fragments (α and proton). The Direct one-step stripping of a dineutron was the only process included in the result, because the same Q-value calculation did not show any signs of intermediate states. The spectroscopic amplitudes $\langle {}^{7}\mathrm{Li}|{}^{5}\mathrm{Li} + 2n\rangle$ and $\langle {}^{114}\mathrm{Sn}|{}^{112}\mathrm{Sn} + 2n\rangle$ were taken to

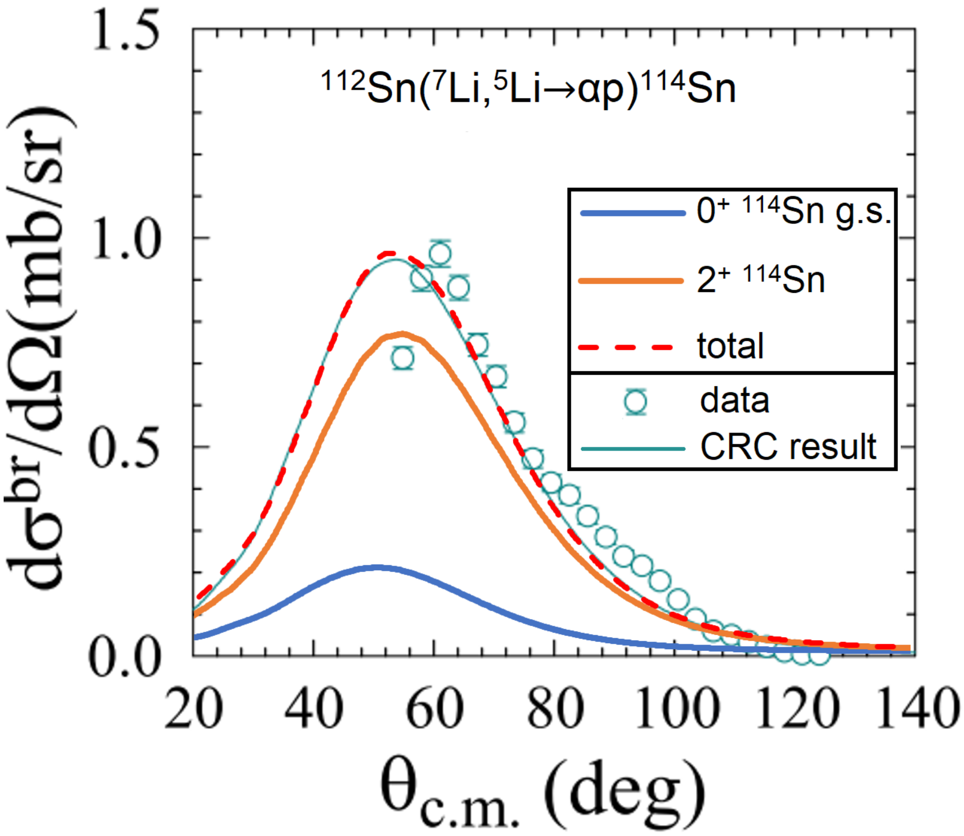

Figure 5.6: Diferential cross section for the ^{112}Sn(^{7}Li,^{5}Li)^{114}Sn reactions channel for a 30 MeV ^{7}Li beam energy. Two states in ^{114}Sn and the ^{5}Li (unbound) ground state were included. The cross section calculated in this work (shown in red) is nearly identical to the calculations (shown in green curve) from Ref. [114].

be 1.0. In the Fresco calculation performed for this work that reproduced the tin CRC reference (Figure 5.6), potentials between the dineutron and the ^{112}Sn and ^{5}Li cores were tuned to match the binding energies of the relevant bound states, and the core-core potential used for a finite-range transfer coupling was kept the same as the entrance channel. These details are summarized in the Fresco input file found in the Appendix.

For this work, the ^{7}Li(^{45}K,^{47}K)^{5}Li two-neutron transfer reaction was modelled, and the same essential procedure was followed. The subsequent breakup of ^{5}Li into an alpha and proton pair was treated as an independent decay, just as in the reference calculation. The calculation was performed in forward rather than inverse kinematics by converting the lab frame beam energy. An important factor in this calculation is the optical model potential. Ultimately optical model parameters from Ref. [116], obtained from the measurement of ^{40}Ca+^{7}Li elastic scattering at 20 MeV, were chosen due to the similarity in the nuclei and the lab frame energy (E_{lab} = 20 MeV or 2.85 MeV/u for ^{7}Li, consistent with a mid-target ^{45}K beam energy from this work). The optical-potential parameters were $(V, r_V, a_V) = (173.0, 1.00, 0.62)$ for the real component and $(W, r_W, a_W) = (20.7, 1.08, 0.97)$ for the imaginary component. As in the reference calculation, the exit channel was changed to the Woods-Saxon square form (i.e. the denominator of Equation 5.1 is squared). For the exit channel, the unbound ground state of ^{5}Li and the $3/2^{+}$ first excited state of ^{47}K were included, since that is the only state in ^{47}K that was observed to gamma decay. Direct dineutron stripping was the only process considered in the calculation. A procedure to calculate the Q values could have been possible with a thinner target; however, given the beam energy loss in the target, the energy of the recoil could not be reconstructed with high enough precision to distinguish excited states in ^{5}Li, potential feeding in ^{47}K, or any intermediate processes.

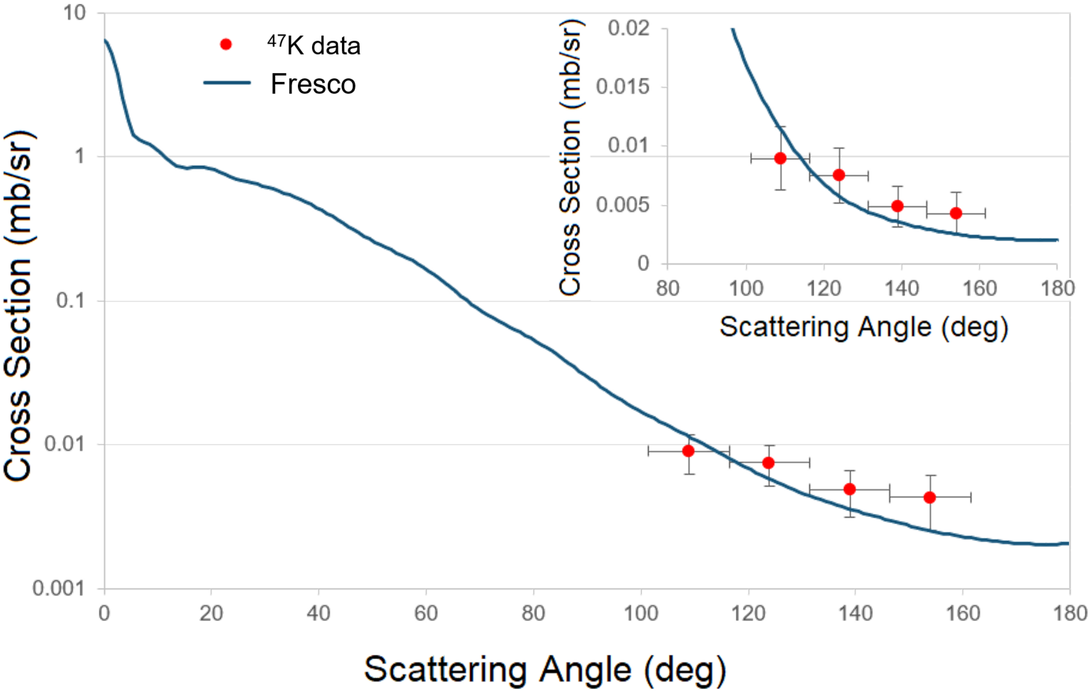

Figure 5.7: Comparison of differential cross section for ^{47}K to Fresco calculation, after accounting for beam energy loss in the target. Agreement is good when using a single-step process and a similar procedure described in Ref. [114], as well as in the text of this section. The result shown uses spectroscopic amplitude of 1.0, and indicates a much higher cross section for forward angles, corresponding to upstream of the target in the laboratory frame.

The result of the Fresco calculation for two-neutron transfer is compared to data in Figure 5.7. The calculation has been averaged over different energies to account for the significant energy loss in the target and the angular resolution of the silicon detector. The spectroscopic amplitude remained 1.0 for this calculation. This is consistent with the shell model picture, where the ^{45}K $3/2^-_1$ ground state and the ^{45}K $3/2^-_1$ first excited state should be dominated by $\pi d^{-1}_{3/2}$ configurations. Both the magnitude and the trend in the differential cross section is in full agreement with the data. The calculation would imply much larger cross sections can be found at lower center-of-mass angles, which correspond to upstream of the target in the laboratory frame. This is consistent with general observations of similar reaction channels like (t,p). In the future, with a detector placement optimized for direct transfer rather than (or in addition to) compound reaction products, one could expect much greater yields with the same target and beam intensity. With the improved detector coverage, another option would be to use a much thinner target, allowing the experiment to probe for intermediate states while maintaining current yields.

As FRIB comes online with higher beam intensities for neutron-rich beams, new opportunities for using this reaction mechanism will open up. For instance, a similar two-neutron transfer reaction from ^{49}K ($1/2^+$ g.s.) to ^{51}K ($3/2^+$ g.s.) would be expected to have strong population to the $1/2^+$ first excited state in ^{51}K for the same reason that the reaction in this work strongly populated the $3/2^+$ first excited state in ^{47}K. Observation of the first excited state energy would be very informative for learning the magnitudes of the different components in the monopole interaction and greatly improve existing effective interactions, as seen in Figure 5.8.

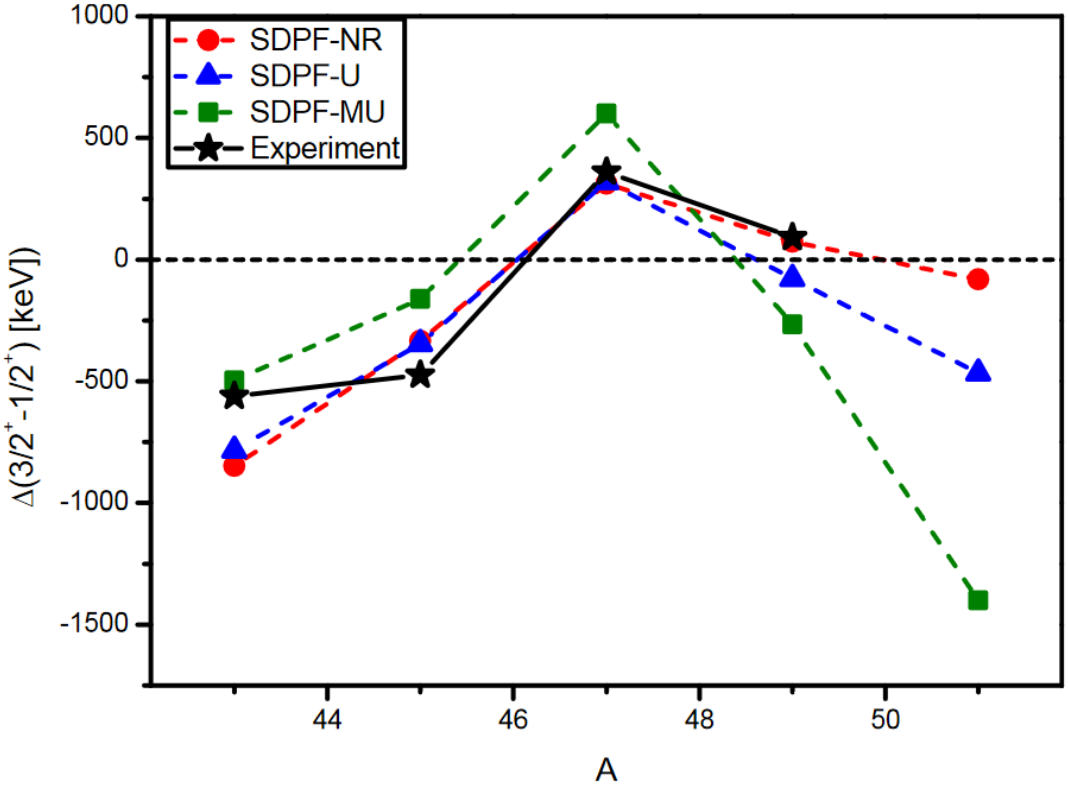

Figure 5.8: Energy level differences in odd-A potassium isotopes between the $3/2^+$ and $1/2^+$ states, compared to the results of shell model calculations. The re-inversion of states from ^{49}K to ^{51}K presents an analogous case to this work, implying that two-neutron transfer could be effective at discovering the location of the $1/2^+$ state in ^{51}K. This experimental result would be very selective for the divergent predictions from the effective Hamiltonians (including [102]). The figure is adapted from Ref. [117].

Chapter 6

Summary and Outlook

The success of this experiment demonstrated the usefulness of reaccelerated rare isotope (RI) beams to access unexplored states in the neutron-rich regime with gamma-ray spectroscopy. The reaccelerated beam facility ReA3 at the National Superconducting Cyclotron Laboratory (NSCL) produced a high-intensity ^{45}K rare-isotope beam which, in addition to a ^{40}Ar stable beam, reacted with a natural lithium target to populate excited states in residues from a variety of Coulomb-barrier energy reaction mechanisms, including direct two-neutron transfer and fusion-evaporation. The Segmented Germanium Array and an annular silicon detector measured gamma-ray and charged-particle interactions to identify transitions and distinguish reaction channels. The versatility of this approach with regard to reaction mechanism was amplified by the use of a 5.8 mg/cm^2-thick target, producing significantly high yields despite relatively low beam intensity. With careful implementation of the setup and methodology introduced in this work, future RI beam experiments will be able to probe deeper than before into the structure of exotic nuclei, especially with newly developed neutron-rich beams available at FRIB.

This work successfully uncovered the existence of three independent band structures in ^{46}Ca which inform the underlying particle-hole excitations characterized by shell structure. Three new states and five new transitions were observed in ^{46}Ca. Together with the consistency with the large-scale shell model calculations, the present results suggest the persistence of shape coexistence in ^{46}Ca due to the competition between established shell structure and particle-hole excitations. The band structure observed for the 0_2^+ state in ^{46}Ca was shown to be consistent with two-particle-two-hole (2p-2h) excitations. This result confirms the long-suspected systematic evolution from dominant 4p-4h (6p-4h) configurations for the 0_2^+ bands of ^{40}Ca (^{42}Ca) to proton cross-shell excitations for the 0_2^+ band of ^{46}Ca. This work opens the way for further investigation into more neutron-rich Ca isotopes away from stability, where new magicity has recently been identified.

A complementary technique of direct neutron transfer proved advantageous to populate low-lying states in neutron-rich nuclei. Differential cross sections were extracted for ^{46,47}K from gamma-ray intensities and compared to CRC calculations. The results confirm the migration of intruder configurations in odd-mass neutron-rich potassium isotopes. Given the successful development of the present work, both direct and compound nucleus reactions can be used simultaneously to explore the single-particle and collective properties of exotic nuclei far from stability.

In conclusion, reaccelerated RI beams and gamma-ray spectroscopy proved a potent combination to explore the evolution of nuclear structure in previously inaccessible nuclei.

APPENDIX

APPENDIX

Fresco Input Files

```
sn112(li7,li5)sn114 @ 30 MeV;
NAMELIST
 &FRESCO hcm=0.03 rmatch=40 rintp=0.20 hnl=0.1 rnl=5.00 centre=0.0
   jtmin=0.0  jtmax=50 absend=-1.0
   thmin=0.00 thmax=180.00 thinc=0.10
   iter=1 nnu=36
   chans=1 xstabl=1
   elab=30.0  /

 &PARTITION namep='li7'  massp=7. zp=3 namet='sn112'  masst=112. zt=50 nex=1  /
 &STATES jp=1.5 bandp=-1 ep=0.0 cpot=1 jt=0.0 bandt=1 et=0.0000  /

 &PARTITION namep='li5' massp=5. zp=3 namet='sn114'  masst=114. zt=50 qval=5.13 nex=2  /
 &STATES jp=1.5 bandp=-1 ep=0.0  cpot=2 jt=0. bandt=1 et=0.0000  /
 &STATES jt=2. bandt=1 et=1.2999  /
 &partition /

 &POT kp=1 ap=7.000 at=112.000 rc=1.278  /
 &POT kp=1 type=1 p1=25.33 p2=1.185 p3=0.75  p4=25.38 p5=1.17 p6=0.787  /

 &POT kp=2 ap=5.000 at=114.000 rc=1.278  /
 &POT kp=2 type=1 shape=1 p1=25.33 p2=1.185 p3=0.75 p4=25.38 p5=1.17 p6=0.787  /
```

```

&POT kp=3 at=7 rc=1.278  /
&POT kp=3 type=1 p1=50.00 p2=1.2 p3=0.65   /
&POT kp=3 type=3 p1=6.00  p2=1.2 p3=0.65   /

&POT kp=4 at=114 rc=0.951  /
&POT kp=4 type=1 p1=50.00 p2=1.2 p3=0.65   /
&POT kp=4 type=3 p1=6.00  p2=1.2 p3=0.65   /

&POT kp=5 ap=7.000 at=112.000 rc=1.278  /
&POT kp=5 type=1 p1=25.33 p2=1.185 p3=0.75  p4=25.38 p5=1.17 p6=0.787  /
&pot /

&Overlap kn1=1 ic1=2 ic2=1 in=1 kind=0 nn=2 l=0 sn=0.0 j=0 kbpot=3 be
   =12.910  isc=1 ipc=0 /
&Overlap kn1=2 ic1=1 ic2=2 in=2 kind=0 nn=4 l=0 sn=0.0 j=0 kbpot=4 be
   =18.0473 isc=1 ipc=0 /
&Overlap kn1=3 ic1=1 ic2=2 in=2 kind=0 nn=3 l=2 sn=0.0 j=2 kbpot=4 be
   =16.7474 isc=1 ipc=0 /
&overlap /

&Coupling icto=-2 icfrom=1 kind=7 ip1=0 ip2=-1 ip3=5 /
&CFP in=1 ib=1 ia=1 kn=1 a=1.00  /
&CFP in=2 ib=1 ia=1 kn=2 a=1.00  /
&CFP in=2 ib=2 ia=1 kn=3 a=1.00  /
&CFP /
&coupling /
```

```
k45(li7,li5)k47 @ 32.66 MeV  energies over target:31.205 29.772 28.305 26.802 25.259 23.673 22.039 20.353 18.609 16.801 14.912;
NAMELIST
 &FRESCO hcm=0.03 rmatch=40 rintp=0.20 hnl=0.1 rnl=5.00 centre=0.0
   jtmin=0.0  jtmax=50 absend=-1.0
   thmin=0.00 thmax=180.00 thinc=1.00
   iter=1 nnu=36
   chans=1 xstabl=1
   elab=31.205 /

 &PARTITION namep='li7'  massp=7. zp=3 namet='k45'  masst=45. zt=19 nex=1 /
 &STATES jp=1.5 bandp=-1 ep=0.0 cpot=1 jt=1.5 bandt=1 et=0.0000  /

 &PARTITION namep='li5' massp=5. zp=3 namet='k47'  masst=47. zt=19 qval=2.32 nex=1  /
 &STATES jp=1.5 bandp=-1 ep=0.0  cpot=2 jt=1.5 bandt=1 et=0.36  /
 &partition /

 &POT kp=1 ap=7.000 at=45.000 rc=1.278  /
 &POT kp=1 type=1 p1=173.0 p2=1.00 p3=0.62 p4=20.7 p5=1.08 p6=0.97  /

 &POT kp=2 ap=5.000 at=47.000 rc=1.278  /
 &POT kp=2 type=1 shape=1 p1=173.0 p2=1.00 p3=0.62 p4=20.7 p5=1.08 p6=0.97 /

 &POT kp=3 at=7 rc=1.278  /
 &POT kp=3 type=1 p1=50.00 p2=1.2 p3=0.65   /
```

```
&POT kp=3 type=3 p1=6.00  p2=1.2 p3=0.65   /

&POT kp=4 at=47 rc=0.957  /
&POT kp=4 type=1 p1=50.00 p2=1.2 p3=0.65   /
&POT kp=4 type=3 p1=6.00  p2=1.2 p3=0.65   /

&POT kp=5 ap=7.000 at=45.000 rc=1.278  /
&POT kp=5 type=1 p1=173.0 p2=1.00 p3=0.62 p4=20.7 p5=1.08 p6=0.97  /
&pot /

&Overlap kn1=1 ic1=2 ic2=1 in=1 kind=0 nn=2 l=0 sn=0.0 j=0 kbpot=3 be=12.910  isc=1 ipc=0 /
&Overlap kn1=2 ic1=1 ic2=2 in=2 kind=0 nn=3 l=0 sn=0.0 j=0 kbpot=4 be=14.879 isc=1 ipc=0 /
&overlap /

&Coupling icto=-2 icfrom=1 kind=7 ip1=0 ip2=-1 ip3=5 /
&CFP in=1 ib=1 ia=1 kn=1 a=1.00  /
&CFP in=2 ib=1 ia=1 kn=2 a=0.84823  /
&CFP /
&coupling /
```

BIBLIOGRAPHY

BIBLIOGRAPHY

[1] S. M. Mc.Daniel. Ph.d. thesis. Michigan State University, 2011.

[2] E. Simpson. The colorful nuclear chart. `https://people.physics.anu.edu.au/~ecs103/chart/`. Accessed: November 23, 2021.

[3] R F Casten. *Nuclear Structure from a Simple Perspective; 1st ed.* Oxford Univ. Press, New York, NY, 1990.

[4] B. A. Brown. Lecture notes in nuclear structure physics (michigan state university). Michigan State University, 2018.

[5] Maria Goeppert Mayer. *Phys. Rev.*, 75:1969–1970, Jun 1949.

[6] Wojciech Satula and Ramon Wyss. *Reports on Progress in Physics*, 68:131, 11 2004.

[7] E. M. Henley and J. P. Schiffer. *Rev. Mod. Phys.*, 71:S205–S219, Mar 1999.

[8] P. J. Twin, B. M. Nyakó, A. H. Nelson, J. Simpson, M. A. Bentley, H. W. Cranmer-Gordon, P. D. Forsyth, D. Howe, A. R. Mokhtar, J. D. Morrison, J. F. Sharpey-Schafer, and G. Sletten. *Phys. Rev. Lett.*, 57:811–814, Aug 1986.

[9] A. Galindo-Uribarri, H. R. Andrews, G. C. Ball, T. E. Drake, V. P. Janzen, J. A. Kuehner, S. M. Mullins, L. Persson, D. Prévost, D. C. Radford, J. C. Waddington, D. Ward, and R. Wyss. *Phys. Rev. Lett.*, 71:231–234, Jul 1993.

[10] D. R. LaFosse, D. G. Sarantites, C. Baktash, P.-F. Hua, B. Cederwall, P. Fallon, C. J. Gross, H.-Q. Jin, M. Korolija, I. Y. Lee, A. O. Macchiavelli, M. R. Maier, W. Rathbun, D. W. Stracener, and T. R. Werner. *Phys. Rev. Lett.*, 74:5186–5189, Jun 1995.

[11] A. Krasznahorkay, M. Hunyadi, M. N. Harakeh, M. Csatlós, T. Faestermann, A. Gollwitzer, G. Graw, J. Gulyás, D. Habs, R. Hertenberger, H. J. Maier, Z. Máté, D. Rudolph, P. Thirolf, J. Timár, and B. D. Valnion. *Phys. Rev. Lett.*, 80:2073–2076, Mar 1998.

[12] G. Hagen, M. Hjorth-Jensen, G. R. Jansen, R. Machleidt, and T. Papenbrock. *Phys. Rev. Lett.*, 109:032502, Jul 2012.

[13] Jochen Erler, Noah Birge, Markus Kortelainen, Witold Nazarewicz, Erik Olsen, Alexander M. Perhac, and Mario Stoitsov. *Nature*, 486(7404):509–512, 2012.

[14] O. B. Tarasov, D. S. Ahn, D. Bazin, N. Fukuda, A. Gade, M. Hausmann, N. Inabe, S. Ishikawa, N. Iwasa, K. Kawata, T. Komatsubara, T. Kubo, K. Kusaka, D. J. Morrissey, M. Ohtake, H. Otsu, M. Portillo, T. Sakakibara, H. Sakurai, H. Sato, B. M. Sherrill, Y. Shimizu, A. Stolz, T. Sumikama, H. Suzuki, H. Takeda, M. Thoennessen, H. Ueno, Y. Yanagisawa, and K. Yoshida. *Phys. Rev. Lett.*, 121:022501, Jul 2018.

[15] A. Huck, G. Klotz, A. Knipper, C. Miehé, C. Richard-Serre, G. Walter, A. Poves, H. L. Ravn, and G. Marguier. *Phys. Rev. C*, 31:2226–2237, Jun 1985.

[16] A. Gade, R. V. F. Janssens, D. Bazin, R. Broda, B. A. Brown, C. M. Campbell, M. P. Carpenter, J. M. Cook, A. N. Deacon, D.-C. Dinca, B. Fornal, S. J. Freeman, T. Glasmacher, P. G. Hansen, B. P. Kay, P. F. Mantica, W. F. Mueller, J. R. Terry, J. A. Tostevin, and S. Zhu. *Phys. Rev. C*, 74:021302(R), Aug 2006.

[17] D. Steppenbeck, S. Takeuchi, N. Aoi, P. Doornenbal, M. Matsushita, H. Wang, H. Baba, N. Fukuda, S. Go, M. Honma, J. Lee, K. Matsui, S. Michimasa, T. Motobayashi, D. Nishimura, T. Otsuka, H. Sakurai, Y. Shiga, P.-A. Söderström, T. Sumikama, H. Suzuki, R. Taniuchi, Y. Utsuno, J. J. Valiente-Dobón, and K. Yoneda. *Nature*, 502(7470):207–210, 2013.

[18] F. Wienholtz, D. Beck, K. Blaum, Ch Borgmann, M. Breitenfeldt, R. B. Cakirli, S. George, F. Herfurth, J. D. Holt, M. Kowalska, S. Kreim, D. Lunney, V. Manea, J. Menéndez, D. Neidherr, M. Rosenbusch, L. Schweikhard, A. Schwenk, J. Simonis, J. Stanja, R. N. Wolf, and K. Zuber. *Nature*, 498(7454):346–349, 2013.

[19] S. Michimasa, M. Kobayashi, Y. Kiyokawa, S. Ota, D. S. Ahn, H. Baba, G. P. A. Berg, M. Dozono, N. Fukuda, T. Furuno, E. Ideguchi, N. Inabe, T. Kawabata, S. Kawase, K. Kisamori, K. Kobayashi, T. Kubo, Y. Kubota, C. S. Lee, M. Matsushita, H. Miya, A. Mizukami, H. Nagakura, D. Nishimura, H. Oikawa, H. Sakai, Y. Shimizu, A. Stolz, H. Suzuki, M. Takaki, H. Takeda, S. Takeuchi, H. Tokieda, T. Uesaka, K. Yako, Y. Yamaguchi, Y. Yanagisawa, R. Yokoyama, K. Yoshida, and S. Shimoura. *Phys. Rev. Lett.*, 121:022506, Jul 2018.

[20] R. F. Garcia Ruiz, M. L. Bissell, K. Blaum, A. Ekström, N. Frömmgen, G. Hagen, M. Hammen, K. Hebeler, J. D. Holt, G. R. Jansen, M. Kowalska, K. Kreim, W. Nazarewicz, R. Neugart, G. Neyens, W. Nörtershäuser, T. Papenbrock, J. Papuga, A. Schwenk, J. Simonis, K. A. Wendt, and D. T. Yordanov. *Nature Physics*, 12(6):594–598, 2016.

[21] A. J. Miller, K. Minamisono, A. Klose, D. Garand, C. Kujawa, J. D. Lantis, Y. Liu, B. Maaß, P. F. Mantica, W. Nazarewicz, W. Nörtershäuser, S. V. Pineda, P.-G. Reinhard, D. M. Rossi, F. Sommer, C. Sumithrarachchi, A. Teigelhöfer, and J. Watkins. *Nature Physics*, 15(5):432–436, 2019.

[22] E. Ideguchi, D. G. Sarantites, W. Reviol, A. V. Afanasjev, M. Devlin, C. Baktash, R. V. F. Janssens, D. Rudolph, A. Axelsson, M. P. Carpenter, A. Galindo-Uribarri, D. R. LaFosse, T. Lauritsen, F. Lerma, C. J. Lister, P. Reiter, D. Seweryniak, M. Weiszflog, and J. N. Wilson. *Phys. Rev. Lett.*, 87:222501, Nov 2001.

[23] G D Dracoulis, A P Byrne, T Kibédi, T R McGoram, and S M Mullins. *Journal of Physics G: Nuclear and Particle Physics*, 23(10):1191–1202, oct 1997.

[24] J. J. Valiente-Dobón, S. M. Lenzi, S. J. Freeman, S. Lunardi, J. F. Smith, A. Gottardo, F. DellaVedova, E. Farnea, A. Gadea, D. R. Napoli, M. Axiotis, S. Aydin, D. Bazzacco, P. G. Bizzeti, A. M. Bizzeti-Sona, G. Benzoni, D. Bucurescu, L. Corradi, A. N. Deacon, G. de Angelis, E. Fioretto, B. Guiot, M. Ionescu-Bujor, A. Iordachescu, S. Leoni, N. Marginean, R. Marginean, P. Mason, R. Menegazzo, D. Mengoni, B. Million, G. Montagnoli, R. Orlandi, F. Recchia, E. Sahin, F. Scarlassara, R. P. Singh, A. M. Stefanini, D. Steppenbeck, S. Szilner, C. A. Ur, B. J. Varley, and O. Wieland. *Phys. Rev. C*, 78:024302, Aug 2008.

[25] S. Zhu, R. V. F. Janssens, B. Fornal, S. J. Freeman, M. Honma, R. Broda, M. P. Carpenter, A. N. Deacon, E. Jackson, B. P. Kay, T. Lauritsen, C. J. Lister, P. F. Mantica, T. Otsuka, D. Seweryniak, J. F. Smith, D. Steppenbeck, and X. Wang. *Phys. Rev. C*, 80:024318, Aug 2009.

[26] S. Bottoni, S. Leoni, B. Fornal, R. Raabe, K. Rusek, G. Benzoni, A. Bracco, F. C. L. Crespi, A. I. Morales, P. Bednarczyk, N. Cieplicka-Oryńczak, W. Królas, A. Maj, B. Szpak, M. Callens, J. Bouma, J. Elseviers, H. De Witte, F. Flavigny, R. Orlandi, P. Reiter, M. Seidlitz, N. Warr, B. Siebeck, S. Hellgartner, D. Mücher, J. Pakarinen, M. Vermeulen, C. Bauer, G. Georgiev, R. V. F. Janssens, D. Balabanski, M. Sferrazza, M. Kowalska, E. Rapisarda, D. Voulot, M. Lozano Benito, and F. Wenander. *Phys. Rev. C*, 92:024322, Aug 2015.

[27] K. Hadyńska-Klęk, P. J. Napiorkowski, M. Zielińska, J. Srebrny, A. Maj, F. Azaiez, J. J. Valiente Dobón, M. Kici ńska Habior, F. Nowacki, H. Naïdja, B. Bounthong, T. R. Rodríguez, G. de Angelis, T. Abraham, G. Anil Kumar, D. Bazzacco, M. Bellato, D. Bortolato, P. Bednarczyk, G. Benzoni, L. Berti, B. Birkenbach, B. Bruyneel, S. Brambilla, F. Camera, J. Chavas, B. Cederwall, L. Charles, M. Ciemała, P. Cocconi, P. Coleman-Smith, A. Colombo, A. Corsi, F. C. L. Crespi, D. M. Cullen, A. Czermak, P. Désesquelles, D. T. Doherty, B. Dulny, J. Eberth, E. Farnea, B. Fornal, S. Franchoo, A. Gadea, A. Giaz, A. Gottardo, X. Grave, J. Grębosz, A. Görgen, M. Gulmini,

T. Habermann, H. Hess, R. Isocrate, J. Iwanicki, G. Jaworski, D. S. Judson, A. Jungclaus, N. Karkour, M. Kmiecik, D. Karpiński, M. Kisieliński, N. Kondratyev, A. Korichi, M. Komorowska, M. Kowalczyk, W. Korten, M. Krzysiek, G. Lehaut, S. Leoni, J. Ljungvall, A. Lopez-Martens, S. Lunardi, G. Maron, K. Mazurek, R. Menegazzo, D. Mengoni, E. Merchán, W. Męczyński, C. Michelagnoli, J. Mierzejewski, B. Million, S. Myalski, D. R. Napoli, R. Nicolini, M. Niikura, A. Obertelli, S. F. Özmen, M. Palacz, L. Próchniak, A. Pullia, B. Quintana, G. Rampazzo, F. Recchia, N. Redon, P. Reiter, D. Rosso, K. Rusek, E. Sahin, M.-D. Salsac, P.-A. Söderström, I. Stefan, O. Stézowski, J. Styczeń, Ch. Theisen, N. Toniolo, C. A. Ur, V. Vandone, R. Wadsworth, B. Wasilewska, A. Wiens, J. L. Wood, K. Wrzosek-Lipska, and M. Zięblinski. *Phys. Rev. Lett.*, 117:062501, Aug 2016.

[28] M. Lach, P. Bednarczyk, A. Bracco, J. Grebosz, M. Kadluczka, N. Kintz, A. Maj, J. C. Merdinger, W. Meczynski, J. L. Pedroza, N. Schulz, M. B. Smith, K. M. Spohr, J. Styczen, J. P. Vivien, and M. Zieblinski. *The European Physical Journal A - Hadrons and Nuclei*, 12(4):381–382, 2001.

[29] J.L Wood, K Heyde, W Nazarewicz, M Huyse, and P van Duppen. *Physics Reports*, 215(3):101 – 201, 1992.

[30] B. A. Brown. *Physics*, 3:104, 2010.

[31] R. Taniuchi, C. Santamaria, P. Doornenbal, A. Obertelli, K. Yoneda, G. Authelet, H. Baba, D. Calvet, F. Château, A. Corsi, A. Delbart, J.-M. Gheller, A. Gillibert, J. D. Holt, T. Isobe, V. Lapoux, M. Matsushita, J. Menéndez, S. Momiyama, T. Motobayashi, M. Niikura, F. Nowacki, K. Ogata, H. Otsu, T. Otsuka, C. Péron, S. Péru, A. Peyaud, E. C. Pollacco, A. Poves, J.-Y. Roussé, H. Sakurai, A. Schwenk, Y. Shiga, J. Simonis, S. R. Stroberg, S. Takeuchi, Y. Tsunoda, T. Uesaka, H. Wang, F. Browne, L. X. Chung, Z. Dombradi, S. Franchoo, F. Giacoppo, A. Gottardo, K. Hadyńska-Klęk, Z. Korkulu, S. Koyama, Y. Kubota, J. Lee, M. Lettmann, C. Louchart, R. Lozeva, K. Matsui, T. Miyazaki, S. Nishimura, L. Olivier, S. Ota, Z. Patel, E. Şahin, C. Shand, P.-A. Söderström, I. Stefan, D. Steppenbeck, T. Sumikama, D. Suzuki, Z. Vajta, V. Werner, J. Wu, and Z. Y. Xu. *Nature*, 569(7754):53–58, May 2019.

[32] F. Nowacki, A. Poves, E. Caurier, and B. Bounthong. *Phys. Rev. Lett.*, 117:272501, Dec 2016.

[33] Y. Iwata, N. Shimizu, T. Otsuka, Y. Utsuno, J. Menéndez, M. Honma, and T. Abe. *Phys. Rev. Lett.*, 116:112502, Mar 2016.

[34] Tomás R. Rodríguez and J. Luis Egido. *Phys. Rev. Lett.*, 99:062501, Aug 2007.

[35] L. Coraggio, A. Covello, A. Gargano, and N. Itaco. *Phys. Rev. C*, 80:044311, Oct 2009.

[36] J.H. Bjerregaard, Ole Hansen, O. Nathan, R. Chapman, S. Hinds, and R. Middleton. *Nuclear Physics A*, 103(1):33 – 70, 1967.

[37] G. M. Crawley, P. S. Miller, G. J. Igo, and J. Kulleck. *Phys. Rev. C*, 8:574–580, Aug 1973.

[38] W. W. Daehnick and M. J. Spisak. *Phys. Rev. C*, 7:2593–2596, Jun 1973.

[39] D. Montanari, S. Leoni, D. Mengoni, J. J. Valiente-Dobon, G. Benzoni, N. Blasi, G. Bocchi, P. F. Bortignon, S. Bottoni, A. Bracco, F. Camera, P. Casati, G. Colò, A. Corsi, F. C. L. Crespi, B. Million, R. Nicolini, O. Wieland, D. Bazzacco, E. Farnea, G. Germogli, A. Gottardo, S. M. Lenzi, S. Lunardi, R. Menegazzo, G. Montagnoli, F. Recchia, F. Scarlassara, C. Ur, L. Corradi, G. de Angelis, E. Fioretto, D. R. Napoli, R. Orlandi, E. Sahin, A. M. Stefanini, R. P. Singh, A. Gadea, S. Szilner, M. Kmiecik, A. Maj, W. Meczynski, A. Dewald, Th. Pissulla, and G. Pollarolo. *Phys. Rev. C*, 85:044301, Apr 2012.

[40] J. L. Pore, C. Andreoiu, J. K. Smith, A. D. MacLean, A. Chester, J. D. Holt, G. C. Ball, P. C. Bender, V. Bildstein, R. Braid, A. Diaz Varela, R. Dunlop, L. J. Evitts, A. B. Garnsworthy, P. E. Garrett, G. Hackman, S. V. Ilyushkin, B. Jigmeddorj, K. Kuhn, P. Kunz, A. T. Laffoley, K. G. Leach, D. Miller, W. J. Mills, W. Moore, M. Moukaddam, L. N. Morrison, B. Olaizola, E. E. Peters, A. J. Radich, E. T. Rand, F. Sarazin, D. Southall, C. E. Svensson, S. J. Williams, and S. W. Yates. *Phys. Rev. C*, 100:054327, Nov 2019.

[41] Niels Bohr. *Nature*, 137(3461):344–348, Feb 1936.

[42] Walter Hauser and Herman Feshbach. *Phys. Rev.*, 87:366–373, Jul 1952.

[43] S. N. Ghoshal. *Phys. Rev.*, 80:939–942, Dec 1950.

[44] R. C. Alig, S. Bloom, and C. W. Struck. *Phys. Rev. B*, 22:5565–5582, Dec 1980.

[45] G.F. Knoll. *Radiation Detection and Measurement.* Wiley, 3rd edition, 2000.

[46] William R Leo. *Techniques for nuclear and particle physics experiments: a how-to approach; 2nd ed.* Springer, Berlin, 1994.

[47] Robley D. Evans. *The atomic nucleus.* McGraw-Hill New York, 1955.

[48] O. Klein and T. Nishina. *Zeitschrift fur Physik*, 52(11-12):853–868, November 1929.

[49] T. Glasmacher. *Annual Review of Nuclear and Particle Science*, 48(1):1–31, 1998.

[50] S Gales. *Journal of Physics: Conference Series*, 267:012009, jan 2011.

[51] M. A. Fraser, Y. Kadi, A. P. Bernardes, Y. Blumenfeld, E. Bravin, S. Calatroni, R. Catherall, B. Goddard, D. Parchet, E. Siesling, W. Venturini Delsolaro, G. Vandoni, D. Voulot, and L. R. Williams. Status of the hie-isolde project at cern, 2017.

[52] A.C.C. Villari, D.M. Alt, G. Bollen, D.B. Crisp, M. Ikegami, S.W. Krause, A. Lapierre, S.M. Lidia, D.J. Morrissey, S. Nash, R. Rencsok, R.J. Ringle, S. Schwarz, R. Shane, C. Sumithrarachchi, S.J. Williams, and Q. Zhao. *Commissioning and First Accelerated Beams in the Reaccelerator (Rea3) of the National Superconducting Cyclotron Laboratory, MSU.* IPAC, Busan, Korea, 2016.

[53] Eiji Ideguchi. *Progress of Theoretical and Experimental Physics*, 2012(1), 12 2012. 03C005.

[54] J. Dilling, R. Krücken, and G. Ball. *Hyperfine Interactions*, 225(1):1–8, Jan 2014.

[55] D. Voulot, F. Wenander, E. Piselli, R. Scrivens, M. Lindroos, H.B. Jeppesen, L.M. Fraile, S. Sturm, and P. Delahaye. *Nuclear Instruments and Methods in Physics Research Section B: Beam Interactions with Materials and Atoms*, 266(19):4103–4107, 2008. Proceedings of the XVth International Conference on Electromagnetic Isotope Separators and Techniques Related to their Applications.

[56] P.G. Hansen and J.A. Tostevin. *Annual Review of Nuclear and Particle Science*, 53(1):219–261, 2003.

[57] A. Lemasson, A. Navin, N. Keeley, M. Rejmund, S. Bhattacharyya, A. Shrivastava, D. Bazin, D. Beaumel, Y. Blumenfeld, A. Chatterjee, D. Gupta, G. de France, B. Jacquot, M. Labiche, R. Lemmon, V. Nanal, J. Nyberg, R. G. Pillay, R. Raabe, K. Ramachandran, J. A. Scarpaci, C. Simenel, I. Stefan, and C. N. Timis. *Phys. Rev. C*, 82:044617, Oct 2010.

[58] D.J. Morrissey, B.M. Sherrill, M. Steiner, A. Stolz, and I. Wiedenhoever. *Nuclear Instruments and Methods in Physics Research Section B: Beam Interactions with Materials and Atoms*, 204:90 – 96, 2003. 14th International Conference on Electromagnetic Isotope Separators and Techniques Related to their Applications.

[59] E. Lunderberg, J. Belarge, P.C. Bender, B. Bucher, D. Cline, B. Elman, A. Gade, S.N. Liddick, B. Longfellow, C. Prokop, D. Weisshaar, and C.Y. Wu. *Nuclear Instruments and Methods in Physics Research Section A: Accelerators, Spectrometers, Detectors and Associated Equipment*, 885:30 – 37, 2018.

[60] D. Alt. Ph.d. thesis. Michigan State University, 2016.

[61] G. Machicoane, D. Cole, J. Ottarson, J. Stetson, and P. Zavodszky. *Review of Scientific Instruments*, 77(3):03A322, 2006.

[62] P.A. Zavodszky, B. Arend, D. Cole, J. DeKamp, G. Machicoane, F. Marti, P. Miller, J. Moskalik, J. Ottarson, J. Vincent, and A. Zeller. *Nuclear Instruments and Methods in Physics Research Section B: Beam Interactions with Materials and Atoms*, 241(1):959–964, 2005. The Application of Accelerators in Research and Industry.

[63] B. Wolf. *Handbook of Ion Sources.* Taylor & Francis, 1995.

[64] G. D. Westfall, T. J. M. Symons, D. E. Greiner, H. H. Heckman, P. J. Lindstrom, J. Mahoney, A. C. Shotter, D. K. Scott, H. J. Crawford, C. McParland, T. C. Awes, C. K. Gelbke, and J. M. Kidd. *Phys. Rev. Lett.*, 43:1859–1862, Dec 1979.

[65] A. Ratkiewicz. Ph.d. thesis. Michigan State University, 2011.

[66] J.P. Dufour, R. Del Moral, H. Emmermann, F. Hubert, D. Jean, C. Poinot, M.S. Pravikoff, A. Fleury, H. Delagrange, and K.-H. Schmidt. *Nuclear Instruments and Methods in Physics Research Section A: Accelerators, Spectrometers, Detectors and Associated Equipment*, 248(2):267–281, 1986.

[67] G. Bollen. *International Journal of Mass Spectrometry*, 299(2):131–138, 2011.

[68] A Lapierre, G Bollen, J R Crespo Lopez-Urrutia, M Doleans, S Geyer, O Kester, K Kittimanapun, M Portillo, and S Schwarz. *Journal of Instrumentation*, 5(07):c07001–c07001, jul 2010.

[69] S. Schwarz, G. Bollen, J. R. Crespo López-Urrutia, O. Kester, K. Kittimanapun, A. Lapierre, D. Leitner, J. Ottarson, and M. Portillo. *Review of Scientific Instruments*, 83(2):02A908, 2012.

[70] A. Lapierre, S. Schwarz, T. M. Baumann, K. Cooper, K. Kittimanapun, A. J. Rodriguez, C. Sumithrarachchi, S. J. Williams, W. Wittmer, D. Leitner, and G. Bollen. *Review of Scientific Instruments*, 85(2):02B701, 2014.

[71] F Wenander. *Journal of Instrumentation*, 5(10):C10004–C10004, oct 2010.

[72] Thomas M. Baumann, Alain Lapierre, Stefan Schwarz, Kritsada Kittimanapun, and Georg Bollen. *AIP Conference Proceedings*, 1640(1):80–87, 2015.

[73] Q. Zhao, V. Andreev, F. Marti, S.O. Schriber, X. Wu, and R.C. York. Design studies of the reaccelerator rfq at nscl. In *2007 IEEE Particle Accelerator Conference (PAC)*, pages 1772–1774, 2007.

[74] E. Lunderberg. Ph.d. thesis. Michigan State University, 2017.

[75] W.F. Mueller, J.A. Church, T. Glasmacher, D. Gutknecht, G. Hackman, P.G. Hansen, Z. Hu, K.L. Miller, and P. Quirin. *Nuclear Instruments and Methods in Physics Research Section A: Accelerators, Spectrometers, Detectors and Associated Equipment*, 466(3):492 – 498, 2001.

[76] W.F. Mueller, D. Bazin, C.M. Campbell, J.A. Church, D.C. Dinca, A. Gade, T. Glasmacher, P.G. Hansen, K.L. Yurkewicz, H. Olliver, B.M. Sherrill, and J.R. Terry. *Nuclear Physics A*, 734:418–424, 2004.

[77] O Wieland, F Camera, B Million, A Bracco, and J van der Marel. *Nuclear Instruments and Methods in Physics Research Section A: Accelerators, Spectrometers, Detectors and Associated Equipment*, 487(3):441–449, 2002.

[78] S. Lipschutz, R.G.T. Zegers, J. Hill, S.N. Liddick, S. Noji, C.J. Prokop, M. Scott, M. Solt, C. Sullivan, and J. Tompkins. *Nuclear Instruments and Methods in Physics Research Section A: Accelerators, Spectrometers, Detectors and Associated Equipment*, 815:1–6, 2016.

[79] H. Crawford. Ph.d. thesis. Michigan State University, 2010.

[80] Technical detail on sega. `https://nscl.msu.edu/users/equipment.html#sega`. Accessed: November 23, 2021.

[81] K. Starosta, C. Vaman, D. Miller, P. Voss, D. Bazin, T. Glasmacher, H. Crawford, P. Mantica, H. Tan, W. Hennig, M. Walby, A. Fallu-Labruyere, J. Harris, D. Breus, P. Grudberg, and W.K. Warburton. *Nuclear Instruments and Methods in Physics Research Section A: Accelerators, Spectrometers, Detectors and Associated Equipment*, 610(3):700–709, 2009.

[82] C.J. Prokop, S.N. Liddick, B.L. Abromeit, A.T. Chemey, N.R. Larson, S. Suchyta, and J.R. Tompkins. *Nuclear Instruments and Methods in Physics Research Section A: Accelerators, Spectrometers, Detectors and Associated Equipment*, 741:163 – 168, 2014.

[83] D. Rhodes. Ph.d. thesis. Michigan State University, 2021.

[84] R. Bass. *Nuclear Physics A*, 231(1):45 – 63, 1974.

[85] A. Gavron. *Phys. Rev. C*, 21:230–236, Jan 1980.

[86] James F. Ziegler, M.D. Ziegler, and J.P. Biersack. *Nuclear Instruments and Methods in Physics Research Section B: Beam Interactions with Materials and Atoms*, 268(11):1818 – 1823, 2010. 19th International Conference on Ion Beam Analysis.

[87] R. Fox. Spectcl home page). `http://docs.nscl.msu.edu/daq/spectcl/`. Accessed: November 23, 2021.

[88] Rene Brun and Fons Rademakers. *Nuclear Instruments and Methods in Physics Research Section A: Accelerators, Spectrometers, Detectors and Associated Equipment*, 389(1):81–86, 1997. New Computing Techniques in Physics Research V.

[89] NSCL lifetime group wiki. `https://wikihost.nscl.msu.edu/lifetime/`. Accessed: November 23, 2021.

[90] S. Agostinelli, J. Allison, K. Amako, J. Apostolakis, H. Araujo, P. Arce, M. Asai, D. Axen, S. Banerjee, G. Barrand, F. Behner, L. Bellagamba, J. Boudreau, L. Broglia, A. Brunengo, H. Burkhardt, S. Chauvie, J. Chuma, R. Chytracek, G. Cooperman, G. Cosmo, P. Degtyarenko, A. Dell'Acqua, G. Depaola, D. Dietrich, R. Enami, A. Feliciello, C. Ferguson, H. Fesefeldt, G. Folger, F. Foppiano, A. Forti, S. Garelli, S. Giani, R. Giannitrapani, D. Gibin, J.J. Gómez Cadenas, I. González, G. Gracia Abril, G. Greeniaus, W. Greiner, V. Grichine, A. Grossheim, S. Guatelli, P. Gumplinger, R. Hamatsu, K. Hashimoto, H. Hasui, A. Heikkinen, A. Howard, V. Ivanchenko, A. Johnson, F.W. Jones, J. Kallenbach, N. Kanaya, M. Kawabata, Y. Kawabata, M. Kawaguti, S. Kelner, P. Kent, A. Kimura, T. Kodama, R. Kokoulin, M. Kossov, H. Kurashige, E. Lamanna, T. Lampén, V. Lara, V. Lefebure, F. Lei, M. Liendl, W. Lockman, F. Longo, S. Magni, M. Maire, E. Medernach, K. Minamimoto, P. Mora de Freitas, Y. Morita, K. Murakami, M. Nagamatu, R. Nartallo, P. Nieminen, T. Nishimura, K. Ohtsubo, M. Okamura, S. O'Neale, Y. Oohata, K. Paech, J. Perl, A. Pfeiffer, M.G. Pia, F. Ranjard, A. Rybin, S. Sadilov, E. Di Salvo, G. Santin, T. Sasaki, N. Savvas, Y. Sawada, S. Scherer, S. Sei, V. Sirotenko, D. Smith, N. Starkov, H. Stoecker, J. Sulkimo, M. Takahata, S. Tanaka, E. Tcherniaev, E. Safai Tehrani, M. Tropeano, P. Truscott, H. Uno, L. Urban, P. Urban, M. Verderi, A. Walkden,

W. Wander, H. Weber, J.P. Wellisch, T. Wenaus, D.C. Williams, D. Wright, T. Yamada, H. Yoshida, and D. Zschiesche. *Nuclear Instruments and Methods in Physics Research Section A: Accelerators, Spectrometers, Detectors and Associated Equipment*, 506(3):250–303, 2003.

[91] C.D. Nesaraja and E.A. McCutchan. *Nuclear Data Sheets*, 133:1–220, 2016.

[92] Jun Chen and Balraj Singh. *Nuclear Data Sheets*, 135:1–192, 2016.

[93] Balraj Singh and Jun Chen. *Nuclear Data Sheets*, 126:1–150, 2015.

[94] Jun Chen, Balraj Singh, and John A. Cameron. *Nuclear Data Sheets*, 112(9):2357–2495, 2011.

[95] A. Lemasson, H. Iwasaki, C. Morse, D. Bazin, T. Baugher, J. S. Berryman, A. Dewald, C. Fransen, A. Gade, S. McDaniel, A. Nichols, A. Ratkiewicz, S. Stroberg, P. Voss, R. Wadsworth, D. Weisshaar, K. Wimmer, and R. Winkler. *Phys. Rev. C*, 85:041303(R), Apr 2012.

[96] E. K. Warburton, C. W. Beausang, D. B. Fossan, L. Hildingsson, W. F. Piel, and J. A. Becker. *Phys. Rev. C*, 34:136–151, Jul 1986.

[97] L.P. Ekström, H.H. Eggenhuisen, G.A.P. Engelbertink, J.A.J. Hermans, and H.J.M. Aarts. *Nuclear Physics A*, 283(1):157–175, 1977.

[98] P. G. Bizzeti, P. R. Maurenzig, G. Poggi, and G. Lo Bianco. *Lett.Nuovo Cim.*, 12:53, 1975.

[99] W. Kutschera, B. A. Brown, H. Ikezoe, G. D. Sprouse, Y. Yamazaki, Y. Yoshida, T. Nomura, and H. Ohnuma. *Phys. Rev. C*, 12:813–820, Sep 1975.

[100] S.-C. Wu. *Nuclear Data Sheets*, 91(1):1 – 116, 2000.

[101] P.M. Endt. *Atomic Data and Nuclear Data Tables*, 23(6):547 – 585, 1979.

[102] Yutaka Utsuno, Takaharu Otsuka, B. Alex Brown, Michio Honma, Takahiro Mizusaki, and Noritaka Shimizu. *Phys. Rev. C*, 86:051301(R), Nov 2012.

[103] B. A. Brown and B. H. Wildenthal. *Annual Review of Nuclear and Particle Science*, 38(1):29–66, 1988.

[104] M. Honma, T. Otsuka, B. A. Brown, and T. Mizusaki. *The European Physical Journal A - Hadrons and Nuclei*, 25(1):499–502, Sep 2005.

[105] Takaharu Otsuka, Toshio Suzuki, Michio Honma, Yutaka Utsuno, Naofumi Tsunoda, Koshiroh Tsukiyama, and Morten Hjorth-Jensen. *Phys. Rev. Lett.*, 104:012501, Jan 2010.

[106] M. Honma, T. Otsuka, B. A. Brown, and T. Mizusaki. *Phys. Rev. C*, 69:034335, Mar 2004.

[107] J. Ash, H. Iwasaki, T. Mijatović, T. Budner, R. Elder, B. Elman, M. Friedman, A. Gade, M. Grinder, J. Henderson, B. Longfellow, A. Revel, D. Rhodes, M. Spieker, Y. Utsuno, D. Weisshaar, and C. Y. Wu. *Phys. Rev. C*, 103:L051302, May 2021.

[108] F. Touchard, P. Guimbal, S. Büttgenbach, R. Klapisch, M. De Saint Simon, J.M. Serre, C. Thibault, H.T. Duong, P. Juncar, S. Liberman, J. Pinard, and J.L. Vialle. *Physics Letters B*, 108(3):169–171, 1982.

[109] J. Papuga, M. L. Bissell, K. Kreim, K. Blaum, B. A. Brown, M. De Rydt, R. F. Garcia Ruiz, H. Heylen, M. Kowalska, R. Neugart, G. Neyens, W. Nörtershäuser, T. Otsuka, M. M. Rajabali, R. Sánchez, Y. Utsuno, and D. T. Yordanov. *Phys. Rev. Lett.*, 110:172503, Apr 2013.

[110] Takaharu Otsuka, Toshio Suzuki, Rintaro Fujimoto, Hubert Grawe, and Yoshinori Akaishi. *Phys. Rev. Lett.*, 95:232502, Nov 2005.

[111] Ian J. Thompson. *Computer Physics Reports*, 7(4):167–212, 1988.

[112] I. Thompson. Fresco: Coupled reaction channel calculations. `http://www.fresco.org.uk/`. Accessed: November 23, 2021.

[113] Ian J. Thompson and Filomena M. Nunes. *Nuclear Reactions for Astrophysics.* Cambridge University Press, 1st edition, 2009.

[114] D. Chattopadhyay, S. Santra, A. Pal, A. Kundu, K. Ramachandran, R. Tripathi, B. J. Roy, T. N. Nag, Y. Sawant, B. K. Nayak, A. Saxena, and S. Kailas. *Phys. Rev. C*, 97:051601, May 2018.

[115] D. H. Luong, M. Dasgupta, D. J. Hinde, R. du Rietz, R. Rafiei, C. J. Lin, M. Evers, and A. Diaz-Torres. *Phys. Rev. C*, 88:034609, Sep 2013.

[116] K. Bethge, C.M. Fou, and R.W. Zurmühle. *Nuclear Physics A*, 123(3):521–530, 1969.

[117] G. Neyens. *Journal of Physics Conference Series (Online)*, 445(1):6, Jul 2013. NUCLEAR PHYSICS AND RADIATION PHYSICS.